Thèse (Dissertation)

"Tests of the standard model in photoproduction at HERA and the LHC"

de Favereau de Jeneret, Jérôme

Abstract

Photoproduction has been used at colliders for decades in order to study hadronic properties of matter. The energy and luminosity of recent and future colliders allow probing also the electroweak sector through photon-photon and photon-proton interactions. At the HERA electron-proton collider, studies of the W boson production provide a stringent test of the Standard Model. At the LHC, photoproduction has to be separated from the overwhelming background of partonic interactions. A powerful 'tagging' technique can be introduced by adding special detectors placed far from the interaction point to detect forward scattered protons, usually present in photon-mediated processes. The HECTOR software package was written in order to provide accurate simulation of forward protons trajectories in the LHC beam-lines. These tools have been used in order to study the photoproduction of top quarks via flavor-changing neutral currents. This process is practically absent in the Standard Model, while it appears in some of its extensions. Detection of such a process would thus be an evidence for the ex[...]

Référence bibliographique

de Favereau de Jeneret, Jérôme. *Tests of the standard model in photoproduction at HERA and the LHC*. Prom. : Piotrzkowski, Krzysztof (2009)

Université catholique de Louvain
Faculté des Sciences
Département de Physique
Center for Particle Physics and Phenomenology

Tests of the Standard Model in photoproduction at HERA and the LHC

Jérome de Favereau de Jeneret
Promoteur: Prof. K. Piotrzkowski

Thèse présentée en vue de l'obtention
du grade de Docteur en Sciences

Avril 2009

Contents

1 Photon interactions at colliders **3**
- 1.1 The HERA Collider 4
- 1.2 The LHC 12
- 1.3 Factorisation in photon interactions 16
- 1.4 Anomalous couplings involving photons 32

2 W boson production at HERA **41**
- 2.1 Motivation 41
- 2.2 The ZEUS detector 43
- 2.3 Background 46
- 2.4 Simulation 46
- 2.5 Event reconstruction and selection 50
- 2.6 Results and cross-section measurement 56
- 2.7 Summary 59

3 Tagging photoproduction at the LHC **61**
- 3.1 Tagging with the central detector 61
- 3.2 Forward detectors at the LHC 67

4 Anomalous top photoproduction at the LHC **103**
- 4.1 Photon interactions at the LHC 103
- 4.2 Anomalous top search at the LHC 107
- 4.3 Early LHC anomalous top photoproduction study 109
- 4.4 Anomalous top search at high luminosity 127
- 4.5 Anomalous triple gauge couplings 141
- 4.6 Conclusions and perspectives 143

Appendix **150**

A Hector, a fast simulator for particles in beamlines **151**
A.1 The basics of beam simulation 152
A.2 Acceptance computation 158
A.3 Hector howto 160

B Phiti: a simple Υ and J/Ψ photoproduction simulator **173**

Bibliography **175**

Figures and Tables **184**

Introduction

The present dissertation aims at giving a hint of the potential behind photon interactions at modern colliders, especially HERA and the LHC. These two machines offer very different experimental conditions for such studies: while at HERA photon interactions represented a large fraction of the visible cross-section, at the LHC they are overwhelmed by strong interactions between partons.

We start by presenting the two colliders, the motivations behind them and their technical aspects. Some of the important achievements of the HERA experiments will be shown, along with a short overview of the LHC physics program. Some aspects of photoproduction are then presented, starting from the notion of the equivalent flux of photon associated with high energy charged particles and ending with some physics cases in which photoproduction is the natural way to extend our understanding of the universe.

The second chapter presents an analysis performed using data from the ZEUS detector at HERA on the production of W bosons, part of which is due to photoproduction.

Chapter three focuses on the experimental challenges at the LHC and on photoproduction tagging techniques. Three different techniques are presented, along with the difficulties associated with such procedures.

In the last chapter of the dissertation, we use these tagging techniques in the interesting physics case of anomalous single top photoproduction through Flavour Changing Neutral Current at the LHC. It is demonstrated how the present limits on such processes can be greatly improved by benefiting from both the huge energies and luminosities of the LHC and the intrinsic assets of photon interactions.

Chapter 1

Photon interactions at colliders

The term "photoproduction" was first used in the early fifties, when photons coming from electron Bremsstrahlung beam where directed toward a hydrogen target in order to study photon-proton interactions. The electron associated with the photon was deflected by the means of a spectrometer magnet, which allowed to know precisely the photon energy. This so-called "tagged photon" technique is still very close to the methods used at present colliders. Early fixed-target photon-proton experiments measured pions and other mesons production [1, 2] in order to understand the mechanisms behind such interactions.

In parallel, the first interactions induced by photons exchanged by colliding charged particles have been studied around 1970 at Novosibirsk [3] and Frascati [4] through the $e^+e^- \to e^+e^-e^+e^-$ process, which showed cross-sections compatible with a fourth-order QED interaction. At the DESY Doris collider, this process was later used to exclude the Han-Nambu model of integer charged quarks [5]. It is also in photon-photon interactions that the hadronic structure of the photon was unveiled and first measured by the PLUTO experiment at DESY [6].

Such interactions were studied more extensively at LEP. The measurement of the total photon-photon cross-section showed an excess that was interpreted as the effect of soft hadronic colourless exchanges [7, 8]. Studies of dijet production also allowed to measure the parton content of the photon and to perform heavy quarks studies [9].

Photoproduction processes took an important place at the HERA electron-proton collider, as many processes happened through a quasi-real photon exchange between an electron and a parton from an incoming

proton (a quasi-real photon is defined as a photon with very low virtuality $Q^2 = -k^\mu k_\mu$ where k^μ is the photon four-vector). Dijet production studies allowed to probe the gluon content of the photon for the first time and exclusive vector meson photproduction was studied leading to the extraction of generalised parton density functions (PDFs) of the proton [10]. Finally, thanks to high HERA beam energies, electroweak processes could be studied in photoproduction for the first time.

At the Tevatron $p\bar{p}$ collider, both photon-proton and photon-photon interaction can occur. Several studies were performed measuring electron and muon pair production. Photon-(anti-)proton interactions were also studied in order to measure production cross-sections of quarkonium states like the J/Ψ, Ψ' and Υ (see for instance [11, 12]).

As a general rule, photoproduction has mainly been used as a tool for hadronic studies. At higher energies and with large luminosities, electroweak studies and search for physics beyond the Standard Model (BSM) become possible. This could be achieved through a photon collider based on a high-energy lepton collider. Compton backscattering of laser photons on a lepton beam is considered as means of producing a high density flux of energetic photons [13]. However, such a project will not take place before years.

As the Tevatron showed the feasibility of studying photon-induced interactions at hadron colliders, the LHC now offers the opportunity to study electroweak processes via photon-photon and photon-proton interactions at higher luminosity and energy [14].

The present dissertation focuses on two processes: W production at HERA and anomalous single top photoproduction via flavour-changing neutral current at the LHC. The two coliders are briefly presented in the following sections.

1.1 The HERA Collider

1.1.1 The need for a lepton-hadron collider

Probing the structure of the proton has been one of the important challenges of particle physics ever since proton point-like components were found in it in the late 60's in fixed-target SLAC experiments [15]. In high energy scattering, the spatial resolution for a "particle microscope" is proportional to $1/\sqrt{Q^2}$ where Q^2 is the virtuality of the probing particle. This virtuality is kinematically bound to be lower than the square

s of the centre of mass energy of the interaction. The most natural way to probe the proton structure is through deep inelastic scattering at a fixed-target experiment involving a lepton beam. In that case, the centre of mass energy of the lepton-proton system is given by $\sqrt{2Mc^2E_l}$ where M is the proton mass and E_l is the incoming lepton beam energy. This makes the maximum reachable spatial resolution Δx:

$$\Delta x_{min} \sim \frac{hc}{\sqrt{Q^2_{max}}} \simeq \frac{h}{\sqrt{2E_lM}},$$

where h is Planck's constant and c is the speed of light[1]. The spatial resolution achieved with a typical beam energy of 100 GeV can only reach $\mathcal{O}(10^{-16} - 10^{-17}$ m) which is close to the lower limit to probe the inner structure of the proton. On the other hand, a lepton-hadron collider has a maximum s of $4E_lE_p$. The resolution is then given by:

$$\Delta x_{min} \sim \frac{hc}{2\sqrt{E_lE_p}},$$

which allows to probe the proton deeper than at any fixed-target setup.

Additionally, a lepton-hadron collider offers the opportunity to validate particular theories such as leptoquarks or R-parity violating supersymmetry in which particles with both leptonic and hadronic properties appear. Such particles could be directly produced by quark-electron fusion. Finally, it is an ideal tool to study photoproduction, thanks to the important flux of quasi-real photons associated with the beam electrons.

1.1.2 The HERA era

The HERA (*Hadron Elektron Ringe Anlage*) project of an electron[2]-proton collider at DESY, Hamburg, Germany, started in the 80's, roughly at the same time as the LEP project at CERN, Geneva, Switzerland, with very complementary goals. The former aiming at probing the structure of the proton and pushing the knowledge of quantum chromodynamics to a new scale, the latter at providing precision measurements for many (especially) electroweak parameters while searching for the Higgs boson.

[1] In the rest of the present thesis the "natural units" convention is used ($\hbar = c = 1$).

[2] Unless otherwise stated, the word "electron" will be used for both electrons and positrons in the following discussions about HERA physics.

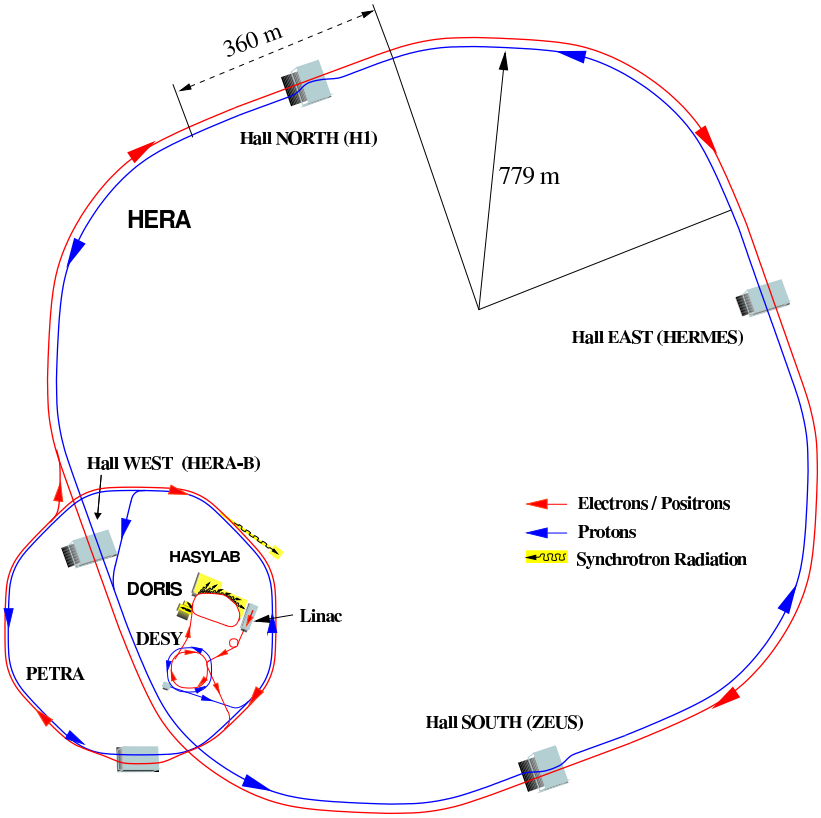

Figure 1.1: The HERA collider complex with its injection system.

The HERA double synchrotron is 6.3 km in circumference and is buried between 15 m and 25 m deep. Along with the main ring, the HERA project implied that both the electron and the proton beams had to pass through four pre-accelerators before reaching the main ring, leading to the need for six accelerators before the particles could be injected into the PETRA rings and finally reach HERA. An illustration of the structure of the HERA accelerator and pre-accelerator complex is shown on Fig. 1.1.

Four experiments took place around the collider. The ZEUS and H1 detectors were traditional, "4π" or "hermetic"[3] detectors, although they were very asymmetric because of the energy difference between the two beams. The HERMES detector studied the interactions of a

[3]This refers to the fact that the detector nearly covers the complete solid angle around the interaction point.

Parameters	Proton	Electron
Injection energy [GeV]	40	12
Collision energy [GeV]	820 (920)	27.5
Number of bunches	174	
Luminosity [cm^{-2} s^{-1}]	1.4×10^{31} (3.6×10^{31})	

Table 1.1: Parameters of the HERA collider during the HERA-I (HERA-II) phase.

polarised electron beam and a polarised fixed target from 1994 onwards. The HERA-B experiment used the proton beam halo to study B-mesons production during the last part of the HERA-I run which ended in 2000.

The data taking started in 1992 for the eight years of the "HERA-I" running bringing nearly 200 pb^{-1} of luminosity. Then the accelerator was upgraded both in terms of luminosity and energy. After the background problems linked to the luminosity upgrade were solved, the "HERA-II" running started in 2003, bringing around 600 pb^{-1} more to each experiment before it was eventually shut down in 2007.

1.1.3 Technical description

The HERA collider accelerates the electrons coming from the PETRA pre-accelerator from 12 GeV to 27.5 GeV using superconducting cavities, while the protons are accelerated from 40 GeV to 820 GeV (920 GeV during HERA-II) using conventional cavities. The centre of mass energy of the proton-electron system is thus of 300 (320) GeV.

The collider was designed to work with a proton beam current (I_p) of 140 mA and an electron current (I_e) of 58 mA, although it ran most of the time at $I_p \sim$ 100mA and $I_e \sim$ 30mA. With 174 colliding bunches of $\sim 10^{10}$ particles and a bunch crossing frequency of 10.4 MHz, the corresponding luminosity was 1.4 10^{31} $cm^{-2}s^{-1}$ during the HERA-I runs.

In order to improve the luminosity for HERA-II, the beam was further focused at the interaction points, which allowed to reach a luminosity of 3.6 10^{31} $cm^{-2}s^{-1}$. As a general rule, around 75 % of this luminosity could be gathered by the experiments. The integrated luminosity provided by HERA can be seen on Fig. 1.2. The various parameters of the HERA rings are summarised in table 1.1

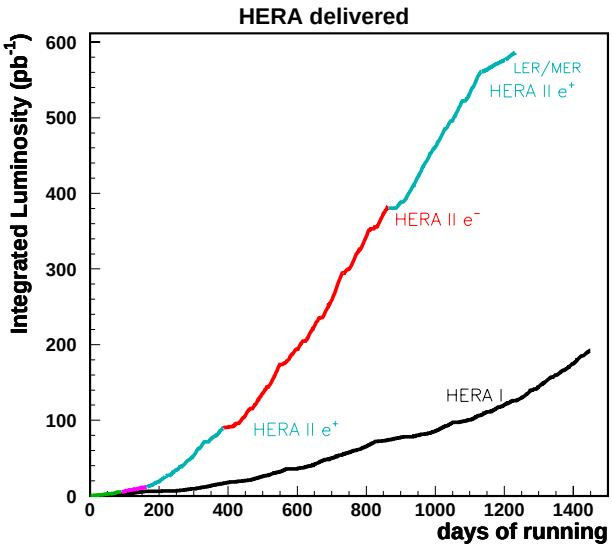

Figure 1.2: Integrated luminosity provided by the HERA collider as a function of the number of days of running.

1.1.4 Research and achievements

It would be impossible to cover here the whole subject of research at HERA[4]. Only some of the most important research topics will be described, which are closely linked to the subject of this dissertation.

The first goal of the HERA project was to probe the proton structure with a spatial resolution of $\mathcal{O}(10^{-18})$ m and thus to extend the range of the proton *structure functions* and *parton distribution functions* (pdfs) measurements. The latter are crucial as they describe the parton content of the proton as a function of the virtuality Q^2 and the fraction x of the proton momentum carried by the parton. Their knowledge is thus a prerequisite for the computation of the cross-section of hard interactions between protons. This study has been at the centre of research since the very beginning of the data taking. One can see how the range was extended by looking at Fig. 1.3 where previous experiments results only cover the lower-right part of the plot while the rest was covered by HERA. On the same plot, one sees the overlap between the regions covered by HERA and the LHC, which allows to directly use HERA measurements to predict cross-sections at the LHC. Outside of

[4]A comprehensive review can be found in [16].

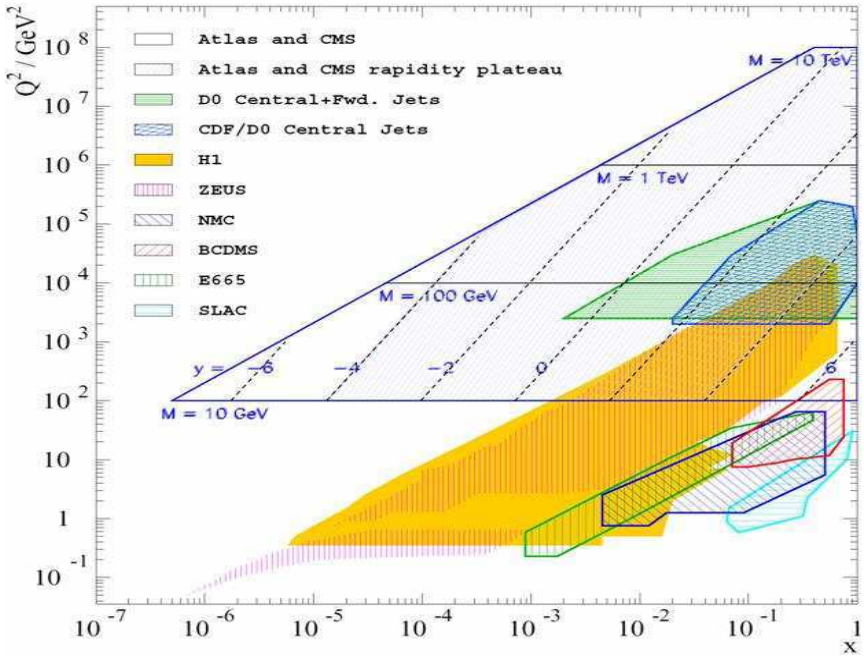

Figure 1.3: $x - Q^2$ range of various experiments for the measurement of structure functions. Fixed-target experiments fill the lower right part of the graph, corresponding to low Q^2 and high x, while HERA extended the range to higher virtualities and lower x. The LHC expected range is also plotted.

this overlapping region, the value of the functions has to be computed using evolution equations, introducing uncertainties.

A major finding was the remarkable fraction (10 %) of events in deep inelastic scattering featuring a large region in pseudo-rapidity devoid of hadronic activity around the outgoing proton direction (Fig. 1.4), which is usually called a "large rapidity gap" (LRG) (see Fig. 1.5). This side usually contains much hadronic activity because of the colour exchange between the proton and the central final state. This measurement [17, 18] thus showed that DIS could involve the exchange of colourless objects with a significant probability and established the presence of diffaction in DIS.

The ZEUS and H1 experiments also pursued many searches for signatures of beyond the Standard Model physics. Along with specific, model-dependent studies like searches for hints of supersymmetry or

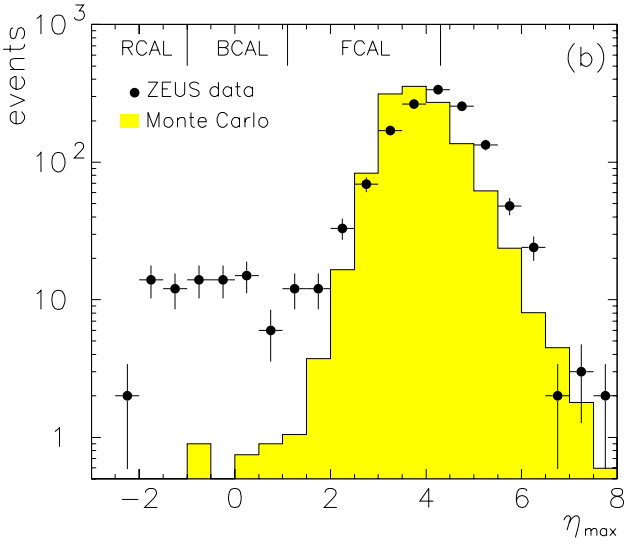

Figure 1.4: Number of observerd events as a function of the pseudo-rapidity η_{max} of the most forward calorimeter cluster in the ZEUS detector, compared with the Monte Carlo DIS expectation. One clearly sees the excess of events with an important rapidity gap between the outgoing proton direction and any activity in the detector [17].

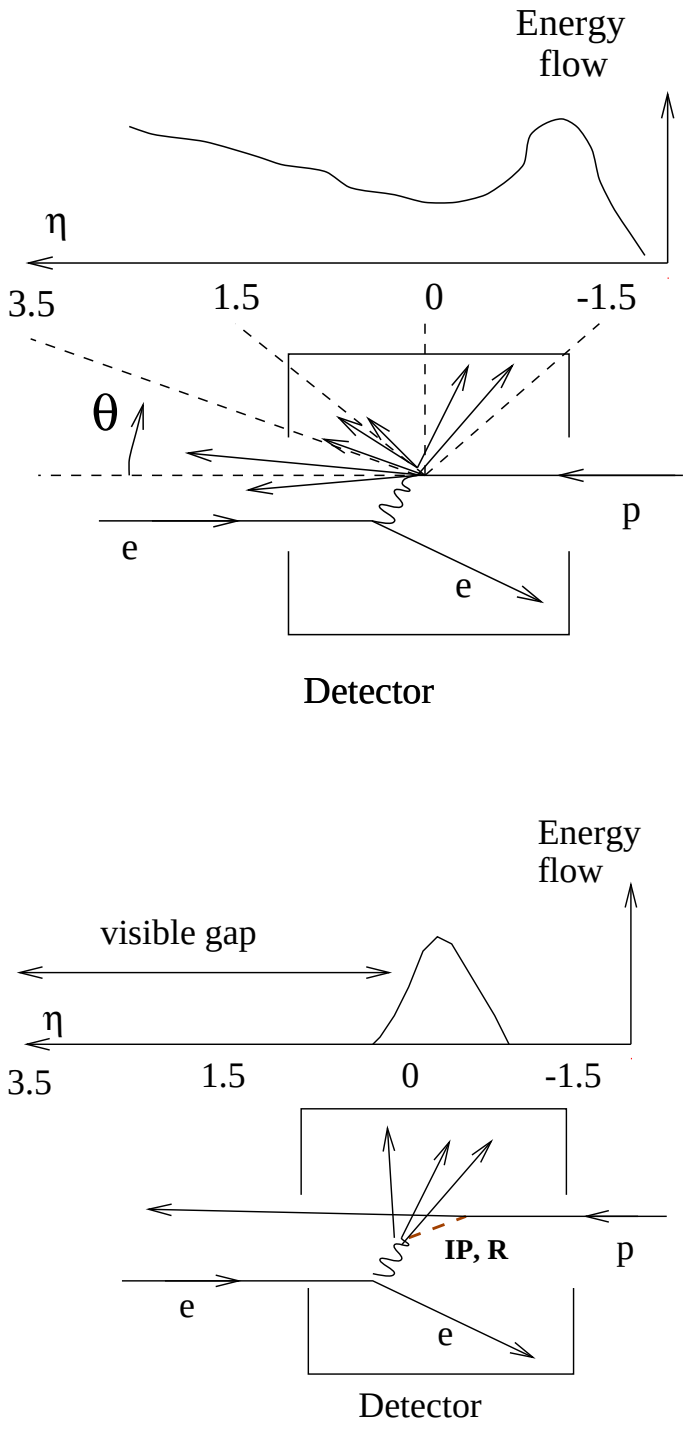

Figure 1.5: Typical deep inelastic scattering event at HERA (up) and event with a rapidity gap (down) [19]. In the latter, no activity is observed in the detector in the region between the proton outgoing direction (left) and the jet, leading to a rapidity gap with $\eta_{max} \sim 0$.

leptoquarks, a model-independent search was performed, hunting for excesses in almost every imaginable topology. For example, the H1 collaboration measured a slight (2.4σ) excess in high transverse momentum (P_T) isolated leptons, significantly above the SM predicted distribution coming mainly from W production [20]. This is a typical signature of beyond the Standard Model physics processes, especially in supersymmetry. However, the latest results of the combined analysis using H1 and ZEUS data are in agreement with the SM expectations [21].

In addition, many photoproduction studies were performed at HERA. The experience and knowledge gained from these studies form a basis for similar studies at the LHC. Particularly, tagging techniques aiming at the selection of photoproduction and diffractive processes were designed and perfected at HERA. These techniques rely on the central detector, supplemented by various small detectors placed along the beamlines, meters away from the interaction points, in order to detect outgoing protons, electrons and photons. Both the H1 and ZEUS detector were equiped with such detector setup which was used in various studies (see for instance [22, 23, 24]).

A search for W bosons at HERA using the ZEUS detector will be presented in the second chapter of the present dissertation. A good understanding of this process is mandatory in order to open the path for BSM searches, as a typical final state of the W decay - an isolated lepton and missing transverse energy - is a common signature of new physics processes.

1.2 The LHC

1.2.1 The choice of a proton-proton collider

In 2000, the LEP electron-positron collider at CERN ceased running. Many precision measurements had been achieved at centre of mass energies reaching 200 GeV, and the last days of LEP's running were especially exciting due to the possible hint for a Higgs boson with a mass around 115 GeV.

Particle physics was thus in need for a collider with a far higher centre of mass energy in order to probe the TeV scale and ensure that a SM Higgs boson would be discovered while exploring regions where BSM processes could show up. As those processes usually have low cross-sections, very high luminosity was also required.

While lepton colliders offer many advantages when compared to hadron colliders in terms of precise knowledge of the initial state and of cleanliness of the final state, reaching high energies with leptons is difficult. Circular colliders suffer from energy losses due to synchrotron radiation (the energy loss is proportional to $(E/m)^4$). They can thus hardly get to higher energies than 100 GeV as was achieved at LEP. One way to avoid this problem is to use linear colliders, but these require high field accelerating cavities in order to reach TeV scale energies for reasonable accelerator length. The technology for such cavities is still under development, for instance in the framework of the ILC or the CLIC [25] projects. A hadron synchrotron is thus at the moment the only available technique to reach TeV scale energies.

The choice had to be made between protons and anti-protons. Anti-protons offer high density of highly energetic antiquarks up and down, providing very high cross-section for Drell-Yan processes. A proton-proton collider relies more on gluon-gluon and gluon-quark interactions, but as the gluons usually carry a smaller fraction of the proton momentum, lower centre of mass energies are reachable. This can be compensated by the possibility to have far higher proton luminosities than for anti-protons and by accelerating the protons to higher energies, which was the choice made for the LHC.

1.2.2 Construction and running plans

The LHC uses the LEP tunnel, dug in the 80's under the border between Switzerland and France, close to the city of Geneva (a plane picture can be seen at Fig. 1.6). This re-use of the tunnel was already foreseen even before it was built. The LHC project officially started in 1984 and was approved by CERN in 1994.

Two "4π", general purpose detector projects, CMS and ATLAS, were accepted in 1996. Two other experiments were approved later: ALICE, dedicated to heavy ions collisions, and LHC-b which covers only one side of the interaction point, looking especially to "forward" (close to the beam pipe) objects. A fifth experiment, TOTEM, consists of forward detectors placed inside and outside of the CMS detector volume, with the purpose of measuring the elastic and total cross-sections. Finally, the LHCf experiment aims at simulating conditions in very high energy cosmic rays showers two small detectors placed on each side of ATLAS.

In 2000, the first elements of the LHC pipe were delivered and tested. The construction continued till beginning of 2008 when the last part of

the CMS detector was lowered to its position in its cavern at the so-called interaction point[5] 5 , marking the end of the construction era and allowing to prepare for the running. The various segments of the machine were cooled down during spring 2008. The official startup took place on September 10th of the same year during which both beams circulated in the ring at the injection energy of 450 GeV. Unfortunately, it ceased operating a few days later because of a technical incident and will only operate again after summer 2009.

1.2.3 Technical description

The LHC is located in the 27 km-long LEP tunnel. The protons will be accelerated by three pre-accelerators before reaching the LHC ring at an energy of 450 GeV. They will then take 20 minutes to get to the nominal energy of 7 TeV, providing a centre of mass energy of the proton-proton system of 14 TeV. The LHC can also accelerate heavy ions up to ~ 3 TeV per nucleon depending on the type of ions.

The design luminosity of the LHC is 10^{34} cm^{-2} s^{-1} or in more convenient units 10^{7} mb^{-1} s^{-1}, with a bunch-crossing frequency of 40 MHz. Bunches will contain $\sim 10^{11}$ protons. Each bunch collision at that luminosity will yield up to 20 proton-proton hadronic interactions. During the first years, the LHC is foreseen to run at lower luminosities, around $10^{32} - 10^{33}$ cm^{-2} s^{-1}. The event pile-up (number of interactions per bunch-crossing) will be lower in these conditions, which allows for some studies that would prove impossible at the highest luminosity. The running parameters of the LHC are shown in deeper details in table 1.2.

1.2.4 Physics program

The first goal of the LHC is to find the missing piece in the Standard Model, the Higgs boson. In parallel, theories like supersymmetry predict new particles whose masses are such that they could be seen at the LHC. The effects of large extra dimensions could also be seen. Finally, measurements in electroweak and top physics will be performed.

These searches form the basic physics program of both the CMS and ATLAS collaborations. The LHCb experiment proposes to explore the asymmetry between matter and antimatter through the violation of

[5]The interaction points of the LHC beams are referred as IPX, with X running from 1 to 8 while going clockwise around the ring. the ATLAS and CMS detectors are placed at the IP1 and 5 respectively.

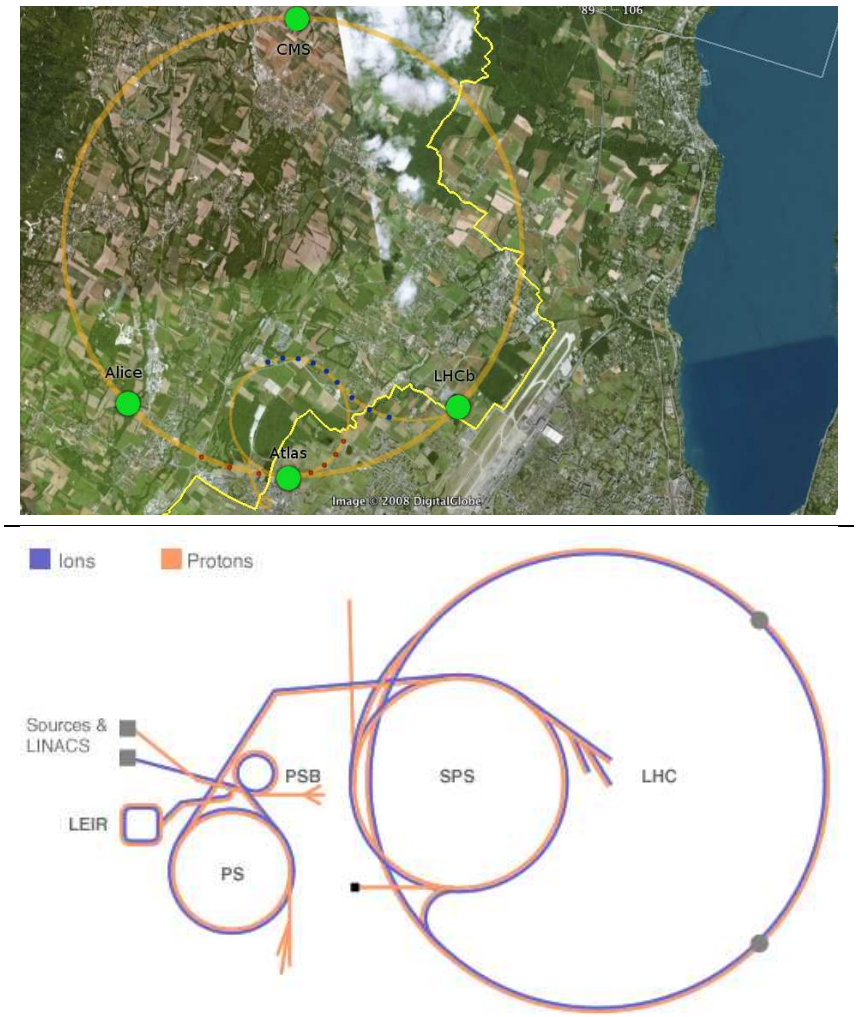

Figure 1.6: Satellite view of the LHC (top) and schematic view of the accelerator and its injection complex (bottom).

Parameters	Injection	Collision
Proton energy	450 GeV	7000 GeV
Beam lifetime	-	15 hours
proton energy loss per turn	0.12 eV	6×10^3 eV
Particles per bunch	10^{11}	
Number of bunches	2808	
RMS beam size at the IP1 and IP5	375.2 μm	16.7 μm
RMS beam size at the IP2 and IP8	279.6 μm	70.9 μm
RMS beam size in ARC sections	1190 μm	300 μm

Table 1.2: Parameters of the LHC in injection and collision mode.

the CP symmetry by looking at the decay of heavy particles containing a b quark. The ALICE collaboration focuses on heavy ions collisions in order to study the quark-gluon plasma state of matter which shows many interesting properties already partly revealed at RHIC.

In addition, the CMS and ATLAS collaboration have an important physics program related to "forward physics". This subject covers the various aspects of diffraction and photon-mediated processes. The main experiments are complemented by collaborations such as TOTEM or FP420 with their own dedicated (sub-)detectors for forward physics studies.

In particular, high energy photon interactions will offer the double benefit of very well known cross-sections as these rely mostly on Quantum Electrodynamics (QED) and of processes involving only few or no colour exchanges, leading to exclusive final states in which the observed objects in the central detectors come from the photon-photon or photon-proton interaction.

The simulation of such photon-mediated processes is based on two key ingredients: the factorisation of the photon "emission" by the beam and its hard interaction, and the computation of the properties of the photon spectrum. These two subjects are discussed in the next section.

1.3 Factorisation in photon interactions

Based on an initial idea of Fermi, Weizsäcker [26] and Williams [27] independently proposed in 1934 a method to simplify the calculation of

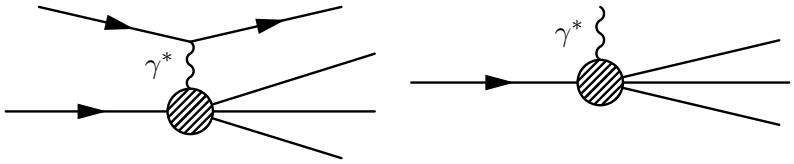

Figure 1.7: Feynman diagrams for Deep Inelastic Scattering (left) and the corresponding photoabsorbtion process (right).

processes induced by the electromagnetic field of moving charged particles.

This method is based on the constatation that the field of a charged moving particle is dominated by transverse components and thus similar to an electromagnetic wave moving in the same direction as the particle, which can consequently be seen as a beam of real photons with a given energy spectrum which can be computed from the properties of the particle.

In the case of photon interactions at colliders, it was shown that factorisation could be applied under some conditions, allowing to compute the cross-section of photon interactions through the convolution of a photon energy spectrum with the photon interaction cross-section. For instance, the HERA-type process of Fig. 1.7 is replaced with the corresponding photoabsorbtion process. The main difference is that one neglects the effect of the photon spin by neglecting the contribution of "scalar" photons.

In this section, we will describe the equivalent photon approximation (EPA) extension of the Weizsäcker-Williams method which allows to take the photon virtuality into account [28].

1.3.1 Variable definitions and kinematics

In the following discussions, the traditional deep inelastic scattering (DIS) variables are used, in addition to some other, specific variables. Based on diagram 1.8 where the photon comes from the bottom proton, one defines:

The beam proton nominal energy:

$$E = p^0$$

its mass:

$$m = \sqrt{p^\mu p_\mu}$$

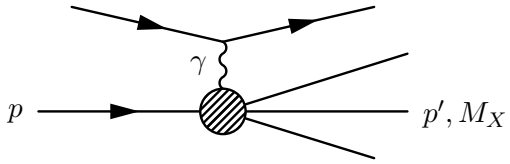

Figure 1.8: Reference diagram for the definition of variables used in the text.

the proton energy fraction taken by the photon (the so-called *Feynman x*):

$$x = \frac{q^0}{E}$$

where q^μ is the photon four-vector. the momentum transfer:

$$Q^2 = -q^2 = -(p^\mu - p'^\mu)(p_\mu - p'_\mu)$$

and the invariant mass of the hadronic system

$$M_X = p'^2 = p'^\mu p'_\mu.$$

The centre of mass energy of the photon-proton or photon-photon system will be referred as W. In case of photon-quark interactions, the centre of mass energy of the photon-parton system will be designed by $\hat{W}$.

In the elastic case, the proton survives the interaction and $M_X = m$. In all cases, the whole kinematics can be described by the following equation:

$$M_X^2 = m^2 - Q^2 - 2E^2x + 2\sqrt{E^2 - m^2}\sqrt{E^2x^2 + Q^2 - P_T^2} \qquad (1.1)$$

Where P_T is the transverse momentum of the outgoing system p'. One can compute the minimum virtuality of the photon as:

$$Q^2_{min} = x\left(\frac{M_X^2}{1-x} - m^2\right)\left[1 + \mathcal{O}\left(\frac{m^2}{E^2(1-x)^2}\right)\right]. \qquad (1.2)$$

From this, one can define two practical cases: first, for elastic exchanges, the minimum allowed virtuality is:

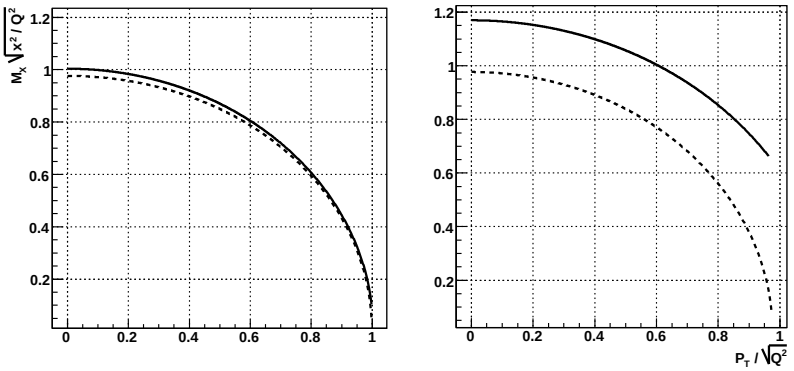

Figure 1.9: Kinematically allowed line for (P_T, M_X) for x = 0.001 (left) and 0.05 (right) for a photon virtuality of 0.1 GeV^2 (plain) and 10 GeV^2 (dashed).

$$Q^2_{min} \sim m^2 \frac{x^2}{1-x}, \tag{1.3}$$

while for the inelastic case the squared mass of the hadronic system is generally dominating the initial mass of the particle:

$$Q^2_{min} \sim M_X^2 \frac{x}{1-x}. \tag{1.4}$$

Equation 1.1 also shows that the maximum mass for the hadronic system is achieved for $P_T = 0$ as illustrated by Fig. 1.9. For values of $x \ll 1$, this maximum mass is given by:

$$M_X^{max} \sim \sqrt{\frac{Q^2}{x}}, \tag{1.5}$$

while the maximum P_T is close to $\sqrt{Q^2}$.

1.3.2 The equivalent photon approximation

Considering a process of the kind $pp \to pX$ occuring through the exchange of a photon, the matrix element for the interaction can be written as:

$$\mathcal{M} = -\langle P'|J^{\nu}_{em}(0)|P\rangle \frac{g_{\mu\nu}}{k^2} V^{\mu} \tag{1.6}$$

where J^{ν}_{em} is the electromagnetic current of the proton [30] and V^{μ} is the matrix element for the subprocess $\gamma p \to X$. The squared and averaged over spin matrix element $\overline{|\mathcal{M}|}^2$ can be written as:

$$\overline{|\mathcal{M}|}^2 = -\frac{1}{Q^2} H^{\mu\nu} T_{\mu\nu} \tag{1.7}$$

where

$$H^{\mu\nu} = \sum_{spins} \langle P'|J^{\mu}_{em}(0)|P\rangle^* \langle P'|J^{\nu}_{em}(0)|P\rangle \tag{1.8}$$

is the "hadronic tensor", here based only on electromagnetism and $T_{\mu\nu}$ is the tensor associated with the $\gamma p \to X$ subprocess. The most general form for the single particle electromagnetic current J_{em}, taking Lorentz invariance and hermiticity is, using the Dirac γ matrices:

$$\langle P'|J^{\mu}_{em}(0)|P\rangle = e\bar{u}(P') \left[\gamma^{\mu} F_1(Q^2) - \frac{i\sigma^{\mu\nu} k_{\nu}}{2m} F_2(Q^2)\right] u(P), \tag{1.9}$$

where $\sigma^{\mu\nu}$ is defined as $(\gamma^{\mu}\gamma^{\nu} - \gamma^{\nu}\gamma^{\mu})/2$, $k_{\nu} = (p - p')^{\nu}$ is the photon 4-vector and u and $\bar{u}$ are the quark spinors. The F_i functions are form factors related to the electric charge q and magnetic dipole moment μ of the considered particle:

$$\begin{aligned} F_1(0) &= \frac{q}{e} \\ F_2(0) &= \frac{1}{e}(2m\mu - q). \end{aligned} \tag{1.10}$$

For an electron for instance, $e = q$ and $\mu = e/2m$, so we have $F_1(0) = 1$ and $F_2(0) = 0$. Doing the full calculation of the cross-section while neglecting the "longitudinal" component of the cross-section [28], one obtains the factorised shape:

$$d\sigma_{pp\to pX} = \sigma_{\gamma p\to X} \times dN_{\gamma} \tag{1.11}$$

This approximation is valid because the cross-section is generally dominated by the low-virtuality region (as a direct consequence of the shape of the photon propagator). A notable example of inapplicability is the lepton pair two-photon production (fig. 1.10) with lepton beams, for which the cross-section is not decreasing as required with the photon virtuality. However, in the case of hadron colliders a natural cutoff

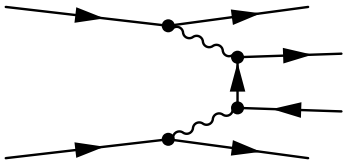

Figure 1.10: Lepton pair production via photon-photon interaction

particle	H_1	H_2
pointlike, scalar	1	0
pointlike, spin 1/2	1	1
composite, scalar (pion)	F_π^2	0
proton (elastic)	$\frac{(4m^2 G_E^2 + Q^2 G_M^2)}{4m^2+Q^2}$	$G_M^2(Q^2)$
proton (inelastic)	$\int \frac{F_2}{x_b^3} dx_b$	$\int \frac{F_2}{x_b} dx_b$

Table 1.3: H_1 and H_2 functions for different beam particles. G_E, G_M and F_π are form factors of the proton and pion. F_2 is the usual proton structure function.

arises due to the electromagnetic form factors, which extends the EPA applicability even more in the elastic case.

The spectrum dN_γ is the number of photons in a given dQ^2dx phase space region and is given by the EPA formula:

$$\frac{d^2N_\gamma}{dQ^2dx} = \frac{\alpha}{\pi}\frac{1}{Q^2\ x}\left[(1-x)\left(1-\frac{Q^2_{min}}{Q^2}\right)H_1(Q^2) + \frac{x^2}{2}H_2(Q^2)\right]. \quad (1.12)$$

The H_1 and H_2 functions are the electric and magnetic form factors of the incoming particle, which are expressed in terms of the F_i functions of equation 1.9 by:

$$\begin{aligned} H_1 &= F_1^2 + \frac{Q^2}{4m^2}F_2^2 \\ H_2 &= (F_1+F_2)^2. \end{aligned} \quad (1.13)$$

A selection of form factors to use for different cases can be found in table 1.3.

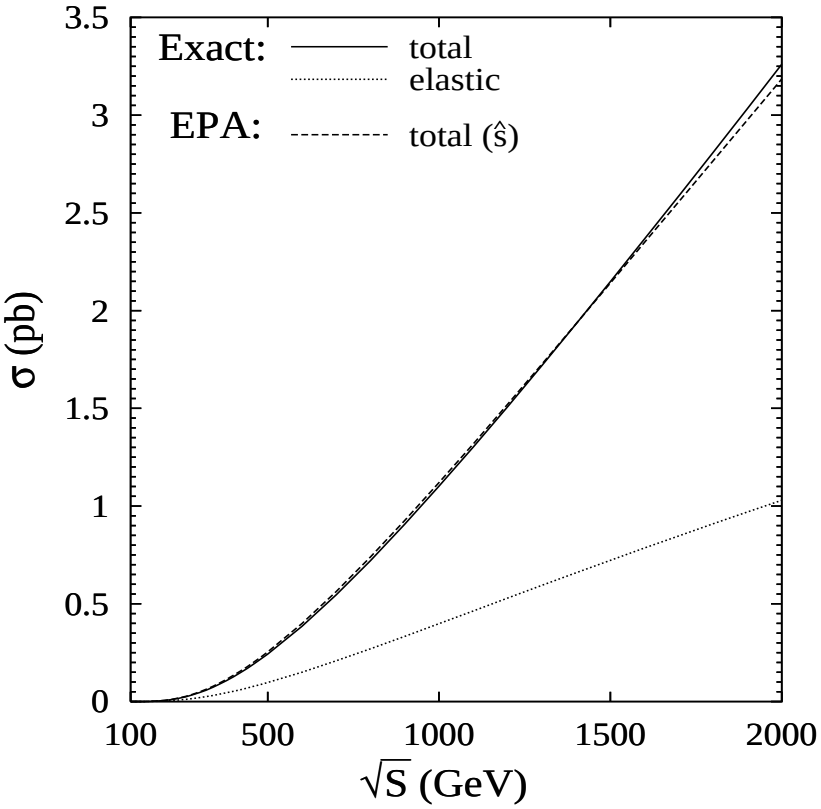

Figure 1.11: Comparison of exact computation of the process $ep \rightarrow \nu WX$ with the result obtained through EPA. The EPA elastic component is indistinguishable from the exact calculation

Comparisons of results obtained using the equivalent photon approximation and exact calculation were performed by Kniehl [30] and Pisano [29] for the production of W bosons at HERA considering elastic and inelastic photon exchange respectively. Both show an excellent agreement as illustrated by Fig. 1.11 from [29].

1.3.3 Equivalent photon spectrum for electrons

Following the method described previously, one of the simplest nontrivial cases is the spectrum associated with a moving electron. As the electron is pointlike and has spin 1/2, both H_1 and H_2 functions are equal to one and independent from Q^2. The spectrum is thus given by:

$$\frac{d\mathcal{N}}{dxdQ^2} = \frac{\alpha}{\pi}\,\frac{1}{x}\,\frac{1}{Q^2}\left[(1-x)(1-\frac{Q^2_{min}}{Q^2}) + \frac{x^2}{2}\right]. \qquad (1.14)$$

1.3.4 Equivalent photon spectrum for protons

Elastic photon exchange spectrum

We use here the dipole approximation for the proton form factors extracted from experiments on elastic scattering. The convenient variables to measure are the so-called Sachs combinations G_M and G_E which have the simple behaviour:

$$\begin{aligned} G_E(Q^2) = \quad & F_1(Q^2) - \tfrac{Q^2}{4m^2}F_2(Q^2) \quad &= \frac{1}{(1+Q^2/Q_0^2)^2} \\ G_M(Q^2) = \quad & F_1(Q^2) + F_2(Q^2) \quad &= \frac{\mu_p}{(1+Q^2/Q_0^2)^2} \end{aligned} \qquad (1.15)$$

with $\mu_p = 2.79$ and $Q_0^2 = 0.71\mathrm{GeV}^2$. Using the definitions of the F_i functions, one gets:

$$\begin{aligned} H_1(Q^2) &= G_M^2 \\ H_2(Q^2) &= \frac{(4m^2\ G_E^2 + Q^2\ G_M^2)}{4m^2+Q^2} \end{aligned}$$

One can note that these form factors fall rapidly with increasing Q^2 as shown on Fig. 1.12 making the approximation of low virtuality valid in most cases. Replacing those into equation 1.12 and integrating over Q^2, one gets the EPA spectrum for elastic interactions [28]:

$$\frac{d\mathcal{N}}{dx} = \frac{\alpha}{\pi}\frac{1-x}{x}\left[\varphi(\frac{Q^2_{max}}{Q_0^2}) - \varphi(\frac{Q^2_{min}}{Q_0^2})\right], \qquad (1.16)$$

with the φ function defined as:

$$\begin{aligned} \varphi(\rho) = (1+ay)\left[-\ln(1+\frac{1}{\rho}) + \sum_{k=1}^{3}\frac{1}{k(1+\rho)^k}\right] + \frac{(1-b)y}{4X(1+\rho)^3} \\ +c(1+\frac{y}{4})\left[\ln\frac{1-b+\rho}{1+\rho} + \sum_{k=1}^{3}\frac{b^k}{k(1+\rho)^k}\right]; \end{aligned} \qquad (1.17)$$

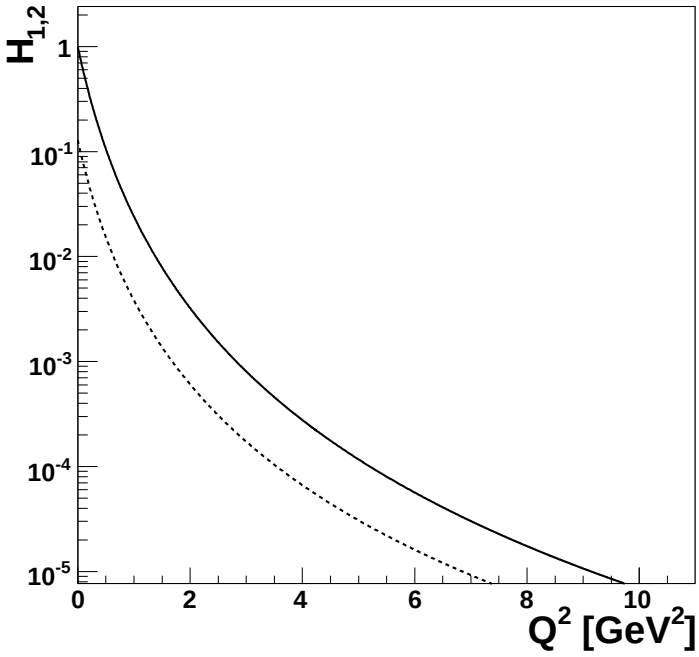

Figure 1.12: Behaviour of the form factors H_1 (plain) and H_2 (dashed) as a function of the photon virtuality.

$$y = \frac{x^2}{(1-x)},\ a = (1+\mu_p^2)/4 \approx 7.16,\ b = 1 - 4m^2/Q_0^2 \approx -3.96,$$
$$c = (\mu_p^2 - 1)/b^2 \approx 0.028.$$

Inelastic photon exchange spectrum

In this case, the H_1 and H_2 form factors from equation 1.12 are integrated versions of the structure function $F_2(x_b, Q^2)$, namely:

$$\begin{aligned} H_1 &= \int \frac{F_2(x_b, Q^2)}{x_b}\, dx_b \\ H_2 &= \int \frac{F_2(x_b, Q^2)}{x_b^3}\, dx_b \end{aligned} \tag{1.18}$$

where x_b is the *Bjorken variable* equal to $Q^2/(M_X^2 + Q^2)$. The integrals of equation 1.18 can be seen as integrals over M_X from the minimal kinematically allowed value which is equal to the mass of the incoming particle to a maximum mass that can be fixed by the experimental conditions. For instance, this limit could be fixed by the condition that the hadronic system (the beam remnant) is not seen by the central detector.

The $F_2(x_b, Q^2)$ function is extracted experimentally from the $\sigma(\gamma^* p)$ cross-section measured in fixed-target and collider experiments by various collaborations such as BCDMS, E665, NMC, H1 and ZEUS. This is achieved by using the relation:

$$\sigma_{total}(\gamma^* p) = \frac{4\pi^2\alpha}{Q^2(1-x_b)} \frac{Q^2 + 4M_p^2 x_b^2}{Q^2} F_2(x_b, Q^2). \tag{1.19}$$

For the practical purpose of Monte Carlo simulation, the ALLM97 [35, 36] parametrisation of F_2 has been used to compute the EPA spectrum.

The computation of the H_1 part of the EPA spectrum, as given in equation 1.18, requires the integration over M_X of this function. The change of variables $x_b \leftrightarrow M_X$ gives:

$$H_1 = \int_m^{M_X^{max}(x,Q^2)} \frac{2M_X}{M_X^2 + Q^2}\, F_2(Q^2, M_X)\, dM_X. \tag{1.20}$$

The behaviour of this form factor is shown on Fig. 1.13. One should not forget that the maximum mass of the X system M_X^{max} depends on

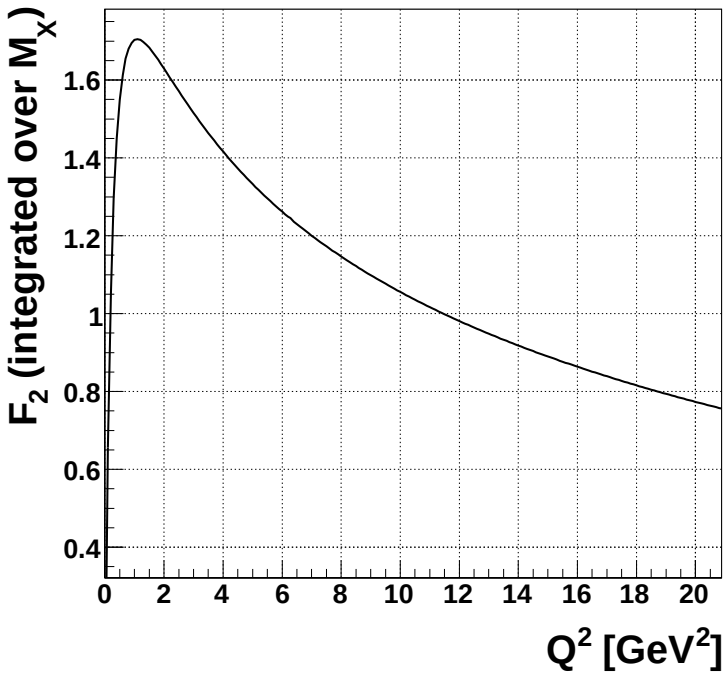

Figure 1.13: Value of the structure function F_2 as a function of the virtuality of the exchanged boson ($M_X^{max} = 20$ GeV).

the photon virtuality through 1.1. The energy spectrum of the photon is thus given by (neglecting the H_2 part as low energy photons dominate the spectrum):

$$\frac{d\mathcal{N}}{dx} = \frac{\alpha}{\pi}\frac{1-x}{x}\int_{m^2\frac{x}{1-x}}^{Q^2_{max}} dQ^2 \int_m^{M_X^{max}(x,Q^2)} dM_X \left(1 - \frac{Q^2_{min}(x,M_X)}{Q^2}\right) \times \frac{2M_X}{M_X^2+Q^2} F_2(Q^2, M_X). \quad (1.21)$$

This spectrum is shown on Fig. 1.14.

1.3.5 Photon luminosity

The essence of EPA is to represent a charged particle collider as a photon collider with corresponding energy and virtuality spectrum. It is

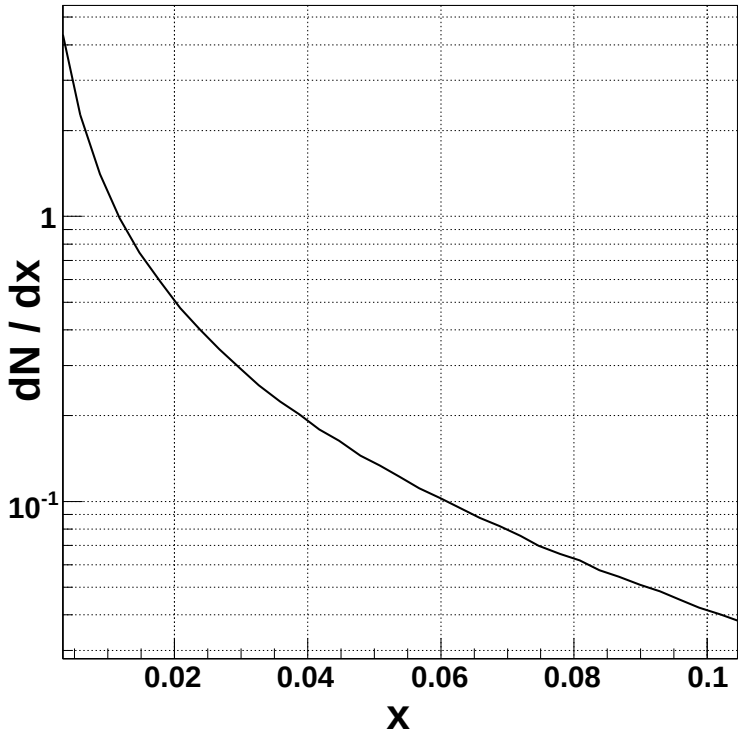

Figure 1.14: Photon energy spectrum for inelastic photon exchange as a function of the photon energy fraction x. The mass M_X has been required to be lower than 20 GeV.

thus interesting to compute the ratio of the photon luminosity to the collider nominal luminosity as a function of the centre of mass energy of the photon-photon or photon-parton system. This relative luminosity is equal to (considering the Q^2-dependence of the fluxes has been integrated out):

$$\mathcal{N}(W) = \int_{x_1}\int_{x_2} \frac{dN}{dx_1}\frac{dN}{dx_2}\delta(W - 2E\sqrt{x_1 x_2})dx_1 dx_2 \tag{1.22}$$

Where the dN fluxes can correspond to photon or parton functions and the integration boundaries naturally go from 0 to 1. However, if one uses forward detectors to detect surviving protons, the energy acceptance of these is limited and the integration range for photon fluxes have to be fixed according to the acceptance of the detectors. It should also be noted that in case of asymmetric events, like photon-quark interactions for instance, this formula only gives one case ($\gamma q \to X$), and the obtained luminosity should then be doubled in order to take the symmetric case into account. Figures 1.15 and 1.16 show the luminosity $\mathcal{N}(W)$.

1.3.6 Cross-section computation

In the EPA framework, the proton-proton cross-section for a process happening through given photon-quark or photon-photon interaction is:

$$\gamma\gamma \quad : \quad d\sigma_{pp} = \sigma_{\gamma\gamma}(E, x_1, x_2, Q_1^2, Q_2^2)dN_1(x_1, Q_1^2)dN_2(x_2, Q_2^2) \tag{1.23}$$

$$\gamma p \quad : \quad d\sigma_{pp} = \sigma_{\gamma p}(E, x, Q^2)dN(x, Q^2) \tag{1.24}$$

For many processes for which the cross-section is weakly dependent on the photon virtuality, one can use the Q^2-integrated flux. In the case of photon-photon interactions we are then interested in the two-photon centre of mass energy spectrum $\mathcal{N}(W)$. This spectrum is computed by integrating over x while keeping W constant. From equation 1.22, one gets:

$$\mathcal{N}(W) = \int_{x_{min}}^{1} \frac{dN}{dx}(x)\ \frac{dN}{dx}(\frac{W^2}{4E^2 x})\ \frac{2W}{4E^2 x}dx \tag{1.25}$$

Which should then be convolved with the cross-section of the photon-photon process as follows:

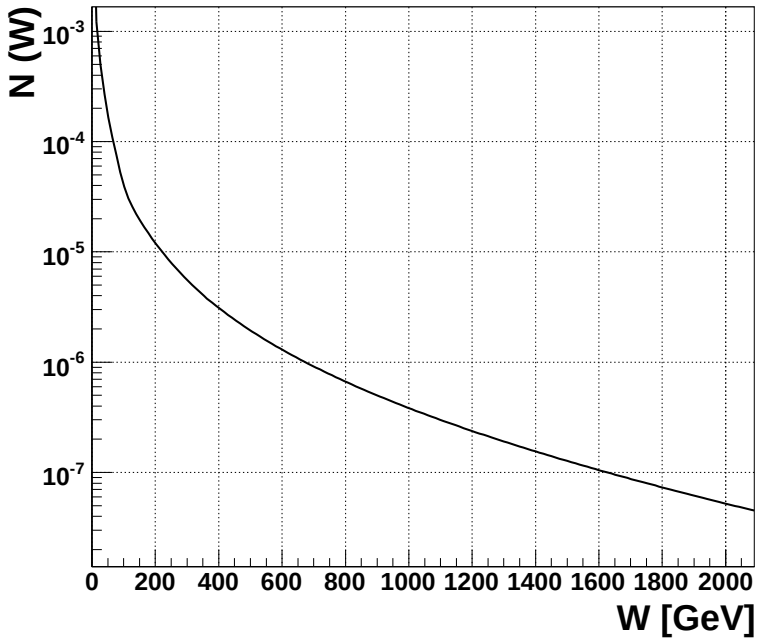

Figure 1.15: Relative luminosity $\mathcal{N}(W)$ for elastic photon-photon interactions at the LHC.

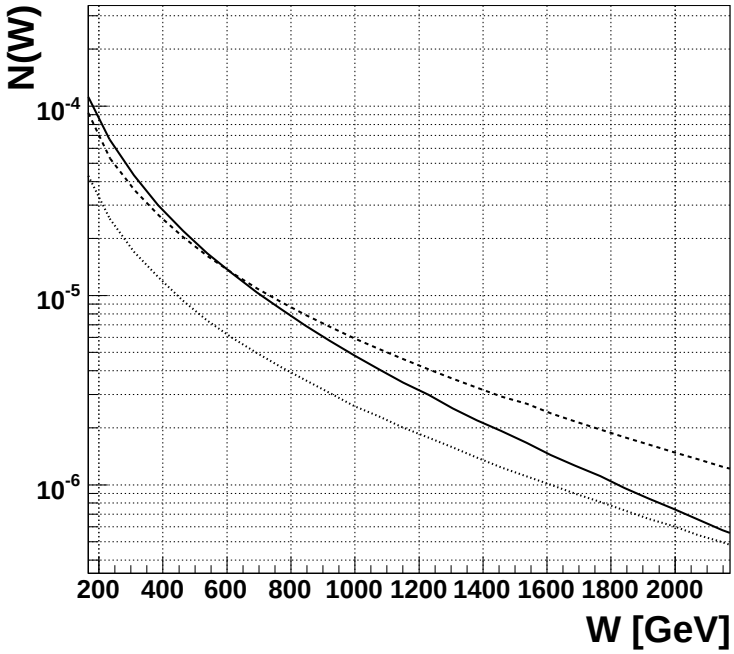

Figure 1.16: Relative luminosity $\mathcal{N}(W)$ for photon-gluon (plain) and photon-quark interactions at the LHC. Here only the up (dashed) and down (dotted) quark contents were considered.

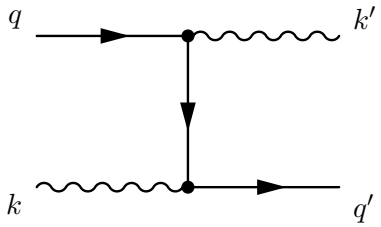

Figure 1.17: Typical t-channel process via photon-proton interaction.

$$\sigma_{pp} = \int_{W_0}^{\sqrt{s}} \sigma_{\gamma\gamma}(W) \, \frac{d\mathcal{N}}{dW} dW. \tag{1.26}$$

Examples of cross-sections computed using this technique interfaced into different Monte Carlo generators will be shown in chapter 4.

1.3.7 Resolved photons

A particular issue of photoproduction processes is the singularity that appears in t-channel processes of the kind shown on Fig. 1.17 when the outgoing quark is massless and collinear with the incoming photon, because of the t-channel quark propagator [31].

At high momentum transfer $t = (q - q')^2 = (k - k')^2$, i.e. if one requires sufficient transverse momentum for the outgoing quark, this singularity does not affect the cross-section. At low momentum transfer, the cross-section rises as the angle between the photon and the quark approaches zero. This is due to the fact that quarks colinear with the incoming photon are predominantly coming from $q\bar{q}$ fluctuations of the photon. By looking at such events, one effectively probes the hadronic structure of the photon, which is dominated by non perturbative QCD contributions. Such events were observed at LEP [32] and HERA [33, 34] through the presence of a "photon remnant", reflecting the hadronic nature of the interaction. The usual way to deal with this is to extract the singularity and re-absorb it into the quark content of the photon, as shown if fig. 1.18, following the Modified Minimal Substraction ($\overline{MS}$) scheme prescriptions. This procedure also introduces a factorisation scale μ_F.

This leads to the separation of the cross-section into two different regimes, in which no singularity now appear. The high momentum transfer regime, for which the calculation uses the t-channel diagram shown before including the singularity extraction, is called the *direct photon* component of the cross-section. In the low momentum transfer

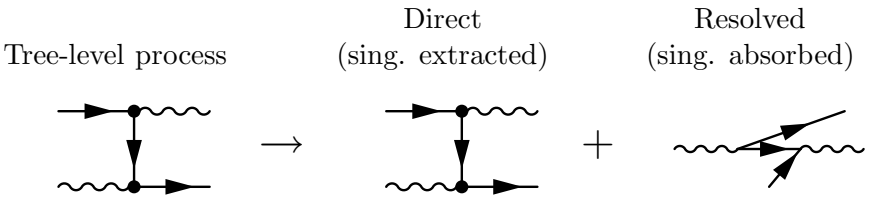

Figure 1.18: Illustration of the singularity extraction for the W + quark photoproduction.

regime, the incoming particle is a quark coming from the photon and this contribution is henceforth called the *resolved contribution*.

The cross-section computation is then usually done by placing a cut to divide the phase space between the two regimes and computing the sum of both cross-sections as if they were initiated by completely different processes.

In all practical cases, it is thus important to determine how important the contribution from resolved photons is and to compute it if it appears to be non-negligible. It is the case for instance in the case of W boson production at HERA treated in chapter 2 as no cut is placed on the transverse momentum of either the W boson or the outgoing quark.

1.4 Anomalous couplings involving photons

Two physics cases for which photon interactions offer a window to beyond the Standard Model physics are presented in this section.

1.4.1 Anomalous gauge couplings

One of the consequences of the non-abelian SU(2) x U(1) structure of the standard model is the existence of couplings between the gauge bosons. In the SM, as far as the photon is concerned, three different couplings occur at tree-level: the triple coupling γWW and the two quartic couplings $WWZ\gamma$ and $WW\gamma\gamma$.

If new physics appears above some energy scale, it may change the value of these couplings. This is generally modelled by effective couplings representing the integration of possible beyond the SM contributions. A measurement of these couplings thus represents a test of the standard model and a probe of new models. Measurements have been performed

at LEP [38, 39, 40] through W pair production associated or not with a photon. Studies have also taken place at HERA and the Tevatron [37].

At the LHC anomalous gauge couplings can be studied through multi-boson production processes [41]. Photon interactions also offer the opportunity to put more stringent limits on these effective couplings especially through process of the type $\gamma\gamma \rightarrow W^+W^-$ which are very sensitive to any anomalous coupling, especially the quartic ones [42].

The present dissertation focuses on photoproduction of events containing a W boson. Those are thus sensitive to variations of the triple gauge couplings. The effect of potential new physics is usually described in a general way by the following effective Lagrangian:

$$\mathcal{L} = e\left[\left(W^{\dagger}_{\mu\nu}W^{\mu} - W^{\dagger\mu}W_{\mu\nu}\right)A^{\nu} + \kappa W^{\dagger}_{\mu}W_{\nu}F^{\mu\nu} + \frac{\lambda}{M_W^2}W^{\dagger}_{\rho\mu}W^{\mu}_{\nu}F^{\rho\nu}\right]. \tag{1.27}$$

Where $W_{\mu\nu} = \partial_\mu W_\nu - \partial_\nu W_\mu$, $F^{\mu\nu}$ is the photon tensor and, in the standard model, $\lambda = 0$ and $\kappa = 1$. The present measurements resulting from LEP combined analysis are the following:

$$\begin{aligned} \kappa &= 0.973^{+0.044}_{-0.045} \\ \lambda &= -0.028^{+0.020}_{-0.021} \end{aligned}$$

which are compatible with the Standard Model expectations.

1.4.2 Flavour-Changing Neutral Currents

As a direct consequence of the structure of the SM Lagrangian, flavour is conserved by interaction via neutral currents at tree-level. As charged currents do not preserve flavour, one-loop corrections of the kind shown in Fig. 1.19 introduce flavour changing neutral currents (FCNC). However, such interactions are heavily suppressed due to the GIM [43] mechanism.

In history

Because of the very low probability of such processes, Standard Model FCNC are hard to observe experimentally. The first observation was made by the CLEO [47] collaboration in 1993, studying the processes:

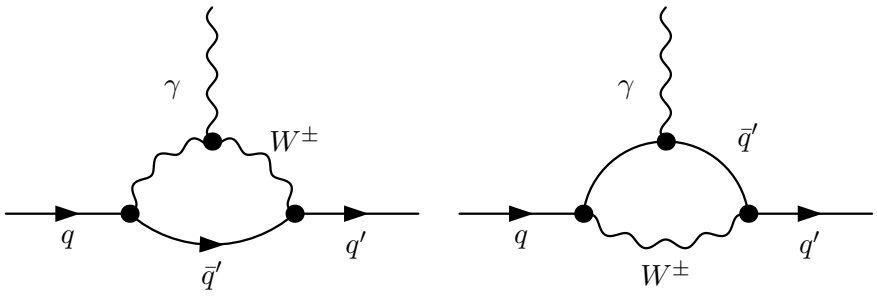

Figure 1.19: One-loop diagrams for FCNC in the SM

$D^0 \to l^+l^-$ and $D \to Xl^+l^-$ and thus probing the $c \to \gamma u$ and $c \to Z^0 u$ branching ratios.

Other studies were done at CLEO [48], BaBar [49] and E949 [50] collaborations focusing on the b and c quarks-based mesons decays via FCNC. No deviation from SM prediction has been found yet.

In theory

FCNC could be far stronger in some models than they are in the SM. By looking for FCNC-induced processes, one can then probe those models efficiently. The most common models allowing important FCNC are the following ones:

1. Multi-Higgs models can in some cases give rise to important FCNC. Usually, multi Higgs-doublet models contain additional symmetries to prevent the existence of FCNC, namely same charge quarks interact only with one of the doublets. Releasing this constraint leads to the appearance at tree-level of couplings of type $q\bar{q}'H^{\pm}$, which lead to great enhancements of the higher order contributions of $\gamma qq'$ and Zqq' through diagrams such as Diag. 1.20.

2. Supersymmetry provides some more opportunities to see FCNC appear at next to leading order (NLO), through quark-squark-neutralino and quark-squark-gluino couplings, in addition to the ones induced by charged Higgs bosons [44].

3. Exotic quarks predicted by some Grand Unification and string theories [45] could mix with the SM quarks and enhance FCNC

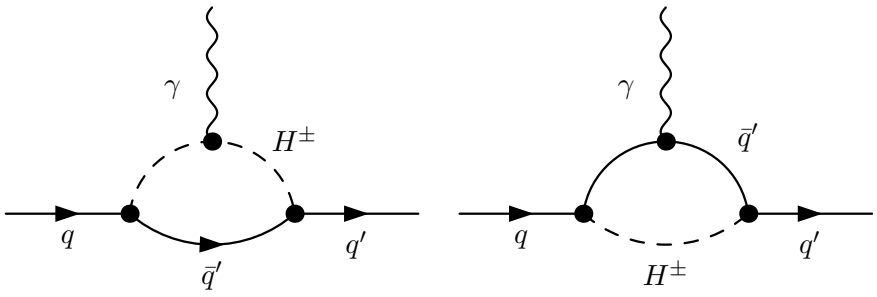

Figure 1.20: One-loop diagrams for FCNC in Multi-Higgs Models

couplings through the non-unitarity of the CKM matrix, especially when dealing with heavy quarks.

4. Technicolor/Topcolor also allows for important FCNC in the top quark sector through top-pion Yukawa couplings [46].

In the latter two, the top quark sector is especially sensitive to FCNC, while in the other models all generations are similarly affected. Constraints based on light quarks do not affect Exotic quarks and technicolor based FCNC, and one should then probe directly the top sector in order to get measurements effectively constraining these models.

1.4.3 Anomalous single top production

One of the consequences of important FCNC would be an enhancement of the production cross-section for single top quarks at all colliders, through $tu\gamma$, $tc\gamma$, tuZ^0 and tcZ^0 enhanced couplings. A summary of branching ratios of top decays to a charm quark and a photon is given as an illustration in table 1.4 for the main theories predicting FCNC as described previously. In a general way, one uses an effective Lagrangian to describe such couplings. The most general, CP-conserving Lagrangian is given by:

Model	SM	MHDM	MSSM	Technicolor	Exotic quarks
$B_{(t\to\gamma c)}$	$\mathcal{O}(10^{-12})$	$\mathcal{O}(10^{-8})$	$\mathcal{O}(10^{-8})$	$\mathcal{O}(10^{-8})$	$\mathcal{O}(10^{-7})$
$k_{tc\gamma}$	$\mathcal{O}(10^{-7})$	$\mathcal{O}(10^{-4})$	$\mathcal{O}(10^{-4})$	$\mathcal{O}(10^{-3})$	$\mathcal{O}(10^{-3})$

Table 1.4: Maximum FCNC decay branching ratio and couplings of the top quark in some models.

$$\begin{aligned} L &= i\, e_t\, \bar{t}\, \frac{\sigma_{\mu\nu} q^{\nu}}{\Lambda}\, k_{tu\gamma}\, u\, A^{\mu} \\ &+ i\, e_t\, \bar{t}\, \frac{\sigma_{\mu\nu} q^{\nu}}{\Lambda}\, k_{tc\gamma}\, c\, A^{\mu} \\ &+ \frac{g}{2\cos\theta_W}\, \bar{t}\, \gamma_{\mu}\, v_{tuZ}\, u\, Z^{\mu} \\ &+ \frac{g}{2\cos\theta_W}\, \bar{t}\, \gamma_{\mu}\, v_{tcZ}\, c\, Z^{\mu} + h.c. \end{aligned} \tag{1.28}$$

where q^{ν} is the 4-vector of the photon, g is the weak coupling, θ_W is the weak mixing angle and Λ is the energy scale, usually taken as the top mass. The couplings are real and positive. The Lagrangian allows to predict the cross-section for single top quarks production through FCNC and consequently, measurements at colliders lead to limits on the anomalous couplings k and v.

At LEP

At the CERN electron-positron collider, all four experiments (ALEPH [54], DELPHI [52], L3 [53] and OPAL [55]) searched for single top quarks. The observed channel was the associated production of a top quark with an up or a charm quark as illustrated by Fig. 1.21. This search is sensitive to the four anomalous couplings described by the Lagrangian. No excess was found with respect to the standard model prediction. The best limits were obtained by the OPAL collaboration. The one-dimensional 95 % C.L limits are $k < 0.37$ and $v < 0.43$.

At HERA

The leading order diagram for anomalous single top production at HERA is shown on Fig. 1.22. Both the ZEUS and H1 [56] collaborations per-

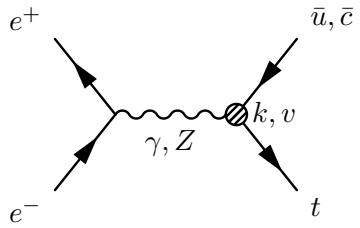

Figure 1.21: Single top production at LEP through flavour changing neutral currents.

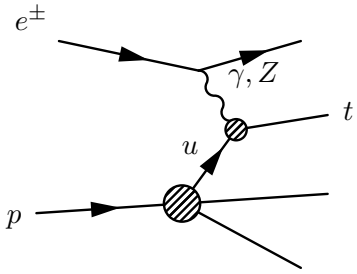

Figure 1.22: Single top production at HERA through flavour changing neutral currents.

formed studies on this channel, although no combined analysis is available yet. The main difference between this study and the one performed at LEP is that due to the high mass of the top quark, the energy fraction of the boson has to be important, which nullifies the contribution of charm quarks. This analysis is thus only sensitive to the couplings $k_{tu\gamma}$ and $v_{tu\gamma}$. The most recent results from the H1 collaboration including all the HERA data provides the best actual limit on the coupling $k_{tu\gamma}$ of 0.14.

At the Tevatron

The CDF [57] experiment at the Tevatron looked at FCNC decays of the top quarks (see Fig. 1.23) in $p\bar{p}$ collisions. The branching ratio of the top to a photon or a Z boson and a quark was computed by comparing the number of FCNC decay candidates with the $t\bar{t}$ normalisation sample. Using a 110 pb^{-1} of accumulated data, one candidate was observed in each of the two decay modes (γ and Z), leading to the following limits on the branching ratios:

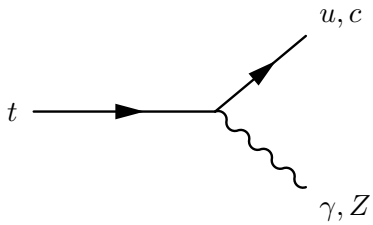

Figure 1.23: FCNC decay of a top quark

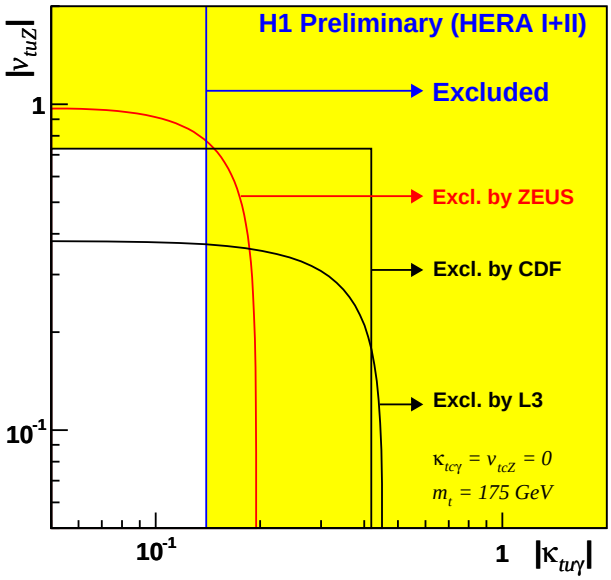

Figure 1.24: Current limits on the anomalous couplings $k_{tu\gamma}$ and v_{tuZ}

$$\begin{aligned} B(t \to c\gamma) + B(t \to u\gamma) &< 3.2\% \\ B(t \to cZ) + B(t \to uZ) &< 33\% \end{aligned}$$

These can be translated into limits on the anomalous couplings: $k < 0.4$ and $v < 0.7$ at 95 % C.L. The limits obtained by the various experiments are summarised on Fig. 1.24.

These limits are still orders of magnitude higher than the values expected from various BSM cases. One thus wants to use the assets of the LHC in order to improve the limits on the anomalous couplings. Photoproduction appears as a natural candidate to achieve this task as it involves direct couplings of the photon to quarks or gauge bosons.

Such a process where anomalous couplings can have important influence on the cross-section is the production of W bosons at HERA, part of which happens through the γWW coupling. This process is studied in the next chapter.

Chapter 2

W boson production at HERA

2.1 Motivation

Despite its rather small cross-section of 1 pb, W boson production at HERA is a very important process in many ways. It occurs via various diagrams among which one is dependent on the γWW vertex (Fig. 2.1), an important prediction of the Standard Model, which makes a measurement of the cross-section a nice test of the model.

Leptonic decays of the produced W boson give birth to topologies very similar to the ones predicted by various models, like some supersymmetric models or the effect of flavour changing neutral currents. In these cases, along with an isolated electron or muon, one expects to see hadronic activity with important transverse momentum. For instance, in the FCNC photoproduction of a single top quark, the latter decays into a W boson and a jet. Given the mass of the top quark, the jet is expected to bear important transverse momentum. Consequently, the observation of high P_T hadronic activity would be an important hint for beyond the SM physics.

Moreover, previous studies by the H1 collaboration [59, 60, 61] showed excesses of isolated lepton events with important transverse momentum of the hadronic final states P_T^X. These excesses were not confirmed by ZEUS measurements. This subject has thus become one of the main priorities of both collaborations. A measurement is presented, based on the data gathered by the ZEUS collaboration between 1996 and 2000 and between 2003 and 2004, looking at isolated electrons associated with missing transverse momentum in various running conditions: in 1998

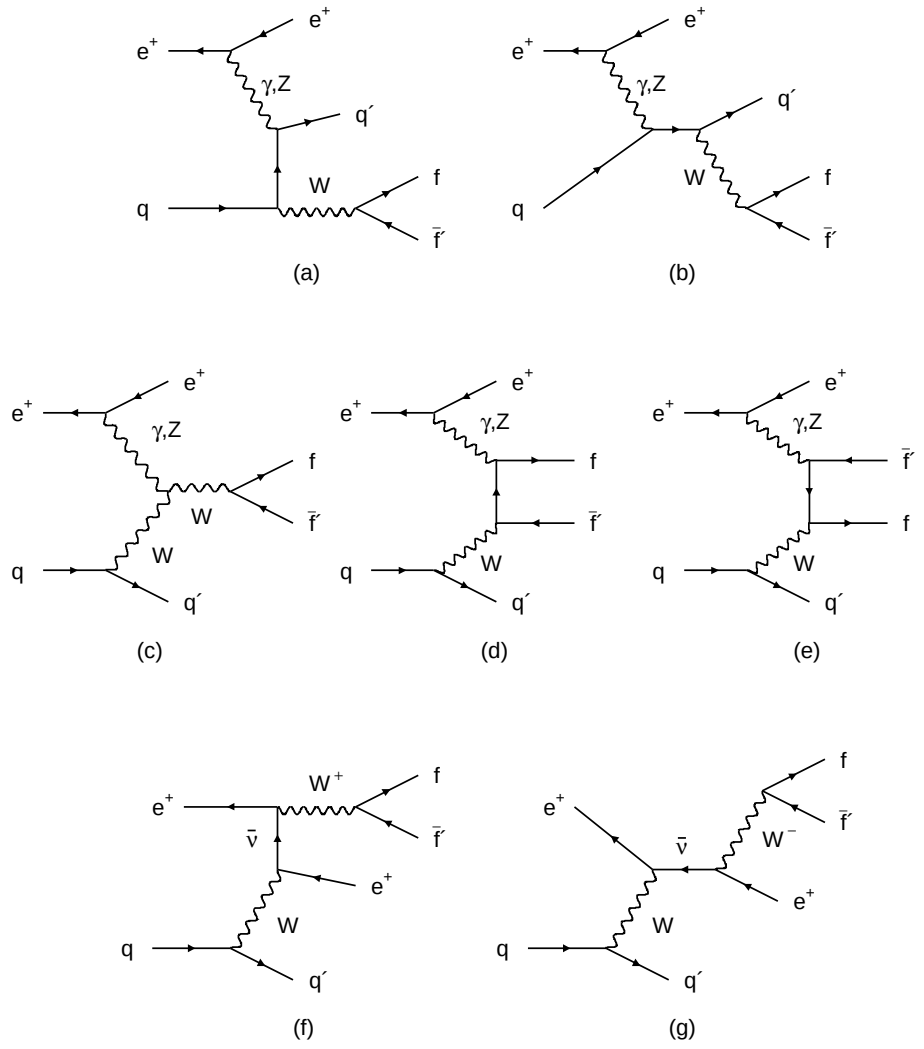

Figure 2.1: Diagrams for W boson production in the Standard Model with the subsequent decay to fermions. The process $ep \to \nu_e W X$ is not depicted. Diagram (c) is sensitive to possible anomalous triple gauge couplings. Diagrams (d) and (e) are included to preserve gauge invariance. The present analysis only focuses on final states including an electron and a neutrino.

and part of 1999 an electron beam was used, while in other samples only a positron beam is used. Finally, from 2003 onwards the beam gets polarised which also affects the cross-sections of both signal and background processes. The present work became part of a wider project including more data, the decay of W bosons into muons and a joint analysis with the H1 collaboration [62].

2.2 The ZEUS detector

The ZEUS detector [63, 64], depicted on Fig. 2.2, is a multi-purpose detector. Its design is asymmetric because of the natural boost of the final states in the direction of the outgoing proton. Its operation started in 1992, and it evolved later by the addition and modification of many subdetectors. From the inner to the outer side, one finds close to the beam a vertex detector (VXD till 1996, then replaced by the microvertex detector MVD) enveloped by the drift chamber forming the central tracking detector (CTD) and the calorimeter (CAL). Between these two lies the coil providing a 1.43 T magnetic field. Both CTD and CAL have extensions in the forward (proton direction) and backward regions. The return yoke is the next layer and also contains detectors (BAC - the "backing" calorimeter) with the purpose of detecting particles not stopped in the CAL. Muon chambers form the last detector layer while the whole detector is covered by a concrete shielding.

Additional detector components are placed around the central detector in order to control the conditions of operation. On the proton side, the so-called VETO wall controls beam-induced events happening before the beam enters the detector. On the same side, the beam pipe tracker and beam pipe calorimeter aim at detecting the outgoing electrons scattered at low angle, while very forward detectors are placed at 34 m and 107 m from the IP for luminosity measurements and tagging photoproduction events. On the other side, proton remnant taggers are placed at 5 m and 24 m from the IP, followed by two roman pots stations. Finally, the leading proton spectrometer consisting of six detectors stations placed between 24 m and 90 m from the IP detects protons with very low transverse momentum.

The present analysis is mainly based on three subdetectors: the microvertex detector, the central tracking device and the calorimeter.

MVD: The vertex detector [65] of ZEUS consists of two parts, a 'barrel'

part , 65 cm long, around the beam pipe and a disk to close the barrel in the forward direction. The barrel consists of three layers of silicon strip detectors, while the forward part is made of four wheels of sensors. Each wheel consists of 14 trapezoidal parts. The optimal resolution of the detector is around 50 μm and the probability of missing hit in a detector plane is below 10^{-3}. The resolution on the reconstructed position of a vertex is around 150 μm.

CTD: The tracking detector [66] is made of a cylindrical 2 m long and 1.6 m wide wire chamber filled with argon, methane and carbon dioxide. The wires are organised in 9 superlayers (SL) of 8 wire layers each. Odd number SLs are parallel to the beam while even SL are tilted by 5 degrees in order to provide a longitudinal (z) position measurement. A timing measurement is also used to determine this position, mainly for trigger purposes. The overall P_T reconstruction resolution is $\Delta P_T = 0.0014 + 0.0065\ P_T + 0.0058\ P_T^2$ if P_T is given in GeV.

CAL: The calorimeter [67] is made of three parts, a barrel around the CTD and two endcaps to close the volume in the forward and backward directions. It is made of depleted uranium alternating with scintillating layers. This design allows, by a particular balancing of the two types of layers, to obtain a *compensating* calorimeter, meaning that electrons and hadrons of similar energies deposit the same energy in the detector. The energy resolution is $\Delta E_e = 0.18\sqrt{E}$ for electrons and $\Delta E_h = 0.35\sqrt{E}$ for hadrons.

Trigger system

At ZEUS, few (~ 5) events per second can be written to disk because of technical limitations. As the frequency of events is orders of magnitude higher (10 MHz of bunch-crossings and 10 KHz event rate for beam-gas interactions alone), a strong preselection has to take place before the data acquisition. This is achieved through a three-stage trigger system.

The first level consists of two parts: local hardware triggers respond to each component measurement, while all the responses are gathered by the global first level trigger (GFLT) which reduces the event rate to around 1 KHz. At the second level, local quantities are reprocessed using more information. This more accurate analysis allows to reduce

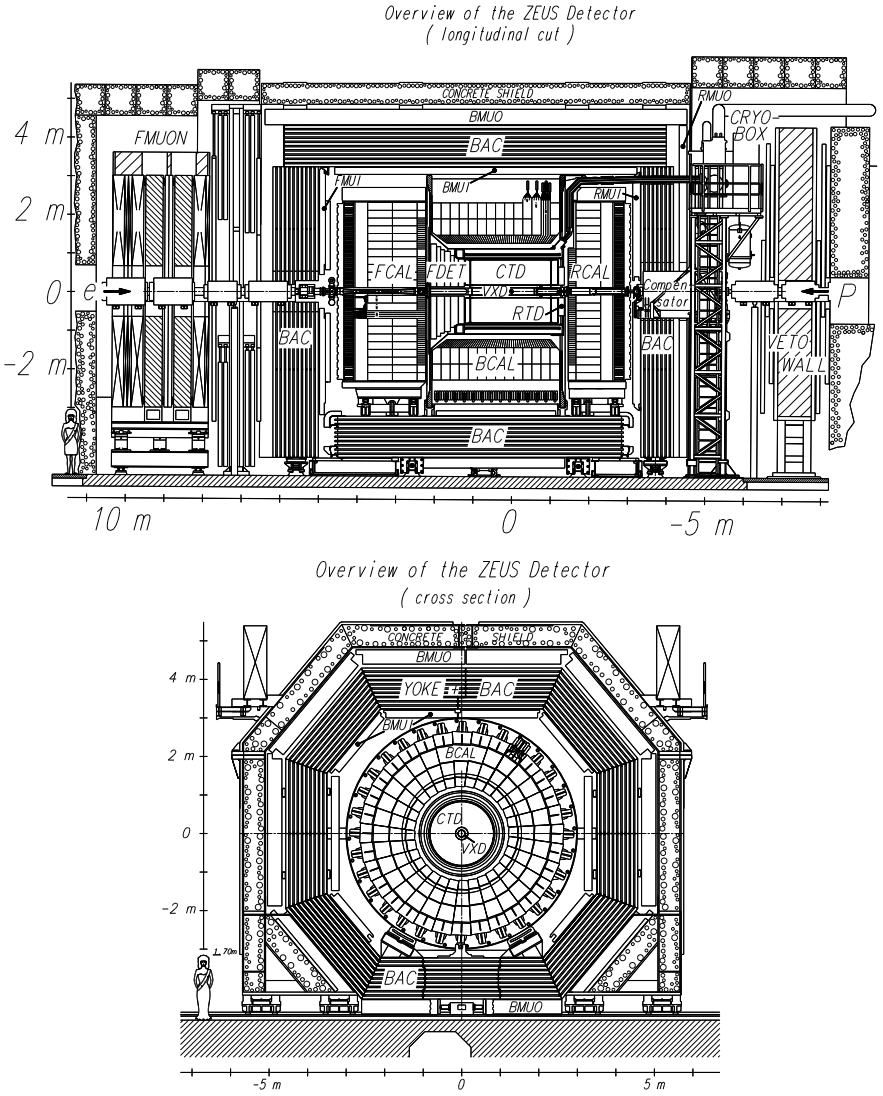

Figure 2.2: Side (top) and front (bottom) cuts of the ZEUS detector

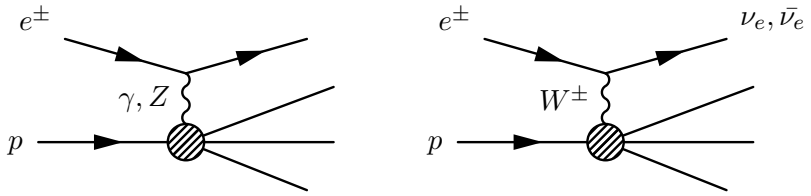

Figure 2.3: Deeply inelastic neutral current (left) and charged current (right) interactions at HERA.

the rate to around 50 Hz. Eventually, data from all detector components are gathered into a single event file which is analysed by the third level of the trigger. The final output rate is around 5 Hz.

2.3 Background

The main background in this study is due to neutral current and charged current deep-inelastic processes shown in Fig. 2.3. Although these do not have the same topology as the studied signal process, their cross-sections are sufficiently high to provide an important rate of fake W events. In the case of neutral current (NC), a genuine electron is detected while the missing transverse energy P_T^{miss} comes from detector effects. Charged current events (CC) on the contrary do possess missing transverse energy while the detected electron is coming from mismeasurements.

Beside these dominant processes, the dilepton photoproduction of Fig. 2.4 also contributes if one of the leptons is not detected. Another source may come from Z boson production: if the Z decays into neutrinos and the momentum transfer is sufficient, the beam electron can be detected in the central detector and associated to some missing transverse energy. However, the cross-section for this process is expected to of the order of 3 % of the signal cross-section and it was thus neglected in the present analysis.

2.4 Simulation

2.4.1 Signal

In order to simulate the Standard Model production of W boson through the diagrams of Fig. 2.1, the EPVEC [68] program was used. It was also

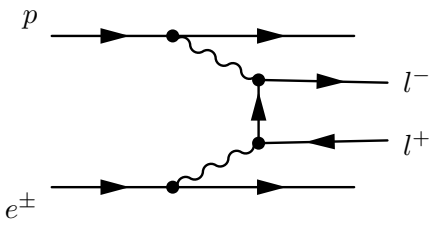

Figure 2.4: Two-photon production of a lepton pair at HERA (with elastic photon emission by the proton).

used to estimate the cross-section of the $ep \to \nu_e WX$ process in which the W boson couples directly to the incoming electron. This process accounts for approximately 7 % of the total W production cross-section.

Next to leading order calculations described in [31] were also included by reweighting the events using the W boson 4-momentum. These corrections do not affect significantly the overall cross-section of 1.1 (1.3) pb at a centre of mass energy of 300 (318) GeV.

As detailed in the previous chapter, the simulation of this process requires to deal with singularities in the differential cross-section at low momentum transfer of the photon. Two different samples were thus defined according to the momentum transfer $t = (p_q - p_W)^2$ of the incoming quark to the W boson: processes with $|t| < 25$ GeV^2 were simulated using a resolved photon model (RES), while direct photon (DIS) simulation was used at higher $|t|$. The contribution of resolved photons is important as events with very low momentum transfer may be selected due to the lack of a cut on the transverse momentum of the W boson or the hadronic system. The size and the cross-section associated with each subsample are shown in table 2.1.

2.4.2 Background

The neutral and charged current processes were generated using Django6 [69]. This Monte Carlo program uses the Heracles [72] and Lepto [73] softwares in order to simulate electron-proton interactions while taking into account one-loop electroweak radiative corrections. Higher-order QCD effects were simulated using ARIADNE while for the final state hadronisation, JETSET [75] was interfaced to Django6. Dilepton samples were generated using the GRAPE generator.

The description of all used samples can be seen on table 2.2.

Subprocess	cross-section [pb] (sample size)			
	96-97 (e^+)	98-99 (e^-)	99-00 (e^+)	03-04 (e^+)
$ep \to W^+$(DIS)	0.39 (20k)	0.46 (50k)	0.49 (10k)	0.47 (50k)
$ep \to W^-$(DIS)	0.32 (20k)	0.43 (50k)	0.40 (10k)	0.43 (50k)
$ep \to W^+$(RES)	0.13 (10k)	0.08 (50k)	0.15 (10k)	0.08 (10k)
$ep \to W^-$(RES)	0.10 (10k)	0.11 (50k)	0.12 (10k)	0.11 (10k)

Table 2.1: Signal subsamples simulated with EPVEC.

Subprocess	cross-section [pb] (sample size)			
	96-97 (e^+)	98-99 (e^-)	99-00 (e^+)	03-04 (e^+)
NC ($Q^2 > 400$ GeV^2)	1097.1 (620k)	1196.8 (200k)	1167.6 (400k)	1167.7 (120k)
NC ($Q^2 > 1250$ GeV^2)	-	216.7 (100k)	-	197.4 (50k)
NC ($Q^2 > 2500$ GeV^2)	-	71.7 (10k)	-	58.9 (24k)
NC ($Q^2 > 5000$ GeV^2)	-	-	-	14.8 (24k)
CC ($Q^2 > 10$ GeV^2)	41.4 (50k)	79.0 (25k)	45.2 (250k)	44.9 (250k)
dileptons ($P_T > 5$ GeV)	30.2 (46k)	31.6 (46k)	33.6 (65k)	34.2 (210k)

Table 2.2: List of the simulated background samples along with their associated cross-section and sample size.

2.4.3 Detector simulation

In order to compare data and the Monte Carlo (MC) simulations described in the previous sections, a full simulation of the ZEUS detector was used. This was achieved by two main programs: MOZART and CZAR. The MOZART software simulates two different steps: first, interactions between the particles and the detector are simulated using Geant 3 [70], including magnetic field and energy deposits. Then the response of the readout electronics is simulated. CZAR uses this information to simulate the trigger functions. Afterwards, the information is treated in the exact same way as real data to reconstruct the physics observables by the ZEPHYR software.

2.5 Event reconstruction and selection

2.5.1 Cosmic and beam-gas events rejection

The first step in the event selection procedure is to get rid of events not linked to electron-proton interactions, such as beam-gas events or cosmic muons. The rejection of cosmic muons is based on a timing measurement from the calorimeter: first, the hits should not be delayed by more than 6 ns with respect to the bunch-crossing timing. Additionally, it is expected that muons crossing the detector vertically or horizontally give birth to two deposits with some delay due to the time of flight, while in electron-proton events the deposits are expected to be simultaneous. The delay between two hits, either in the upper and lower half of the CAL or in the forward and backward parts, is thus required to be smaller than 6 ns.

Beam-gas events are treated by counting the number of "good" tracks among the tracks measured by the CTD. Good tracks are defined as central ($15 < \theta_{track} < 165$) primary vertex tracks with P_T greater than 0.2 GeV. It is then required that at least one good track is found, and that the total number of tracks is such that:

$$N_{total} < 20 + 5 \times N_{good}. \tag{2.1}$$

This condition is based on the observation of data and is illustrated on Fig. 2.5.

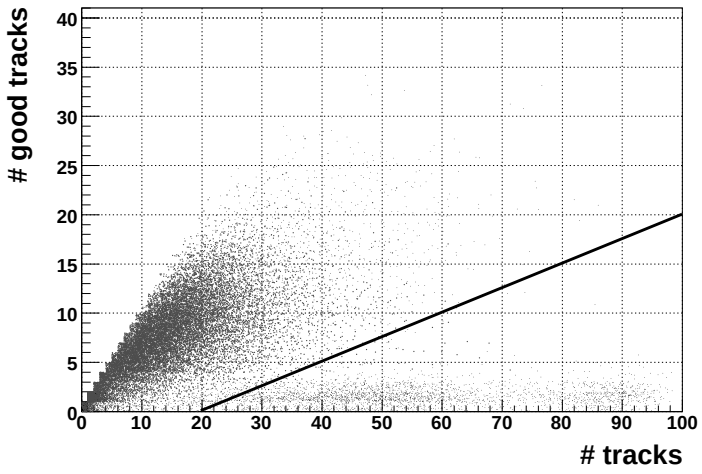

Figure 2.5: Number of good tracks versus the total number of tracks for beam-gas events. The line represents the condition described by equation 2.1. One clearly sees the separation between beam-gas induced events (lower right) and physical events.

2.5.2 Preselection

A preselection is applied in order to restrict the sample to events with missing transverse momentum and compare the selected sample with Monte Carlo simulations in order to validate it. This preselection consists of various trigger conditions aiming at the selection of charged current events, in addition with some CAL-based reconstructed variables. The total missing transverse momentum P_T^{CAL} of the event is reconstructed from the calorimeter cells by summing over all the energy deposits:

$$P_T^{CAL} = \sqrt{\left(\sum_i P_{x,i}^{cal}\right)^2 + \left(\sum_i P_{y,i}^{cal}\right)^2} \tag{2.2}$$

Where $P_{x,i}^{cal} = E_i \sin\theta_i \cos\phi_i$ and $P_{y,i}^{cal} = E_i \sin\theta_i \sin\phi_i$. P_T^{CAL} is required to be greater than 9 GeV in order to suppress neutral current background. The same was done excluding the inner ring of the forward CAL in order to avoid fake missing P_T usually associated with beam-gas events and was also required to exceed 9 GeV. Athough the missing momentum seen in NC events is caused by mismeasurements,

the data is well reproduced by the simulation in this extreme region of phase space . The transverse momentum of the hadronic system P_T^X was defined similarly as the sum over all calorimeter cells not associated to the electron candidate.

The CAL cells allow to reconstruct the difference between the total energy measured and the total longitudinal momentum of the event $E - P_Z = \sum_i E_i(1 - \cos\theta_i)$. If all final states are identified this variable is expected to lie around[1] 55 GeV. Higher values would be significant of bad reconstruction of the forward and backward CAL energies and are not well reproduced by detector simulation, while beam-gas events typically show a value close to zero. The value of this variable was thus requested to lie between 5 and 60 GeV. Finally, the reconstructed position of the main event vertex was required to be less than 50 cm away from the detector centre.

2.5.3 Electron reconstruction

In order to reconstruct the isolated electron, the neural-network based algorithm Sinistra [71] was used. It is trained in order to maximise electron identification and discrimination against hadronic final states. The direction of the lepton was then extracted from its position in the calorimeter and the position of the associated vertex. Further checks were performed in order to reject fake and not isolated electrons: the calorimeter cluster associated with the electron identified by the algorithm was required to have a track within 10 cm. Additionally, a cone was defined around the leading track and the energy associated with the electron and outside this cone was required not to exceed 4 GeV. Another $\eta - \phi$ cone of radius 0.5 was defined around the electron track and it was required that no track with P_T greater than 0.2 GeV took place in that cone.

The so-defined electron was selected if it had a P_T greater than 10 GeV and an η lower than[2] 2 in order to reduce the NC background in which the electron is often scattered in the backward direction. The algorithm provides an estimate of the quality of the candidate related to its probability to correspond to a genuine electron. This value is comprised between 0 for poor candidates and 1 for perfect ones and was

[1] The total total energy is $= E_{proton} + E_{electron}$, while the total longitudinal momentum is $\sim E_{proton} - E_{electron}$. The difference thus approaches twice the electron beam energy if no energy escapes the detector.

[2] η is defined positive in the electron beam direction.

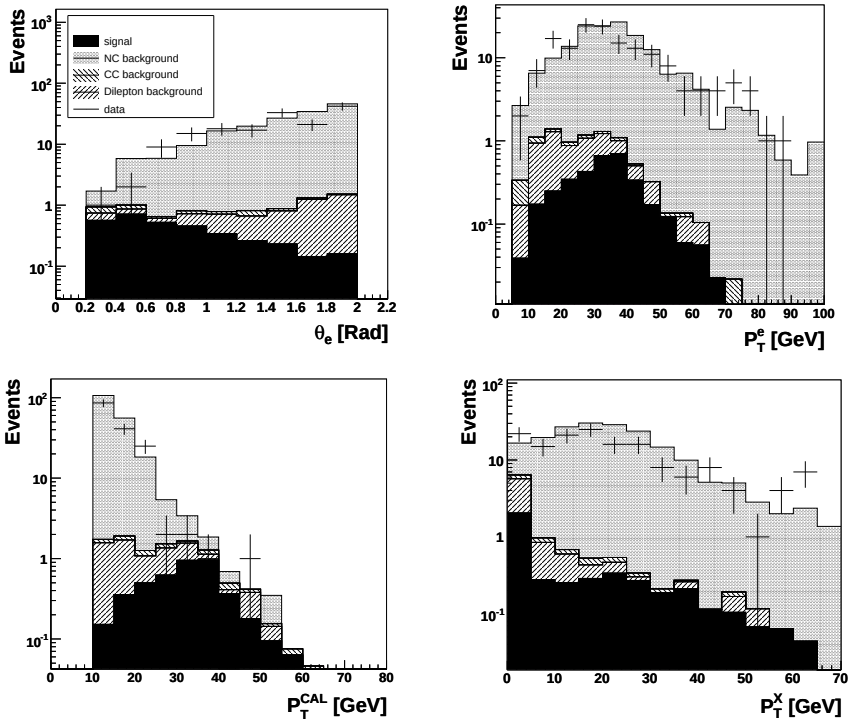

Figure 2.6: Distributions of the isolated electron events compared with the SM expectation for the data taking period 1999-2000 which represents the most important statistics in the present analysis. The error bars on the data points correspond to $\sqrt{N_i}$ where N_i is the number of events in bin i of the histogram.

required to be greater than 0.9. The transverse mass of the neutrino + electron system was reconstructed using the CAL estimation of the missing momentum and the electron candidate. This mass was required to exceed 10 GeV.

The distributions obtained after this preselection are shown on Fig. 2.6. A good agreement between the simulated events and the measured data is found on all distributions in the phase space of interest.

2.5.4 Final selection

In order to reject as much of the NC and CC background as possible, additional cuts were applied on the previously reconstructed variables:

- $P_T^{CAL} > 12$ GeV,
- $\theta_{electron} < 1.5\ rad$,
- $P_T(\text{electron}) > 10$ GeV,
- $P_T^{track}(\text{electron}) > 5$ GeV,
- $E - P_Z < 55$ GeV.

In addition, two variables were reconstructed using the electron candidate: the acoplanarity between the leptonic and hadronic part of the event, and the virtuality of the exchanged particle. The acoplanarity is defined as π minus the angle between the hadronic system and the electron in the transverse plane. This cut aims at reducing the background induced by NC events with fake missing transverse momentum due to bad reconstruction of the hadronic energy. In these cases, the hadronic state is still back to back with the electron in the transverse plane, as shown on Fig. 2.7. In the present case it was required to be higher than 0.3 rad.

The virtuality of the exchanged boson in a neutral current event is given by:

$$Q^2 = 2E_e E_{e'}(1 + \cos\theta_{e'}) \tag{2.3}$$

Where e is the initial beam electron and e' is the outgoing one. The cross-section of NC events strongly favours low values of this variable. In the case of signal events however, this does not represent the virtuality of the interaction and can get very high. As NC events dominate for events with $P_T^{CAL} < 25$GeV the reconstructed virtuality was required to be higher than 5000 GeV^2 for these events. The distribution of the reconstructed Q^2 is shown on Fig. 2.8.

The transverse momentum P_T^X of the hadronic system is, as explained previously, a variable of great interest in the present study. No cuts were applied on this variable, although it was used to separate the final sample in three different regions, namely $P_T^X < 12$ GeV, 12 GeV $< P_T^X <$ 25 GeV and $P_T^X > 25$ GeV as it is in the latter region that the H1 excess was found. An example of a selected event is shown on Fig. 2.9.

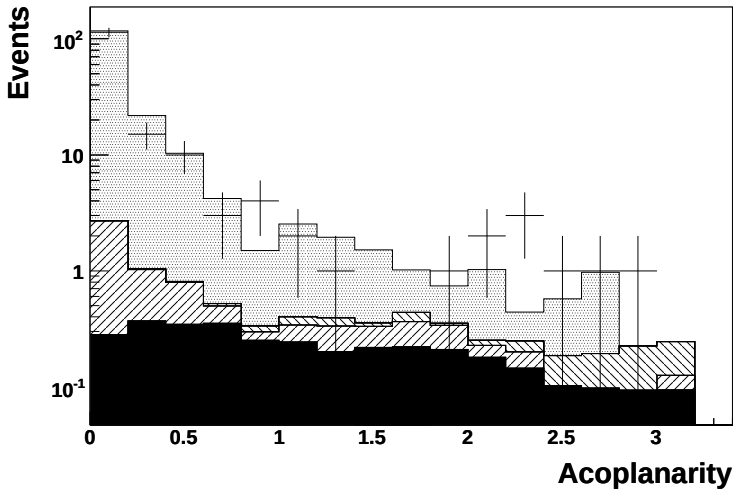

Figure 2.7: Acoplanarity distribution of the isolated electron events compared with the SM expectation for the data taking period 1999-2000

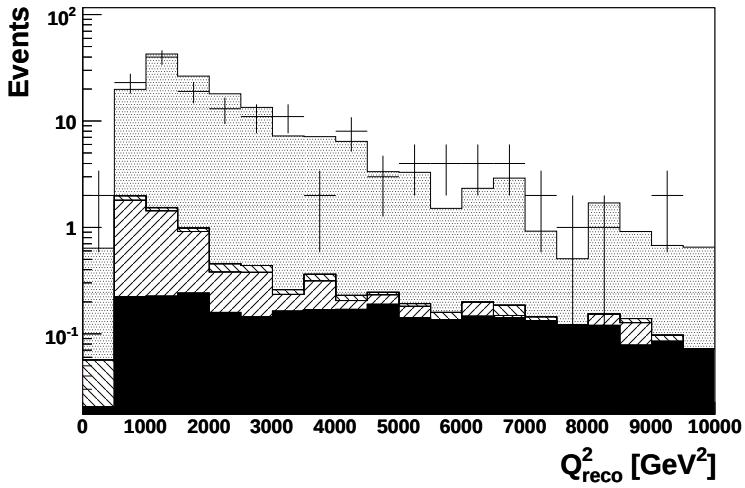

Figure 2.8: Reconstructed Q^2 distribution of the isolated electron events compared with the SM expectation for the data taking period 1999-2000

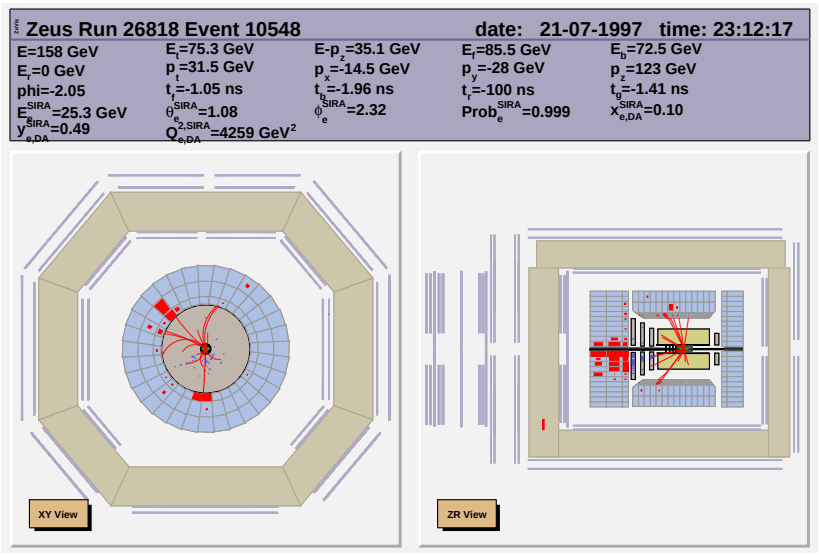

Figure 2.9: Selected event from the 96-97 data taking period. The electron candidate is clearly visible in the lower part of the detector.

2.6 Results and cross-section measurement

2.6.1 Statistical method

As the number of selected events is expected to be distributed according to the Poisson law, the probability of selecting a number n_i of events in a given data taking period denoted by the index i is:

$$P(n_i|\lambda) = \frac{e^{-\lambda}\lambda^{n_i}}{n_i!}. \tag{2.4}$$

The parameter λ is the expected number of events corresponding to $\lambda = B_i + \sigma\varepsilon_i$ where B is the expected background, ε is the signal selection efficiency and σ is the cross-section for W boson production. Using a Bayesian approach with a uniform prior on σ, one can express the total likelihood for the combined samples as:

$$L(\sigma) = \prod_i P(n_i|\lambda(\sigma)) \tag{2.5}$$

In order to take into account the uncertainty δ on the numbers obtained from the selection applied on MC samples, one introduces a Gaus-

Sample	$W^{\pm}$ production	Other SM processes (δ)	Data
96-97 (e^+)	1.00	0.56 (0.16)	2
98-99 (e^-)	0.47	0.12 (0.05)	1
99-00 (e^+)	2.02	1.23 (0.40)	3
03-04 (e^+)	1.22	0.11 (0.09)	0
total	4.71	2.02 (0.44)	6

Table 2.3: Remaining data events and SM expectation after selection for the four periods of data taking. The SM backgrounds are the ones listed in table 2.2.

sian distribution $G(\lambda)$ for the parameter of the Poisson distribution, with the mean defined here above and a width corresponding to the statistical uncertainty on the background estimation. This uncertainty was computed from the weight w_i of the Monte Carlo events using the following formula :

$$\delta = \sqrt{\sum_i w_i^2}. \tag{2.6}$$

Including this effect, the likelihood is thus written as:

$$\mathcal{L}(\sigma) = \prod_i \left[\frac{\int_0^\infty G_i(\lambda) P(n_i|\lambda) d\lambda}{\int_0^\infty G_i(\lambda) d\lambda} \right]. \tag{2.7}$$

The measured cross-section is given by the value of σ which corresponds to the maximum of $\mathcal{L}(\sigma)$, designed as σ_{meas}. The boundaries correspond to values of the cross-section such that $\ln(\mathcal{L}(\sigma_{min,max})) = \ln(\mathcal{L}(\sigma_{meas})) - 0.5$.

2.6.2 Results

The results of the selection are shown on table 2.3. A comparison of data and MC for three P_T^X regions is shown on table 2.4. No significant effect at high P_T^X can be observed.

Combining the likelihood functions associated with these results and assuming a branching ratio of the W boson into an electron and a neutrino of 0.107, one obtains the cross-section measurement:

$$\sigma_W = 0.97^{+0.75}_{-0.57} \text{ pb}$$

	$P_T^X < 12$ GeV	$12 < P_T^X < 25$ GeV	25 GeV $< P_T^X$
MC expected	3.37	1.43	1.93
Data	1	4	1

Table 2.4: Expected MC and observed events for three regions in P_T^X.

which is in agreement with the Standard Model expectation of 1 pb. Unfortunately, due to the important uncertainty, this result does not allow to improve the LEP limits on anomalous triple gauge couplings.

2.6.3 Anomalous single top production

It is interesting to note that the presented search for W bosons is very similar to the search of single top quarks performed by the ZEUS collaboration [76] on the data of the period 1994-2000. W boson production is thus one of the main backgrounds for this study. The fact that the measured cross-section in the W boson search is in agreement with the Standard Model expectations show that this process is well understood and opens the way to BSM searches with similar final states.

Search strategy

The lepton identification part of the single top analysis is very close to the one described previously. The presence of at least a reconstructed central ($-1 < \eta < 2.5$) jet with P_T higher than 40 GeV was required. The reconstructed lepton had to be at a distance exceeding 1 in units of $\eta - \phi$ from any reconstructed jet. No data events survived this selection.

Results

Using a similar statistical method as the one described previously and including NLO corrections, the search for single top quarks with a subsequent decay to leptons lead to a 95 % C.L. one-dimensional limit of $k_{tu\gamma} < 0.247$. Adding the hadronic decay channel, the limit is $k_{tu\gamma} < 0.174$. This limit has been the best until the H1 collaboration recently presented results using the whole set of HERA data [77].

2.7 Summary

The search for single W boson production at HERA lead to the measurement of a cross-section of 0.97 pb, in good agreement with the SM predictions. This agreement holds when adding the other decay channels of the W and the complete set of HERA data, showing that the production of W bosons is well described. It does not confirm the excess of events of this type seen by the H1 collaboration at high P_T^X in e^+p collisions.

This success allows to perform BSM searches such as the anomalous single top search, which leads to results competitive with the ones of the TeVatron (see Fig. 1.24), but also general searches for excesses of various final states.

Chapter 3

Tagging photoproduction at the LHC

One of the main differences between HERA and the LHC when dealing with photoproduction is that at the LHC photon interactions are overwhelmed by partonic processes. While at HERA the study of W production could be done without any tagging procedure, at the LHC the partonic backgrounds will usually dominate photoproduction processes with similar final states by at least three orders of magnitude. One should thus design techniques in order to reduce the impact of these backgrounds.

In the present chapter, we will introduce the various ways one can tag photoproduction (and diffractive) events at the LHC in a similar manner as what has been done at LEP, at HERA and at the Tevatron. Such tagging procedures rely on a particular use of the central detector, complemented or not by very forward detectors.

3.1 Tagging with the central detector

Due to the topology of photoproduction events, it can be possible to select them without any additional instrumentation but a typical '4π' detector of the kind of ATLAS and CMS. This selection is based on the existence of "rapidity gaps" as measured at HERA and described in chapter 1.

3.1.1 Rapidity gaps

The key difference between photoproduction and partonic interactions at the LHC lies in the absence of colour exchange on the photon side. This causes a large zone of rapidity to be completely devoid of hadronic activity, while the colour flow in partonic interactions tends to produce hadrons in the region between the proton remnant and the hard hadronic final states. This region with no hadronic activity is usually called a *large rapidity gap* (LRG) and is a natural way to distinguish between photoproduction and partonic backgrounds.

Gap survival probability

However, the existence of such a gap requires that no additional interaction (*rescattering*) takes place between the two protons simultaneously with the main process. Any colour exchange between the protons would indeed cause the protons to hadronise and the colour flow would naturally cause the region between the protons to be filled with hadronic activity, filling the rapidity gap. This problem is usually reffered as the *gap survival*.

The issue of gap survival appeared when the diffractive parton densities extracted from HERA data [10] were used to predict diffractive event rates at the Tevatron. Factorisation would imply that that these parton densities allow to predict rates for all diffractive processes, independently of the underlying process. However, measurements at Tevatron showed that the observed rates of diffractive processes, selected using a rapidity gap condition, are significantly lower than expected. Exclusive dijets [78] showed an approximately ten times lower rate than expected if factorisation was correct.

This is linked as stated before to the fact that soft rescattering of the protons can appear, leading to the population of the gap by hadronic secondaries. The probability for rescattering not to occur, usually denoted S^2, appears as a correction factor to be applied to the differential cross-section. S^2 is naturally close to one at HERA, while it is small (and process dependent) at hadron colliders. One has:

$$d\sigma_{gap} = d\sigma_{\text{fact.}} \times S^2 \tag{3.1}$$

where σ_{gap} is the observed cross-section requiring a large rapidity gap and $\sigma_{\text{fact.}}$ is the cross-section expected using diffractive parton density functions. The value of S^2 depends on various parameters, mainly the

centre-of-mass energy of the incoming hadrons and the impact parameter distribution of the amplitude of the underlying event, which obviously breaks factorisation.

As introduced by Bjorken [79], the general form for the S^2 factor is given by:

$$S^2 = \frac{\int |\mathcal{M}(b)|^2 \; e^{-\Omega(b)} \; db}{\int |\mathcal{M}(b)|^2 \; db} \tag{3.2}$$

where b is the impact parameter of the interaction and $\mathcal{M}$ the amplitude of the process of interest (in impact parameter space). The function $\Omega(b)$ is called the *optical density* or *opacity* of the particle. The expression $e^{-\Omega(b)}$ denotes the probability that no inelastic interaction takes place at given impact parameter b. It is thus close to one at large values of the impact parameter and low at small b.

The $\mathcal{M}(b)$ distribution is expected to be much wider in quasi-real photon driven interactions than in diffractive interactions, leading to bigger impact parameter[1]. The very strong reduction factors seen in exclusive events at Tevatron should hence not be as limiting in photon-induced interactions at the LHC. For instance, the S^2 factor obtained for exclusive diffractive Higgs boson production at LHC is 0.05 [80] while the same process via $\gamma\gamma$ interaction has a S^2 of around 0.86 [81] (Fig. 3.1). Consequently, the survival probability will not be taken into account in the following analysis. In any cases, it should affect both signal and photoproduction background processes in a similar way.

Another aspect of this issue is the effect of rescattering in inelastic photon emission. Although inelastic emission is not included in the present study, it is interesting to note that rescattering would play an important role in that case too. As computed in the first chapter, the energy spectrum of photons coming from inelastic emission is dependent on the mass of the outgoing system formed by the proton remnant. At low mass, the fragments are scattered at small angles and the rapidity gap requirement can be respected, while at higher masses the system spreads to a large jet which would be detected in forward detectors. Rescattering could play a role a this stage by rising the mass of the remnant and filling the gap. Unfortunately, this matter is very hard to tackle, as it requires a proper understanding and simulation of the underlying event which is, to our knowledge, unavailable at the moment.

[1]The impact parameter is approximately inversely proportional to the square root of the exchanged particle virtuality.

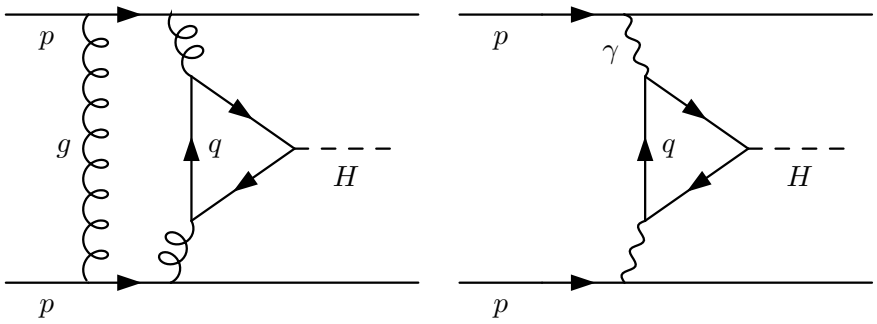

Figure 3.1: Diffractive (left) and two-photon (right) production of a Higgs boson at the LHC

However, clues can be found by looking at the photon energy spectrum as a function of the photon virtuality and of the mass of the proton remnant. As shown on Fig. 3.2, rising the upper bound on the allowed mass for the remnant only affects the high Q^2 region of the spectrum, leaving the low Q^2 region basically untouched. As rescattering affects mainly high Q^2 processes - because the impact parameter grows as the inverse of Q^2 - it also affects only the region sensitive to mass boundary variations. This means that the region where rescattering could fill gaps is the region where gaps are already filled by the high mass of the remnant. One can thus expect a minor contribution from these regions to the cross-section and place a cut at some reasonable mass.

3.1.2 Exclusivity

Another, closely related, consequence of the absence of colour exchange is the overall *exclusivity* of photoproduction events. This means that the only visible objects in the central detectors will be the final products of the main process with only little hadronic contamination, except for the remnant of the strongly-interacting proton. Exclusivity may easily be assessed by counting the visible tracks not associated with a reconstructed final state object in the tracking device.

A positive feature of this method is that if one can reconstruct the vertex of the main process, it does not suffer much of the existence

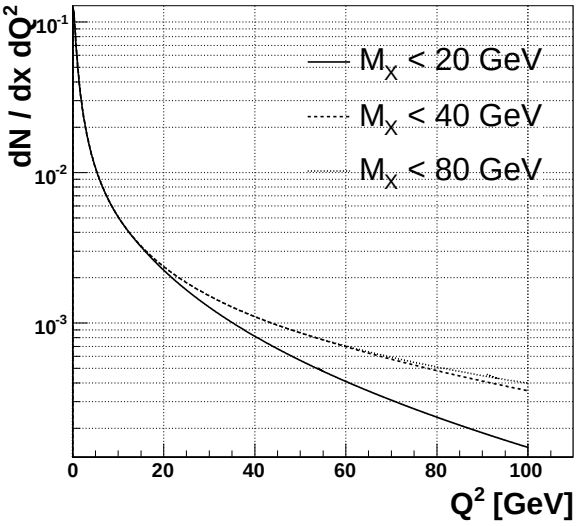

Figure 3.2: Photon energy spectrum as a function of the virtuality of the emitted photon in the case of inelastic photon emission.

of pile-up. One can indeed only look for tracks associated with the main vertex, ignoring any other source of tracks and therefore avoiding influence from pile-up events.

This influence can be estimated from the longitudinal extension σ_z of the interaction regions of ATLAS and CMS and the single track longitudinal position reconstruction resolution. This resolution for CMS is shown of Fig. 3.3. Given that $\sigma_z = 53$ mm, one can compute the probability to have a pileup vertex at a certain distance δz from the main event vertex as a function of the luminosity scenario. For $\delta z = 1$ mm, corresponding to the worst possible resolution, this probability is 5 % (23 %) for a luminosity of 2×10^{33} cm^{-2} s^{-1} (10^{34} cm^{-2} s^{-1}). This does not take into account the proper track number and direction distribution inside pileup events and should only be taken as a rough estimate. One sees that the effect is not expected to be important at low luminosities, while it could affect the results at higher luminosities.

An usual way to test the exclusivity of an event is to measure the pseudo-rapidity η_{max} of the most forward detected object (track or calorimeter hit) excluding the expected final states. For exclusive events, the measured value is expected to be important, reflecting the fact that there are no objects close to the outgoing hadron. In case of hadron-

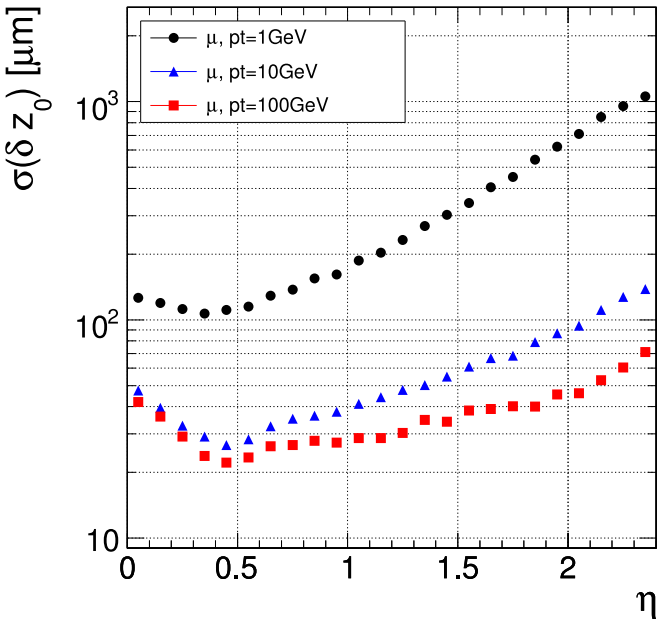

Figure 3.3: Longitudinal impact parameter resolution for single tracks in the CMS detector [111].

hadron colliders, one can choose the maximum of the computed η_{max} for both sides. If used in combination with another mean of determination of the side of the colourless exchange, like forward detectors, one may only require exclusivity on that side of the detector.

3.1.3 Background source : diffractive processes

Diffractive processes play an important role in the study of photon-induced processes because of some similarities between the two classes of interactions. These similarities will cause diffraction processes to appear as important background processes to photon-induced physics.

The name "diffraction" was given to a set of processes taking places in hadron collisions because the distribution of outgoing particles is very similar to the one observed in classic optics. The so-called *Regge theory* [83] describing these processes was built before the appearance of Quantum Chromodynamics to describe soft interactions of hadrons. In this theory, interactions are described by sums of particle exchanges, the sum being called a *Regge trajectory*. If this trajectory is colourless, it is called a *Pomeron*. In modern views based on QCD, diffractive processes are seen as the exchange of two soft gluons with strong interactions between them. As diffractive processes may happen trough colourless exchanges, they can give birth to topologies including LRGs and to exclusive final states. These processes are thus a source of irreducible (by the means of rapidity gap or exclusivity selections) background in photoproduction studies.

In order to estimate the cross-section of diffractive processes at a hadron collider, one needs diffractive parton distribution functions (DPDFs) in the same way PDFs are needed to predict hard partonic interactions cross-sections. These functions have been measured at HERA by the ZEUS and H1 collaborations [84, 85]. However, as stated before, the knowledge of DPDFs is not sufficient to predict the cross-section of diffractive processes because of the high probability of multiple interactions. This leads to important uncertainties when trying to estimate these cross-sections at the LHC.

3.2 Forward detectors at the LHC

Ever since the potential of forward physics was revealed, central detectors were complemented by many kinds of *forward detectors* and *very*

forward detectors. We will call "forward" detectors aiming at detecting particles emitted with a pseudo-rapidity exceeding ~ 2.5. Very forward detectors are usually placed several meters further, but the main difference lies in the fact that they use the beamline optics as a spectrometer to distinguish between beam particles and particles of interest (beam particles with energy loss and any kind of non-beam particles).

At HERA, both the ZEUS and H1 detectors were complemented by very forward detectors aiming at detecting the protons and electrons that have lost energy. At the Tevatron, D0 and CDF also used forward detectors to study soft and hard diffraction and for monitoring beam losses. It is thus only natural that the LHC experiments have a forward physics program based on forward and very forward detectors.

3.2.1 Forward detectors and forward physics at the LHC

Both ATLAS and CMS have a vast forward physics program, including luminosity measurements, soft diffraction, hard diffraction, photon physics and some more exotic studies. Many detectors were designed for that purpose, some of them ready for the start of the LHC while some other detectors will be installed in the years to come.

Forward detectors around CMS

CMS forward calorimeters Although most of the CMS detector only extends to $|\eta| \lesssim 2.5$, the hadronic calorimeter extends to $|\eta| = 5$. While this calorimeter does not aim at precision measurements, this extra coverage is very useful for rapidity gap selection such as the one described in section 4.3.3.

TOTEM The TOTEM [89] independent experiment is based on a series of detectors placed inside and outside of the CMS volume. Its initial purpose was to measure the total proton-proton cross-section with a high precision, but it offers many opportunities for diffraction and photon physics studies. It consists of four main subparts: a tracking device placed in front of the forward hadronic calorimeter and a second one fixed to the beam pipe 14 m away from the interaction point, covering the region $5.3 < |\eta| < 6.7$. The other parts are typical so-called "roman pots" station placed at 150 m and 220 m from the IP. These roman pots consist of moveable silicon detectors that can approach the beam to nearly

1 mm, efficiently detecting protons with non-nominal energy with a transverse position resolution of 10 μm.

Castor This sampling calorimeter [90] is located downstream the second totem station at 14 m. Castor has a very similar η acceptance as TOTEM. It contains both an electromagnetic and hadronic calorimeter parts. Its initial physics program is to study the hadronic activity in the forward region, in order to study low-x and diffractive physics.

ZDC As the beams run in two different pipes, their paths have to be separated by strong dipoles. Neutral particles (mainly neutrons and photons) can thus be detected by this device [88] placed between the two beam paths at 140 m from the IP, downstream the separating magnets, as they are not deflected.

FP420 In order to measure processes in which one proton undergoes a very low energy loss (less than 1%), a common project [91] between CMS and ATLAS was set up to place detector stations at 420 m on both sides of both experiments. The motivation of the project is exclusive Higgs production which can lead to two surviving protons which are usually out of the TOTEM detectors acceptance, thus requiring new detectors sensitive to smaller energy losses. The detectors stations consist of pipe sections able to move transversely to bring the tracking detectors to a few millimetres to the beam. The transverse position reconstruction resolution is expected to reach 15 μm. It is complemented by timing Cerenkov detectors aiming at measuring the longitudinal position of the vertex of the central process.

Forward detectors around ATLAS

LUCID These detectors [87] take place at 17 m from IP1, the centre of the ATLAS detector. They cover the rapidity range $5.6 < \eta < 6$ and rely on Cerenkov techniques to count incoming particles.

ZDC The same type of detectors as the CMS ZDC will also take place at ATLAS.

ALFA This setup [88] has the same purpose as TOTEM: a total pp cross-section measurement. The detectors consist of roman pots containing scintillating fibres placed at 237 m from the IP.

FP420 The detector setup will be the same as at CMS.

3.2.2 The LHC beamline

In order to understand and simulate correctly the path of protons towards the very forward detectors, the beam parameters and the different apparatus acting on it must be fully characterised. The position and lateral size of the LHC beams are mainly controlled by two types of elements:

- focusing (quadrupoles) or deflecting (dipoles, kickers) magnets;
- collimators and optical apertures, limiting the lateral beam extension.

Quadrupole magnets can focus the beam either vertically or horizontally. Dipole magnets also come in two kinds: rectangular dipoles (R-BEND) with a straight shape, and sector dipoles (S-BEND) which are bent to match the beam curved trajectory. The former are mainly used in the long and short straight sections (LSS, SSS) of the beamline, while the latter are placed in the dispersion suppressors (DSs) and the bending sections (ARCs) [94]. The kickers are magnets that control the crossing angle of the beams at the IP.

Basics of beam optics

Many parameters are used to describe the state of a particle beam in general or at a given position. Here we will give a short description of the most commonly used set of parameters. For a complete derivation of the equations of motion of particles in a beamline, see appendix A.

Beta functions: in presence of quadrupoles which have the strongest effect on the beam transverse distribution, the motion of the particles is described by the equation: $x''(s) = k(s)x(s)$ where x'' is the second derivative of the transverse position x with respect to the longitudinal position s of the particle along the beam path. This equation describes an oscillation and can be written as:

$$x(s) \propto \sqrt{\beta(s)}\cos(\Psi(s) + \phi), \tag{3.3}$$

where two functions are introduced: the $\beta(s)$ function which describes the evolution of the beam transverse size, and $\Psi(s)$ which represents the phase advance of the oscillation and is defined by:

$$\Psi(s) = \int_{\sigma=0}^{s} \frac{d\sigma}{\beta(\sigma)}. \tag{3.4}$$

The proportionality factor and the phase constant ϕ are fixed by the initial conditions. Two β functions are needed to describe the beam size evolution, corresponding to the horizontal and vertical directions.

Emittance: from equation 3.3 one could see that the solutions for x, x' form an ellipse of fixed surface F along the movement. The *emittance* associated with a particular particle is defined as $\varepsilon = F/\pi$. The fact that it is constant is a direct consequence of Liouville's theorem of canonical equations of movement. The square root of the emittance also gives the missing proportionality factor of equation 3.3. The envelope E of the trajectories of single particles after any number of runs around the storage ring, or of particles with same emittance ε is thus given by $E(s) = \sqrt{\varepsilon\beta(s)}$.

This allows to define the envelope of the whole beam as a beam property. Assuming a Gaussian distribution of the transverse position of particles in the beam, one can define the size of the beam as one standard deviation from the central position. The corresponding emittance is computed as:

$$E(s) = \sigma(s) = \sqrt{\varepsilon_\sigma \beta(s)} \Rightarrow \varepsilon_\sigma = \frac{\sigma^2(s)}{\beta(s)} = cst. \tag{3.5}$$

This is generally used to define the beam emittance. It allows, providing $\beta(s)$ is known, to compute the beam size at one standard deviation for any position s. Again, a vertical and an horizontal emittance have to be defined.

Size and divergence: as stated before, a beam may be described by a Gaussian distribution in transverse position and angle with respect to the beam direction. One can thus give the initial conditions in terms of four standard deviation values $\sigma_{(x,y)}$ and $\sigma_{\theta_{(x,y)}}$ for a given reference position (usually the interaction point).

Dispersion: all previously defined quantities are used to define beam particles with the nominal beam energy or small variations from it. The case of small energy losses is generally treated through the *dispersion* function $D(s)$. The position of a particle with a momentum difference Δp is given by:

$$x(s) = x_0(s) + D(s)\frac{\Delta p}{p} \tag{3.6}$$

Where x_0 is the position of this particle assuming no energy loss. The dispersion function is only approximately independent of the energy loss, and this relation thus only holds for small values of $\Delta p/p$.

Parameters of the LHC beams

Here are the parameters describing the nominal 7 TeV proton beams of the LHC:

- the horizontal and vertical emittances $\epsilon_{x,y} \sim 500 \times 10^{-6}$ μm
- the lateral beam size at the IP $\sigma = 16.6$ μm $= \sqrt{\epsilon\beta^*}$, where $\beta^* = 0.55$m is the value of the beta function at the IP
- the lateral vertex size (or the transverse size of collision region) $\sigma^v = 11.76$ μm $= \sigma/\sqrt{2}$
- the angular divergence at the IP $\sigma_\theta = 30.2$ μrad $= \sqrt{\epsilon/\beta^*}$
- the crossing angle is equal to 2×142.5 μrad, in vertical (horizontal) plane at the IP1 (IP5)
- the energy spread $\sigma_E = 1.129 \times 10^{-4}E$

The beamline around interaction region 5 (IR5) corresponding to the CMS detector is described below. The elements affecting the beam are described starting at interaction point 5 (IP5), going eastward when looking from the centre of the ring. The other side of the beamline is very similar. As the region of interest for the forward physics related detectors extends up to approximately 500 m from the IP, the beamline is described only up to that point. The layout of the beam is shown on Fig. 3.4.

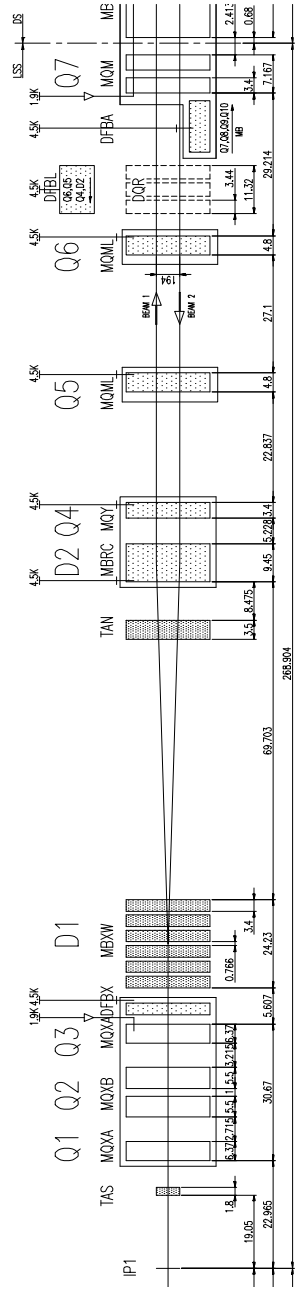

Figure 3.4: Layout of the LHC beam line around IP1 and IP5. See text for a complete description.

Upstream 85 m from IP

Downstream the IP, beam 1 separates from the incoming beam 2 because of the crossing angle. The two beam paths stay close ($\sim$ 4 mm) for the first 85 m. They encounter the first three collimators at 19 m, 45 m and 55 m from the IP (the so-called low-β inner triplet). A first kicker takes place at 30 m from the IP and then quadrupoles[2] (H: 23 and 47 m ; V: 32 and 39 m) and consecutive dipoles (RBEND) from 60 to 81 m, which deviate the two beam paths to lead them to their final separation of 194 mm. The dipoles are positioned symmetrically with respect to the two beams.

From 85 m to 269 m from IP

At about 160 m from the IP big RBEND dipoles are used to make the beam orbits parallel, so from there on the beams get to their nominal relative positions. These dipoles are positioned in such a way that the beam 1 (2) enters (exits) it perpendicularly. Four more collimators are located respectively at 141, 149, 184 and 256 m from the IP5. Two kickers, at 165 and 199 m, lead them to the ideal path that they would have followed if there were no crossing angle. The beam is kept under control by five additional quadrupoles (H: 194, 260, 264 ; V: 168 and 226 m) and one dipole (153 m). This is the end of the straight section.

From 269 m onwards

At 269 m the beam path starts its bending. The beamline is composed of quadrupoles to keep the beam focused in alternance with sector dipoles to bend it. The first sextupoles with non-zero field are situated after 439 m downstream from the IP.

3.2.3 Very forward detectors at 220 m and 420 m

As introduced before, the purpose of very forward detectors is to tag interactions including a proton scattered at very low angle while having suffered a substantial energy loss. This targets especially diffractive processes and photoproduction, for which a surviving proton can escape in the beam pipe with an energy loss of the order of a few percents.

[2] In the following, "H" and "V" will stand for horizontally and vertically focusing quadrupoles respectively.

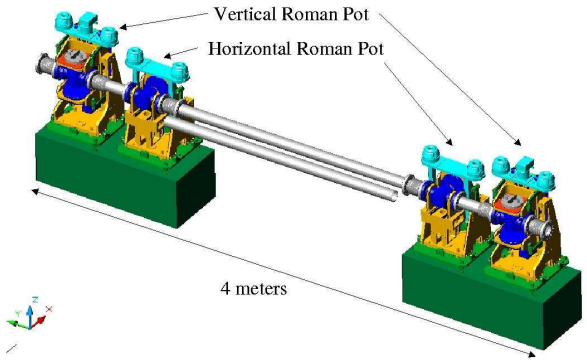

Figure 3.5: The *roman pot* design of TOTEM very forward detectors

Both ATLAS and CMS will most likely be complemented by four VFD stations each, placed in the free spaces of the beamline around 220 m and 420 m.

220 m from CMS: TOTEM

The TOTEM very forward detectors are typical *roman pots*: the detectors are placed in the primary vacuum, directly inside the beam pipe. The part entering the tube has a thinner part which forms the entrance window behind which the actual detector is located as can be seen on Fig. 3.5. It consists of 10 layers of silicon strips detectors in each "pot". During injection phases where the beam is less focussed and could damage the detectors, the pots can retract from the pipe. The closest approach distance of the detectors is fixed by security at 1.3 mm from the beam, approximately 5 times the size[3] of the beam at that place. This setup is the only one ready for measurements.

The choice of the position at 220 m is motivated by the fact that it is a minimum of the horizontal beta function and that the phase advance with respect to the IP is very close to π. The first property implies that the beam is thin, which reduces the uncertainty on the displacement induced by the proton energy loss. A phase advance of π ensures that the ratio x/β is the same as at the interaction point. The position of a proton at 220 m is consequently only weakly affected by the angle at the

[3]The size of the beam is defined as twice the RMS of the transverse distribution of the particles.

interaction point, and is thus less dependent on the momentum transfer of the interaction as will be explained in section 3.2.5.

420 m from both experiments: FP420

Contrarily to TOTEM detectors design, FP420 stations consist of moving parts of the beam pipe, according to the so-called *Hamburg pipe* design. One of the main motivations for this design is the lack of room: protons which lost energy tend to get between the two pipes, leaving only little space for detectors and preventing a design similar as TOTEM's.

The stations consist of sets of detectors containing silicon 3D detectors which will approach the beam to ~ 4 mm complemented by timing Cerenkov detectors. The timing measurement aims at a precise measurement of the vertex longitudinal position of the event vertex. Indeed, if the event contains two escaping protons and that these two are detected, the difference of time Δt between the two detectors directly gives the longitudinal distance between the main vertex and the geometrical centre of the central detector. In order to achieve a good precision in that measurement, the overall detector is expected to reach a timing accuracy of 10 ps, giving a vertex position measurement of ~ 2 mm. The conditions at 420 m are not as favourable than at 220 m in terms of phase advance and beta functions. On the other hand, the dispersion is far higher, providing good acceptance at low energy losses and good energy reconstruction resolution. The installation of the setup is foreseen to happen in 2010.

3.2.4 Acceptances

The acceptance of forward detectors is defined as a function of two variables: the energy loss E_{loss} of the proton and the momentum transfer t of the interaction. The effect of an energy loss is to displace the particle transversely of an amount given (for $x \ll 1$) by $\Delta x = D(s)\Delta E/E$ with D being the dispersion of the beam at that position s, while the momentum transfer causes the particle to exit the vertex with some angle with respect to the beam direction.

The energy acceptance of forward detectors is driven by two factors: the lower bound is basically related to the distance of closest approach d of the detector to the beam: $\Delta E_{min} \sim dE/D(s)$. The upper bound depends on the beamline aperture limitating elements.

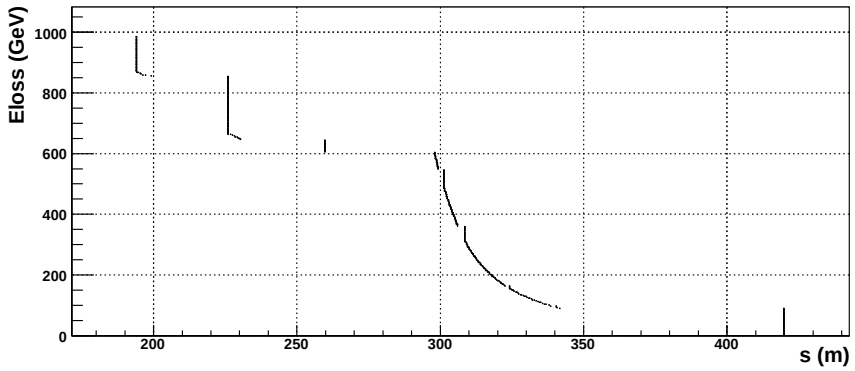

Figure 3.6: Position s reached by a particle with given energy loss E_{loss}. The particle is supposed to be at the centre of the beam with no angle at the interaction point. Forward detectors were considered at 420 m from IP only.

At the LHC the dipoles are essentially bending the beams horizontally: in the long bending sections obviously, and around the interaction points to get them to the interaction point from their running position where they are separated by 20 cm and back afterwards. This means that there is no dispersion in the vertical plane. Consequently, the detectors should approach the beam from the sides, between the two beam pipes for VFDs at 420 m and externally for the stations around 220 m.

In order to estimate the acceptance in a realistic way, the HECTOR [95] simulation software described in appendix A was written. It checks the position of particles at the entrance and exit of each element of the beam line in order to determine the position a particle reaches as a function of its energy, position and angle at the interaction point. This position is shown as a function of the energy loss on Fig. 3.6.

The results of these simulations for both beams are shown on Fig. 3.7 and 3.8. Beam 1 is defined as going counterclockwise while looking at the ring from above. One sees that at low momentum transfer (t) the acceptance only depends on the energy, while at higher t the distributions get wider because of the angle induced by the particle exchange and the acceptance begins to lower. For elastic photoproduction processes, the momentum transfer is low (~ 0.1 GeV^2) and it is thus safe to assume a purely energy-dependent acceptance window.

Applying these acceptances to the luminosity plots shown in section

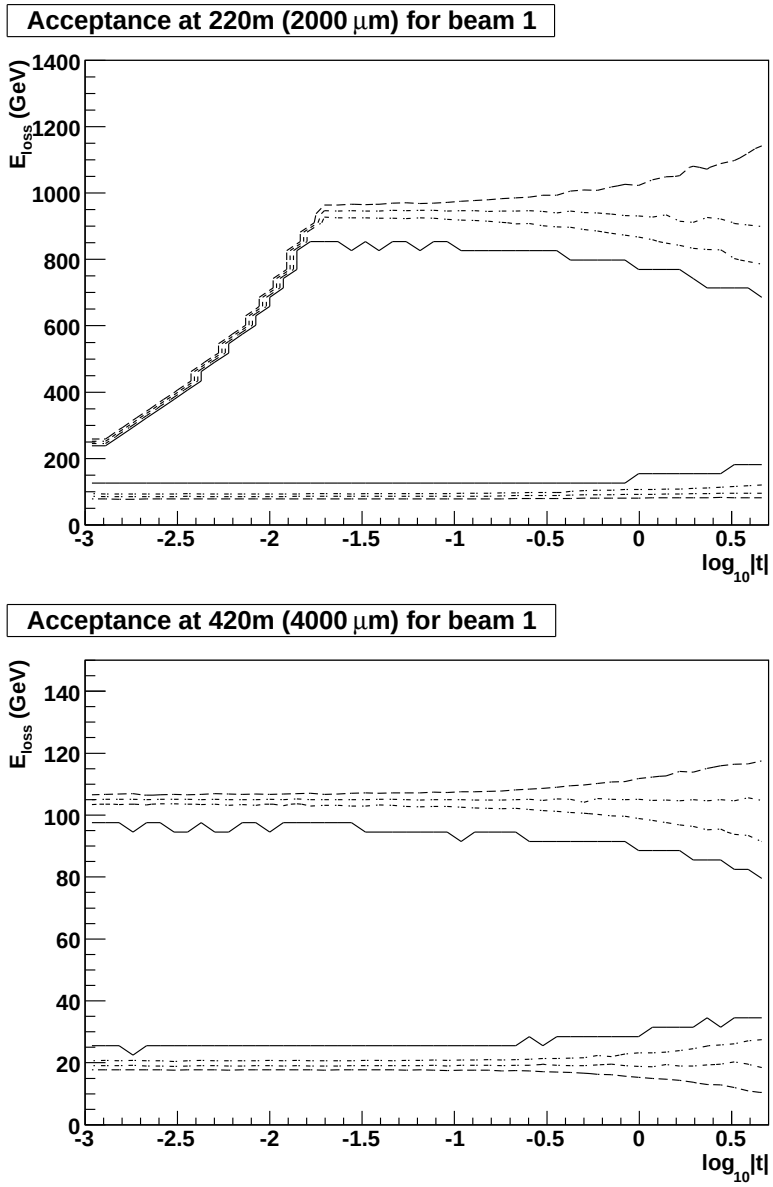

Figure 3.7: Acceptance of very forward detectors at 220 m (top) and 420 m (bottom) from the IP for beam 1. The plain lines represent 100 % acceptance, while dashed lines give the 75 %, 50 % and 25 % limits. The detectors at 220 m and 420 m have been assumed to approach the beam at 2 mm and 4 mm respectively.

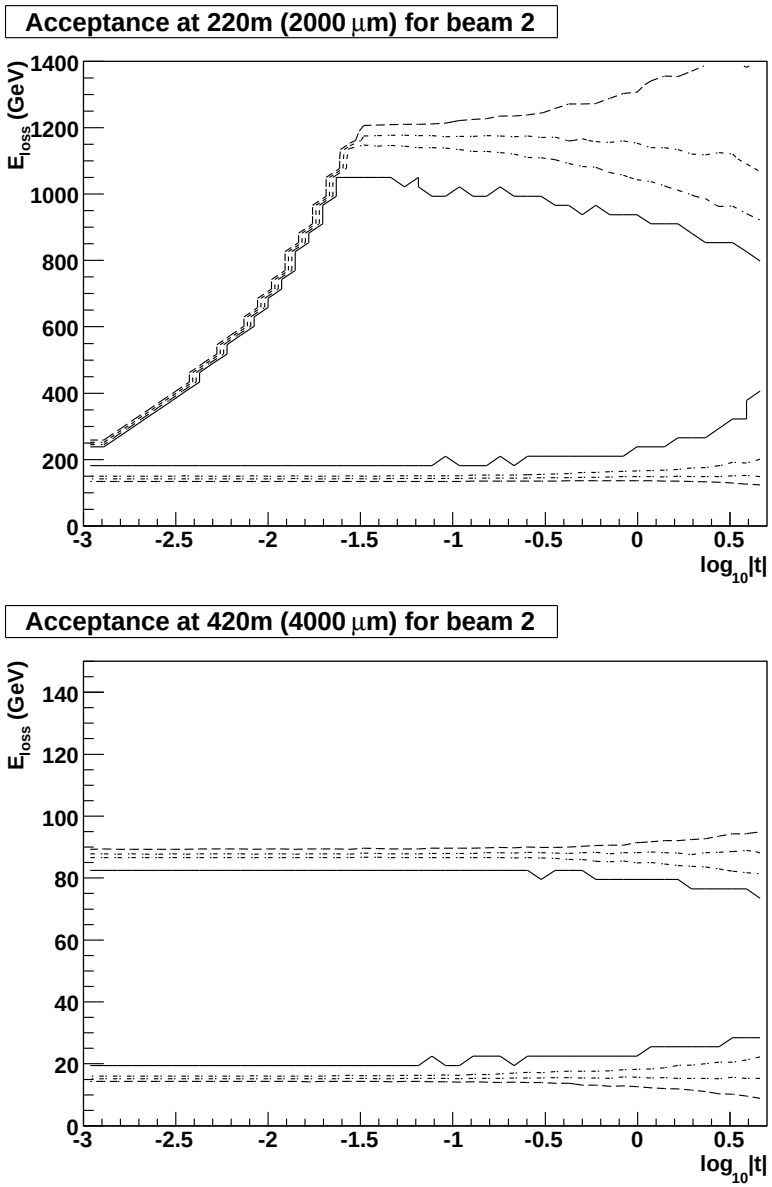

Figure 3.8: Acceptance of very forward detectors at 220 m (top) and 420 m (bottom) from the IP for beam 2. The plain lines represent 100 % acceptance, while dashed lines give the 75 %, 50 % and 25 % limits. The detectors at 220 m and 420 m have been assumed to approach the beam at 2 mm and 4 mm respectively.

1.3.5 allows to know the effective luminosity available while using very forward detectors to tag photoproduction processes. The corresponding plots are shown on Fig. 3.9 and 3.10.

3.2.5 IP variables reconstruction and resolution

As stated in section 3.2.3, one of the advantages of VFDs is that they can allow the reconstruction of part of the initial state or even the full initial state of the event in case of double-tagged $\gamma\gamma$ or γ-pomeron interactions. This requires to extract information on the emitted particle from the position of the hit of the emitting proton in the forward detector.

The initial state of the proton at the IP consists of five variables: transverse position (x^*, y^*), angle with respect to the nominal propagation direction (θ_x^*, θ_y^*) and the proton energy. Among these variables, $\theta_{x,y}^*$ and the energy are especially interesting to reconstruct the proton state, as they are directly related to its 4-vector.

In the absence of magnets of higher orders than quadrupoles, the horizontal (x) and vertical (y) propagations are completely decoupled and thus the x position of the particle at the VFD is only dependent on x^*, θ_x^* and the energy. Obviously, a single position measurement leads to an infinity of solutions for this set of variables, and a second position measurement by another detector plane is needed to restrict the available phase space by measuring the angle of the proton with respect to the beam.

One could object that a third plane could be used in order to get a unique solution. Technically however, the planes are part of a single detector placed in a magnetic field-free zone, which implies that the position of the third plane could directly be deduced from the positions in the two others and thus bring no additional information.

Principles of initial state reconstruction

As the dipoles bend the beam horizontally (except for kickers around the ATLAS interaction point), the horizontal position of the proton hit in a VFD is mostly driven by the beam dispersion D, with the simple approximate relation :

$$x = D_{VFD} E \tag{3.7}$$

and E can easily be reconstructed as the ratio x/D. This is done assuming that the contribution of the IP position and angle of the par-

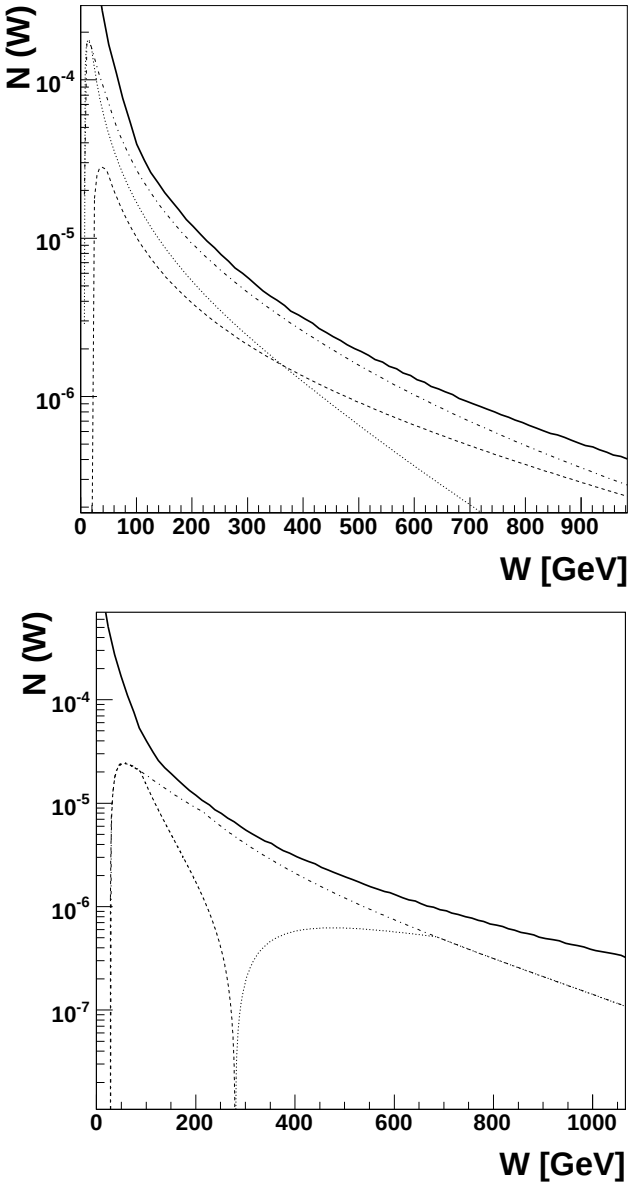

Figure 3.9: Effective luminosity of photon-photon interactions with the requirement of one (up) or two (down) tagged protons using detectors at 220 m (dashed), 420 m (dotted) or both stations (dash-dotted). One should note that in the case of single tag, luminosities have to be multiplied by two in order to take into account the symmetry between the two beams. The solid line shows the untagged luminosity.

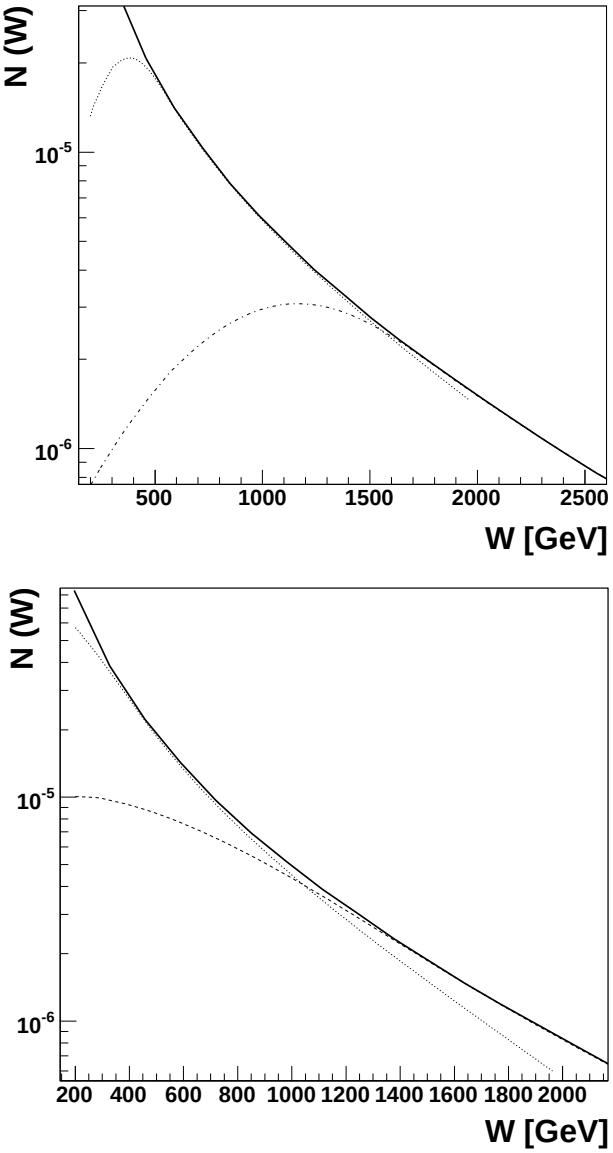

Figure 3.10: Effective luminosity of photon-proton interactions in gamma-quark (up) and gamma-gluon (down) channels using detectors at 220 m (dashed), 420 m (dotted). On the gamma-quark luminosity plot, the luminosity including one tag at 220 is indistinguishable from the untagged lumi after 1500 GeV while the luminosity for a 420 m tag dies around 2 TeV of centre of mass energy. Only the interactions with the up quark were considered for illustration. The solid line shows the untagged luminosity.

ticle contribute in a negligible way to the VFD particle position. This is not generally true. Especially, pomeron exchanges usually imply high momentum transfers and accordingly high IP angles, which has a direct effect on the VFD hit position, as shown on[4] Fig. 3.11.

It is thus mandatory to use the information from a second detector plane in order to compensate for the effect of momentum transfer. Using the linear equations for the particle propagation described in appendix A, one gets:

$$\begin{aligned} x_1 &= \alpha_1 x^* + \beta_1 \theta_x^* + D_1 E \\ x_2 &= \alpha_2 x^* + \beta_2 \theta_x^* + D_2 E \end{aligned} \tag{3.8}$$

where the indices specify the detector planes. There are three unknown quantities for the particle IP state, while the α, β and D factors can be computed using the matrix formalism used in the HECTOR software. One quantity should then be neglected in order to solve these equation, for which the most natural choice is the position x^*. This variable is not related to the physics process and neglecting it keeps the door open to the reconstruction of the angle θ_x^*. One then gets the so called *angle compensating method* for energy reconstruction:

$$E = \frac{\beta_2 x_1 - \beta_1 x_2}{\beta_2 D_1 - \beta_1 D_2}. \tag{3.9}$$

This allows to completely remove the momentum transfer dependence of the reconstructed energy. The same method allows to reconstruct $\theta_{x,y}$ by isolating it from equation 3.8 and thus to compute the particle momentum transfer.

Coping with chromaticity

Unfortunately, when the energy loss gets higher than a few percent, one has to take chromaticity (see appendix A) into account. The α, β and D factors of equation 3.8 become strongly energy-dependent and the equations 3.7 and 3.9 do not apply anymore. There is in general no analytic way to solve these because of the nontrivial behaviour of the parameters and one should then resort to other methods like tables of pre-calibrated values or iterative methods.

[4]For small angle scattering, the momentum transfer can be linked in a very good approximation to the scattering angle by the relation: $t \simeq P_T^2 \simeq E^2(\theta_x^{*2} + \theta_y^{*2})$.

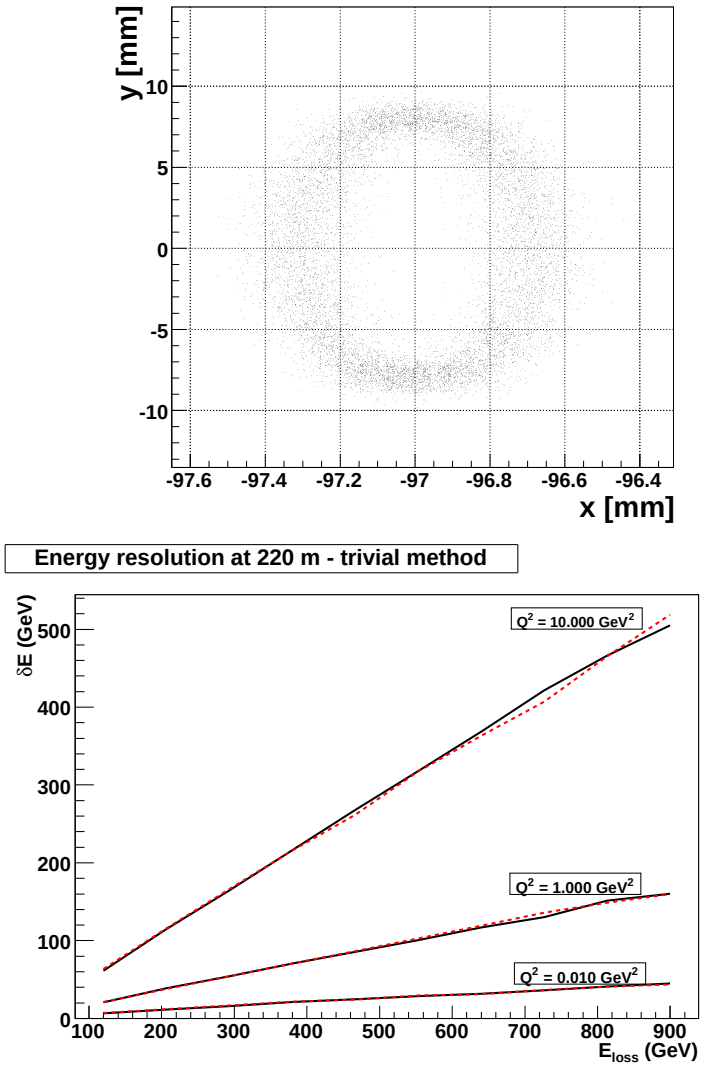

Figure 3.11: Effect of momentum transfer of 10 GeV^2 on the beam profile (left). As the position is measured only using one detector plane, this affects strongly the reconstructed energy resolution (right).

This nonlinear effect is easily seen on *chromaticity grids* such as shown in Fig. 3.12. These show the hit position on both detector planes as a function on the energy loss and angle at the interaction point. Some regions are favoured and get better reconstruction resolution because the iso-energy lines are further appart, while in other regions the reconstruction becomes more difficult and the resolution worsens. Another remarkable property is the effect of the phase advance close to π at 220 m which ensures an angle between the iso-energies and the iso-angles close to $\pi/2$, while at 420 m the grid is more closed on itself.

The simple method of equation 3.7 can easily be adapted to consider chromaticity. As the dispersion D becomes a function of the energy, one has:

$$x = D_{VFD}(E)E = \bar{D}_{VFD}(E)$$

which can be inverted. The behaviour of the $\bar{D}_{VFD}$ function is obtained from simulation or from a physics process.

This can be used for the study of photoproduction processes like lepton pair production, but does not give acceptable results in most physics processes for which the momentum transfer is most likely to be non-negligible like diffractive processes. The general case requires to adapt the two-plane based method. Many solution are possible, depending on the requirements in terms of speed and adaptability.

The most trivial solution is to compute the chromaticity grids from simulation with an important number of lines and to use it to build lookup tables. This method, once the simulations have been done, can be quick but requires many fits to achieve good precision at high energy where the effect of chromaticity becomes very important. It also requires to rebuild the lookup tables for any change in the calibration or in the beamline magnets. This last aspect of the method was considered unacceptable and other methods have been investigated to get a fully automatic solution, while keeping a very fast event-based reconstruction, maximum precision and no bias.

Iterative method

A first possible approach is to get the energy using an iterative algorithm. Such a solution would allow to avoid fitting and simulations and would thus be completely adaptative. On the other hand, it requires repeating computations a certain number of times, which leads to an event-based

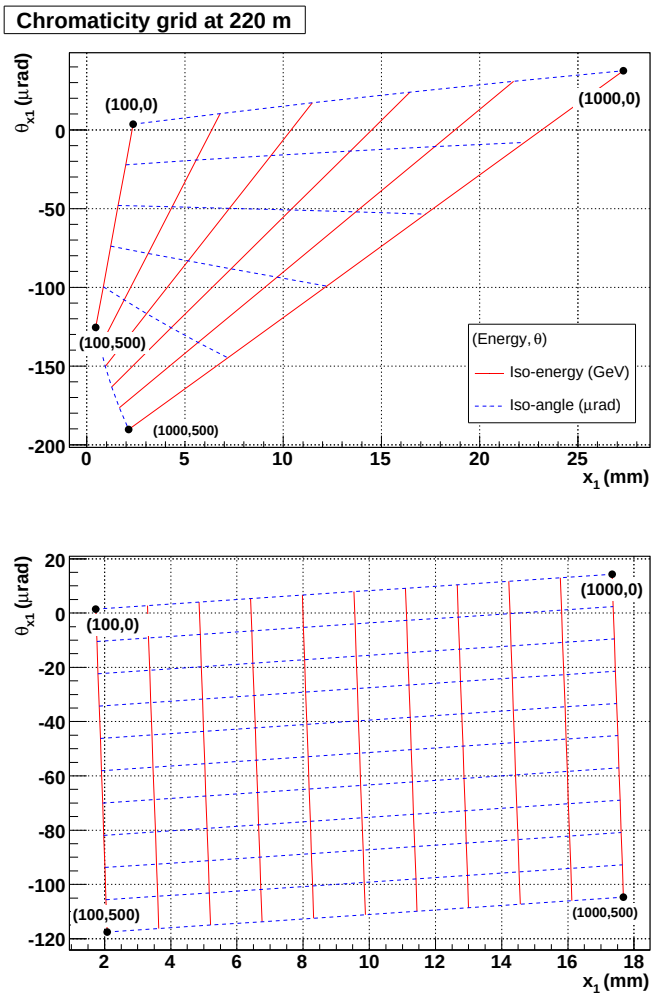

Figure 3.12: Chromaticity grids for detectors at 220 m from CMS interaction point. Lines represent protons with same energy loss (plain) and angle (dashed). The lower plot was built without taking into account the second-order effect of the energy loss, while the top plot includes it.

potential increase in the computation time if the convergence is not fast enough. As the factors of equation 3.8 are energy-dependent, equation 3.9 becomes :

$$E = \frac{\beta_2(E)x_1 - \beta_1(E)x_2}{\beta_2(E)D_1 - \beta_1(E)D_2} = F(x_1, x_2, E), \tag{3.10}$$

which is generally solved iteratively using:

$$E_{i+1} = F(x_1, x_2, E_i),$$

where E_i can converge or not to the solution of equation 3.10 depending on the behaviour of the function F around the solution E. In the particular case of the LHC, reconstruction for detectors at 420 m from the IP gives nice, unbiased results after only less than 10 iterations, while detectors at 220 m show pathologic behaviours giving birth to important bias in the reconstructed energy, leading to the rejection of the method.

Likelihood method

The solutions of equations 3.8 form a curve in the tridimensionnal space (x^*, θ_x^*, E). A likelihood function can be computed for each point of this curve according to prior probabilities based on our partial knowledge of the initial state.

In the practical case treated here, the transverse position of the particles in the beam can be expected to be normally distributed around the beam centre with a known width σ_x. The distributions in θ^* and E are driven by physics and are process-dependent. However, a coherent prior would be to use the EPA distributions for those variables.

The likelihood for a fixed point in the tridimensional space mentioned above is the defined by:

$$L(x^*, \theta_x^*, E) = P(x^*) \times P(\theta_x^*, E) \tag{3.11}$$

Where $P(\theta_x^*, E)$ is taken to be proportional to the EPA spectrum. One usually uses the logarithm of the likelihood L, to get the following and the normal distribution of x yields:

$$\mathcal{L}(x^*, \theta_x^*, E) = \frac{x^{*2}}{\sigma_x^2} + \log\left(\frac{dN_\gamma}{dQ^2 dx}\right) + \text{constant factors.} \tag{3.12}$$

In order to solve the system 3.8 for the energy, one has to express the likelihood as a function of E only and then to maximise it. The variables x^* and θ_x^* are written as functions of the energy for a given (x_1, x_2) measurement by inverting equations 3.8, including the energy-dependence of the factors, getting $x^*(x_1, x_2, E)$ and $\theta_x^*(x_1, x_2, E)$. Only few preliminary simulations are needed, as only the dependences of $\alpha_{1,2}(E)$, $\beta_{1,2}(E)$ and $D_{1,2}(E)$ have to be computed, leading to a maximum of 6 functions to be fitted.

Once the $\mathcal{L}(x_1, x_2, E)$ function has been determined, maximising it straightforwardly gives the most probable energy assuming the measurement at VFDs and the prior knowledge of the initial state.

In the case of the LHC, further simplifications can be applied, making this method faster and simpler. First, the beam conditions are such that the EPA-based part of the likelihood will be strongly dominated by the position distribution at the IP, and can thus be considered as a constant factor in the calculations. The likelihood is then:

$$\mathcal{L}(x^*, \theta_x^*, E) = x^{*2} + \text{constant factors.} \tag{3.13}$$

and it suffices to minimise x^{*2} for which the behaviour is given by:

$$\begin{aligned} x^*(x_1, x_2, E) &= \frac{1}{\beta_2\alpha_1 - \beta_1\alpha_2}\left[\beta_2 x_1 - \beta_1 x_2 - (\beta_2 D_1 - \beta_1 D_2)E\right] \\ &= F_1(E)x_1 + F_2(E)x_2 + F_3(E). \end{aligned} \tag{3.14}$$

One sees that only three functions $F_i(E)$ must be estimated in order to get a complete description of the chromaticity grid. The same could be applied to the vertical component of the propagation in order to complement the reconstruction. However, as no strong vertical dipoles influence the proton path vertically, its vertical position is less dependent from its energy and the gain is negligible[5].

Resolution

Using the likelihood method, the resolution of the reconstructed proton energy can be computed. For a particle with given energy E, the error on

[5]This was checked for the case of CMS. In the case of ATLAS, as strong vertical "kicker" dipoles are present in the beamline, it is likely that the vertical position of the protons is more influenced by the energy loss and could then perhaps be used for energy reconstruction.

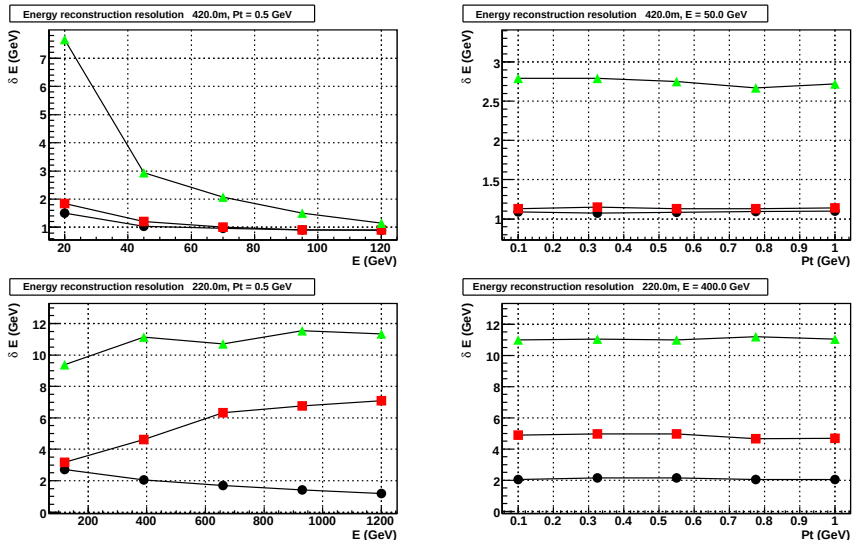

Figure 3.13: Resolution of the reconstructed energy loss of protons as a function of the energy loss (left) and the transverses momentum (right), for stations at 420 m (up) and 220 m (down). The detector resolution was supposed to be perfect (no smearing, circles), 5 μm (squares) and 30 μm (triangles).

the reconstructed energy comes from the uncertainties on the initial state (position and angular distributions) and the resolution of the position measurement of the very forward detector. Using two detectors weakens the effect of the angular distribution, but the effect of the beam size is impossible to reduce. Fig. 3.13 shows the expected reconstruction resolution using two detector planes, for the station at 220 m and 420 m. One sees that the effect of the angle of the particle at the interaction point, here given in terms of transverse momentum, is compensated by the method and does not affect the energy resolution anymore, while the detector resolution becomes a dominant factor in the resolution.

One can also reconstruct the angle or the transverse momentum of the proton at the interaction point using similar methods. Although it may be used in diffractive physics, in the case of photoproduction the expected momentum transfer is generally below 1 GeV^2 which is of the order of the resolution and this measurements would not be reliable. Fig. 3.14 shows the reconstructed momentum transfer resolution.

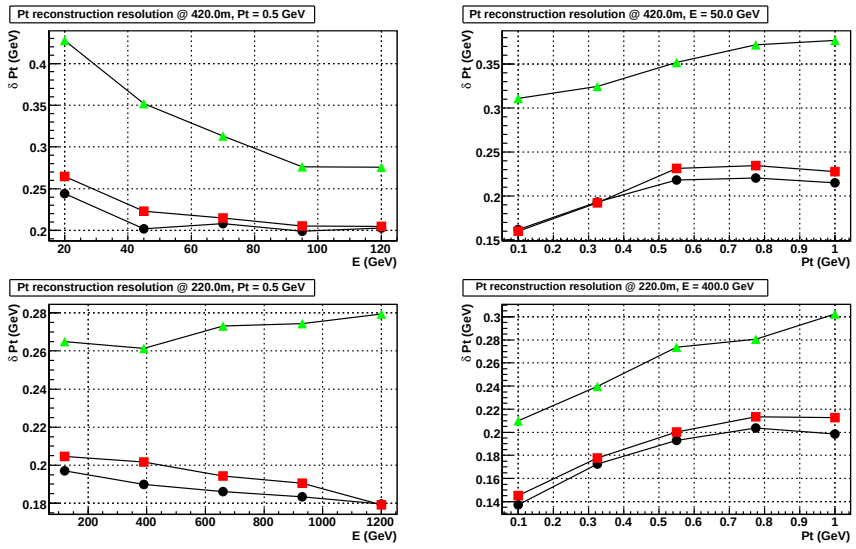

Figure 3.14: Resolution of the reconstructed transverse momentum of protons as a function of the energy loss (left) and the transverses momentum (right), for stations at 220 m (up) and 420 m (down). The detector resolution was supposed perfect (no smearing, circles), 5 μm (squares) and 30 μm (triangles).

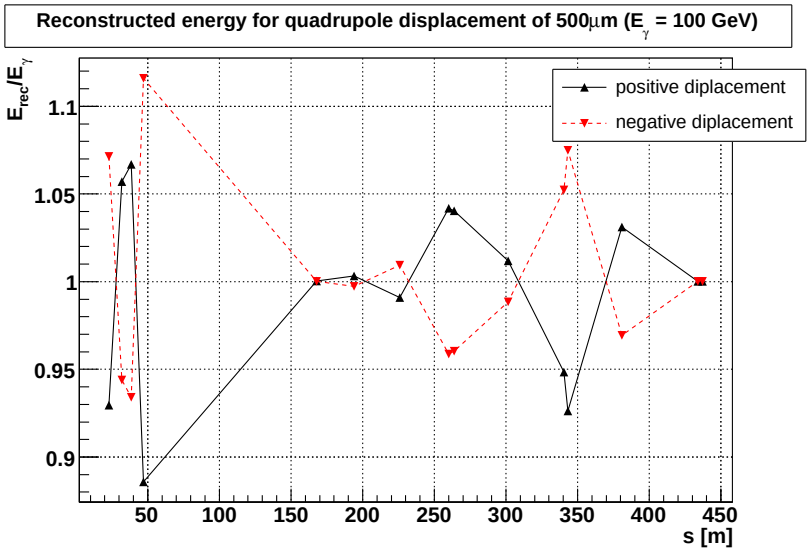

Figure 3.15: Effect on the reconstructed (using detectors at 420 m) proton energy loss of a 0.5 mm transverse displacement of the quadrupole placed at s.

3.2.6 Misalignment and calibration

An important issue when dealing with very forward detectors is the calibration of the position measurement. The position of the proton at the VFD station is indeed strongly affected by any change in the transverse position of the beamline quadrupoles. As this position measurement is the key ingredient in energy reconstruction, any bias would have important consequences in any study based on the energy loss measurement. Using HECTOR, the effect of a half-millimetre transverse displacement on the reconstructed energy loss has been computed and is shown on Fig. 3.15. For such a small displacement, the effect already reach 10 % for the quadrupoles close to the IP, while it is slightly less important for other magnets.

One way to deal with this effect would be to have beam position monitors placed in the VFD stations. One would thus measure the displacement of protons relatively to the measured beam position instead of their absolute position. As shown in Fig. 3.16, it is quite efficient to compensate for the misalignement of quadrupoles far from the IP, but it does not correct for errors due to the first quadrupoles. A physics-based

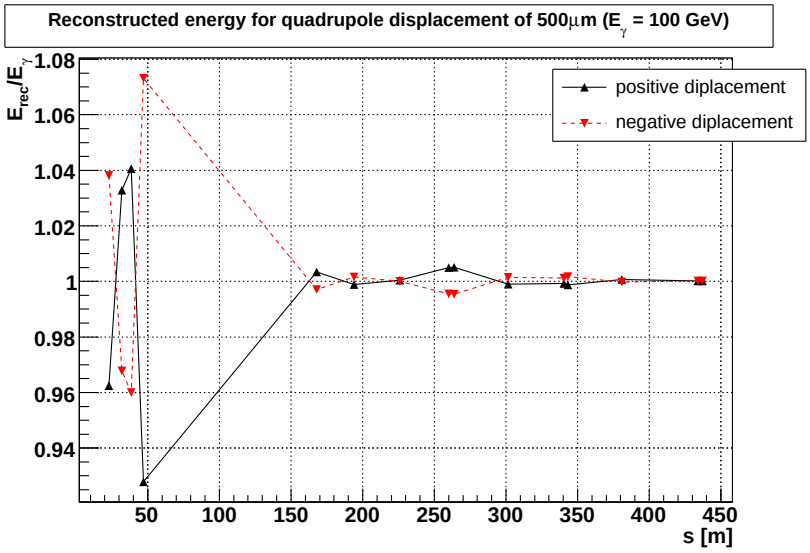

Figure 3.16: Effect on the reconstructed (using detectors at 420 m) proton energy loss of a 0.5 mm transverse displacement of the quadrupole placed at s, while considering the beam position at the VFD to be known perfectly.

calibration scheme is thus needed.

An interesting candidate for calibration is the two-photon production of lepton pairs. This process has an important cross-section of around 1 nb and the energy of a tagged forward proton can easily be reconstructed from the measurement of the invariant mass and total longitudinal momentum P_Z of the two-muons system:

$$\begin{aligned} 4E_\gamma E_{\gamma'} &= M^2_{\mu\mu} \\ E_\gamma - E_{\gamma'} &= P_Z \end{aligned} \tag{3.15}$$

The energy of both photons is exressed as:

$$E_{(\gamma,\gamma')} = \frac{1}{2}\left(\sqrt{P_Z^2 + M^2_{\mu\mu}} \pm P_Z\right). \tag{3.16}$$

The resolution on the photon energy computed using this method was estimated [89] to be of the order of 10^{-2} GeV. Using this very precise measurement, one can obtain a good calibration function between the measured position of the proton in the VFD and the energy loss, providing that enough statistics can be obtained. The LPAIR simulation software was used to estimate the ratio of dimuon events for which the two muons would be measured in the central detector while having one proton detected in the VFDs. The obtained visible cross-section is around 3 pb for tagging at 420 m and 0.05 pb at 220 m. As some tens of events are sufficient, the calibration of detectors at 420 m from the IP is thus possible using very short periods of data taking, while the 220 m detectors cannot be recalibrated as often, and require other means of calibration. An illustration of the above discussion is given by Fig. 3.17 in which MADGRAPH [92] was used to simulate Higgs boson production in the photon-photon production channel and the mass of the particle was reconstructed using the measurement of both surviving protons. The effect of the misalignment of a quadrupole is clear. It is only partially compensated by the usage of beam position monitors. The calibration using 100 dimuon events allows an unbiased mass reconstruction.

Another related issue is the relative alignment of the different parts of the detector stations. While physics processes give information about the distance between the beam and the detectors, *internal alignement* can only be achieved by the means of precise beam position monitors mounted close to each detector. The full procedure for the internal alignment of FP420 stations can be found in [91].

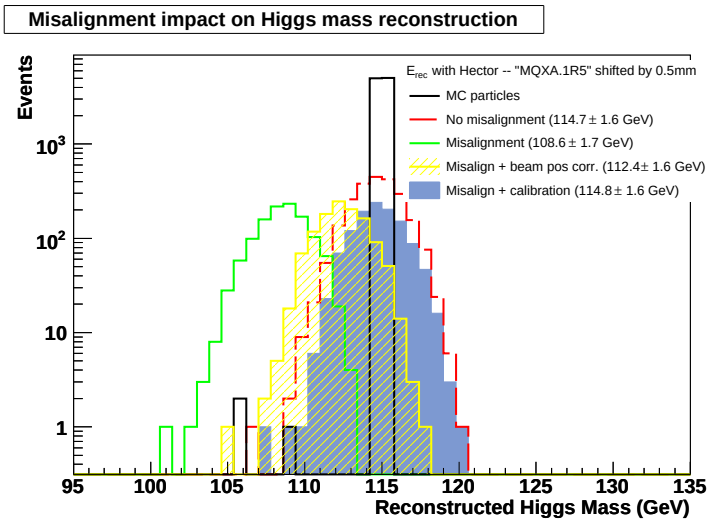

Figure 3.17: Reconstruction of a centrally produced higgs boson via photon-photon interaction using the missing mass method. The empty histogram shows the effect of the misalignment of a quadrupole close to the IP. The shaded histogram is obtained using perfect beam position knowledge. The filled histogram represents the effect of a calibration based on $\sim$ 100 dimuon events.

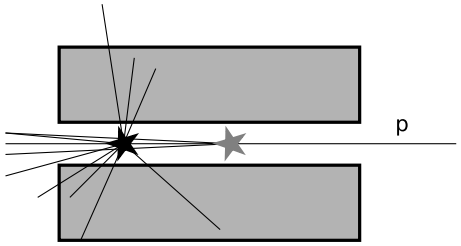

Figure 3.18: Illustration of accidental coincidences between a soft diffractive event (grey) including a surviving proton which can be detected by VFDs and a hard event mimicking the signal (black).

3.2.7 Background sources: soft diffraction and machine-induced hits

As was shown in the previous sections, very forward detectors form an excellent tool for studying processes with forward protons.

Focusing on photoproduction, the most obvious backgrounds for the study of a particular process come from other photoproduction processes with similar final states. Along with these, using VFDs brings other sources of background: first, some hard diffractive processes may have the same topology as the signal process and an escaping forward proton, but more generally, any hit in a VFD leads to the tagging of the current event as a photoproduction/hard diffractive one. The main source of forward protons with non-standard energy at the LHC will come from single diffractive events of the type $pp \to pX$. Given the high luminosity of the LHC, the probability of such an event to take place at the same time as a partonic event with similar topology as the signal is high, and the complete event, partonic + soft diffractive, will then be interpreted as a photoproduction event with the right topology, as illustrated by Fig. 3.18.

Soft diffraction and accidental coincidences

The soft single diffraction cross-section was estimated using PYTHIA [93] to be:

$$\sigma_{pp\to pX} = 14 \text{ mb}$$

In the following, three different configurations will be assumed, namely two detectors at 220 m each side of the central detector, two detectors

Detectors scenario	220 m only	420 m only	220 m + 420 m
Tagging efficiency	15 %	13 %	28 %

Table 3.1: single diffractive tagging efficiency for different detector scenarios.The detector at 220 m(420 m) is placed at 2 mm(4 mm) from the beam position. Beam 1 and beam 2 values have been averaged.

at 420 m each side of the central detector and the combination of the four detectors. The tagging efficiency of single diffractive events using forward detectors has been computed using HECTOR and can be seen in table 3.1.

Computing the probability of a single-diffractive event to induce a tag in the forward detector requires some combinatorics. It depends strongly on the luminosity scenario, namely the bunch-crossing (BC) rate f and the instantaneous luminosity. The average number λ of single diffractive events per BC is given by:

$$\lambda = \frac{\mathcal{L}\sigma}{f}. \tag{3.17}$$

As the actual number of events for a single bunch-crossing is the result of a Poisson distribution of parameter λ, the probability $P_\lambda(X = n)$ to have n single diffractive interaction during one single BC is:

$$P_\lambda(X = n) = e^{-\lambda}\frac{\lambda^n}{n!} \tag{3.18}$$

We are here interested only in events for which at least one single diffractive interaction is tagged in the forward detectors. This probability can be written as:

$$P(Y \geq 1) = 1 - P(Y = 0) \tag{3.19}$$

where Y is the number of protons simultaneously tagged. The computation of $P(Y = 0)$ can easily be done the following way:

$$P(Y = 0) = \sum_{n=0}^{\infty} P(Y = 0 \mid X = n)P_\lambda(X = n) \tag{3.20}$$

The probability $P(Y = 0 \mid X = n)$ to have no hits in forward detectors given n single diffractive events is given by:

$$P(Y = 0 \mid X = n) = (1 - p)^n, \tag{3.21}$$

where p is the probability for a diffractive event to induce a hit in the VFD. The complete expression for $P(Y = 0)$ is:

$$P(Y = 0) = \sum_{n=0}^{\infty} e^{-\lambda} \frac{\lambda^n (1-p)^n}{n!} = e^{-\lambda p} \sum_{n=0}^{\infty} P_{\lambda(1-p)}(n) \tag{3.22}$$

from the definition of the Poisson distribution. The sum is equal to unity, yielding:

$$P(Y \geq 1) = 1 - e^{-\lambda p} \tag{3.23}$$

Another possible tagging strategy, especially if detected protons have to be used for the event reconstruction, is to require to have exactly one proton in the forward detector. In this case, the probability is:

$$P(Y = 1) = \lambda p \; e^{-\lambda p}. \tag{3.24}$$

This requirement simultaneously cuts a part of the signal (photon or pomeron induced) events, especially at high luminosity. However, if one wants to use the tagged forward proton in order to improve the reconstruction of the central state, it is thus mandatory to ensure that only one proton is associated with the current event and one should thus ensure that only one proton is seen in the VFDs. The effect of this requirement on the signal over background ratio is shown on figure 3.19.

This applies to both sides of the IP and the probability to get a proton tag in at least one of the forward detectors (left or right) is then, using the probability P:

$$P_{2sided} = 2P - P^2. \tag{3.25}$$

One eventually defines the *reduction factor* (R) of some detector configuration in some luminosity scenario as:

$$R = \frac{1}{P_{2sided}}.$$

This number divides the cross-section of a proton-proton process to get the visible cross-section requiring that (at least) one proton is tagged in the forward detectors. As it depends only on the single diffractive

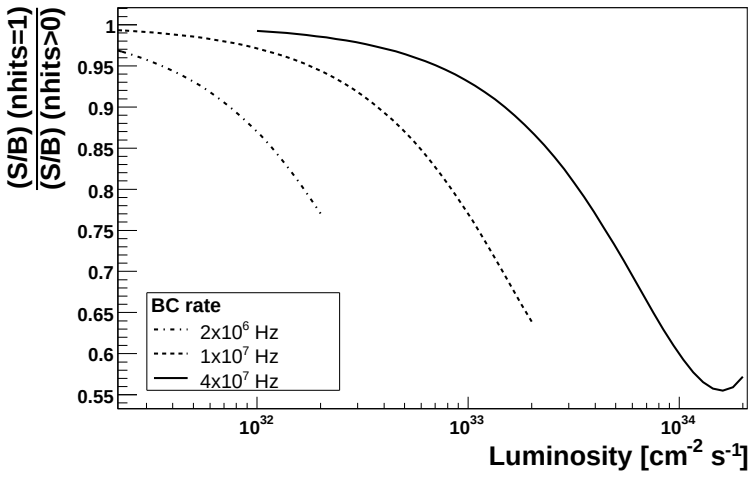

Figure 3.19: Effect of the requirement to have exactly one proton hit in the forward detectors on the signal over background ratio. A value of one means that this requirement does not affect the ratio. Values below one represent a degradation of the ratio.

cross-section it is process-independent. Fig. 3.20 shows this reduction factor in the scenario for which at least one proton is required to get a tag. Typical benchmark points are summarised in table 3.2.7. Those numbers show that tagging will most likely not reduce enough the contamination from proton-proton background processes. Fortunately, one can use the reconstructed information from the tagged proton in correlation with the central detector measurements in order to achieve further reduction as will be shown in the next section.

The detector scenario can be chosen freely according to the studied physics channel, in order to optimise the signal over background ratio.

One should note that because of this reduction factor, the number of events observed from partonic backgrounds rises roughly quadratically with the instantaneous luminosity. The main effect is that one does not gain by increasing the instantaneous luminosity. Indeed, if the significance of a measurement is given by the usual estimator $S/\sqrt{B}$ where S is the number of expected signal events after selection and B is the expected background level, S and B can be written in the case of pure partonic background as:

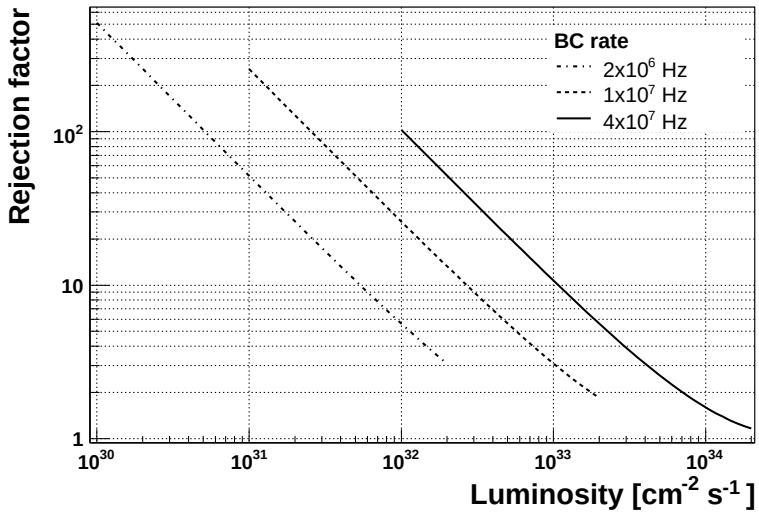

Figure 3.20: Expected reduction factor as a function of the luminosity for two bunch crossing rate scenarios (10 MHz and 40 MHz), for a scenario including detectors at 220 m and 420 m.

Luminosity scenario	BC rate	λ
10^{32} cm^{-2} s^{-1}	10 MHz	0.07
2×10^{33} cm^{-2} s^{-1}	10 MHz	1.40
2×10^{33} cm^{-2} s^{-1}	40 MHz	0.35
10^{34} cm^{-2} s^{-1}	40 MHz	1.75

Table 3.2: Average single diffractive pileup λ for different luminosity scenarios.

Luminosity scenario		220 m	420 m	220 m $\oplus$ 420 m
10^{32} cm^{-2} s^{-1}	10 MHz	55.4	48.1	26.0
2×10^{33} cm^{-2} s^{-1}	10 MHz	3.3	2.9	1.8
2×10^{33} cm^{-2} s^{-1}	40 MHz	11.5	10.0	5.6
10^{34} cm^{-2} s^{-1}	40 MHz	2.7	2.4	1.6

Table 3.3: Expected reduction factor. Although the numbers are given for illustration, forward detectors at 420 m are not expected to be present for early LHC runs at 10^{32} cm^{-2} s^{-1}.

$$\begin{aligned} S &= \sigma_s \times \mathcal{L} \times t \\ B &= \beta \times \mathcal{L}^2 \times t, \end{aligned} \tag{3.26}$$

where σ_s is the signal visible cross-section after selection, $\mathcal{L}$ is the instantaneous luminosity and t is the time during which data is taken. The $\beta \times \mathcal{L}^2$ part parametrises the background behaviour with luminosity. The significance is thus given by:

$$\frac{S}{\sqrt{B}} = \sqrt{t}\frac{\sigma_s}{\sqrt{\beta}}, \tag{3.27}$$

which is completely independent from the instantaneous luminosity. This is only valid when the estimator effectively approaches the real significance, which is not the case when number of events are too low, typically below 20 selected events. Another limitation comes from the fact that the background is usually composed of both a partonic part and a photon-induced and diffractive one which behaves the same way as the signal with respect to instantaneous luminosity. The significance is thus given by:

$$\frac{S}{\sqrt{B}} = \sqrt{t}\frac{\sigma_s}{\sqrt{\beta + \sigma_b/\mathcal{L}}}, \tag{3.28}$$

where σ_b is the cross-section for the selected photoproduction events. The behaviour as a function of the instantaneous luminosity depends in that case of the ratio of photon-induced and partonic backgrounds.

Machine-induced background

The additional sources, not linked to central events, of hits in very forward detectors have been studied by the FP420 collaboration [96]. There are three sources of particles which could lead to hits in the very forward detectors:

1. Interactions between beam particles and residual gas in the beam pipe,

2. The beam "halo" made of protons getting far from the beam centre due to various causes,

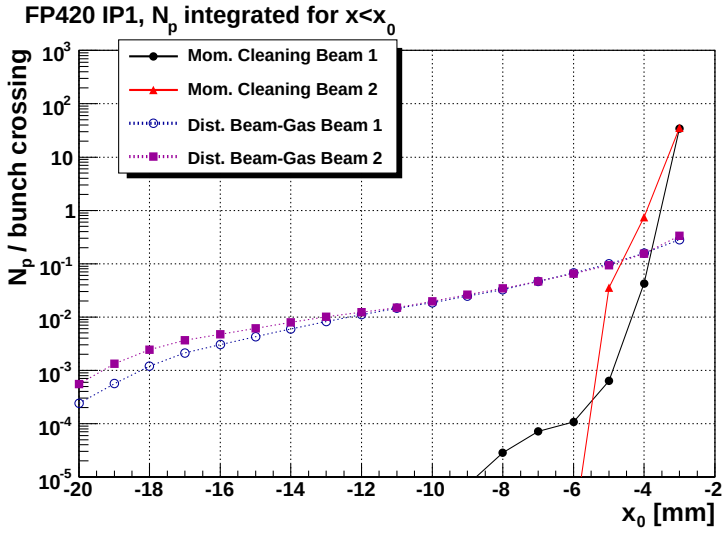

Figure 3.21: Integrated number of protons potentially hitting very forward detectors at 420 m as a function of the distance from the beam centre. The beam halo coming from the effect of collimators (Mom. Cleaning) dominates at distances lower than 5 mm but dies quickly afterwards, while the halo from distant beam gas interactions is smaller close to the beam but falls slower at larger distances.

3. Showers coming from particles produced at the IP and interacting with elements of the beam pipe like collimators.

The rate of beam-gas interactions in nominal LHC running conditions was estimated by simulation to be 2.4 s^{-1} at 240m from the IP. It has to be scaled with the pressure at 420 m which is higher, leading to a number of interactions of 1.8×10^{-4} (6×10^{-8}) interactions per bunch crossing at 420 m (220 m).

The beam halo results in an important number of protons concentrated in a region very close to the beam (Fig. 3.21). Simulations showed that detectors would have to be placed at ~ 5 mm from the beam centre in order to reduce the effect of the beam halo at the same level as the one issued from beam-gas interactions. However, it is still possible to reduce this halo by a careful positioning of collimators.

Finally, the effect of secondaries requires advanced simulations of the interaction of particles with the beam line elements and is not completed yet. Neutron rates only have been computed and are expected to be at

the level of 0.1 per bunch-crossing.

Chapter 4

Anomalous top photoproduction at the LHC

4.1 Photon interactions at the LHC

As was discussed in the previous chapters, photon-photon and photon-parton interactions will occur at the LHC at a high rate and at energies never reached in similar channels at previous colliders. The present section describes some of the possible studies of photon-induced interactions at the LHC.

4.1.1 Photon-photon interactions

Two-photon interactions are among the cleanest events one can expect to observe at the LHC. As no colour exchange is involved, the only visible particles in the detector are expected to be from the final state of the central photon-photon interaction. Additionally, owing to very forward detectors, the photon energies can be determined with excellent precision, leading to a complete knowledge of the initial state. The drawback is that cross-sections are generally low and that one thus needs large integrated luminosity.

The cross-sections for some processes computed using MG/ME [92] are shown on Fig. 4.1. Thanks to the LHC energy, the physics potential includes the production of charged particle pairs with large masses predicted by many theories beyond the Standard Model.

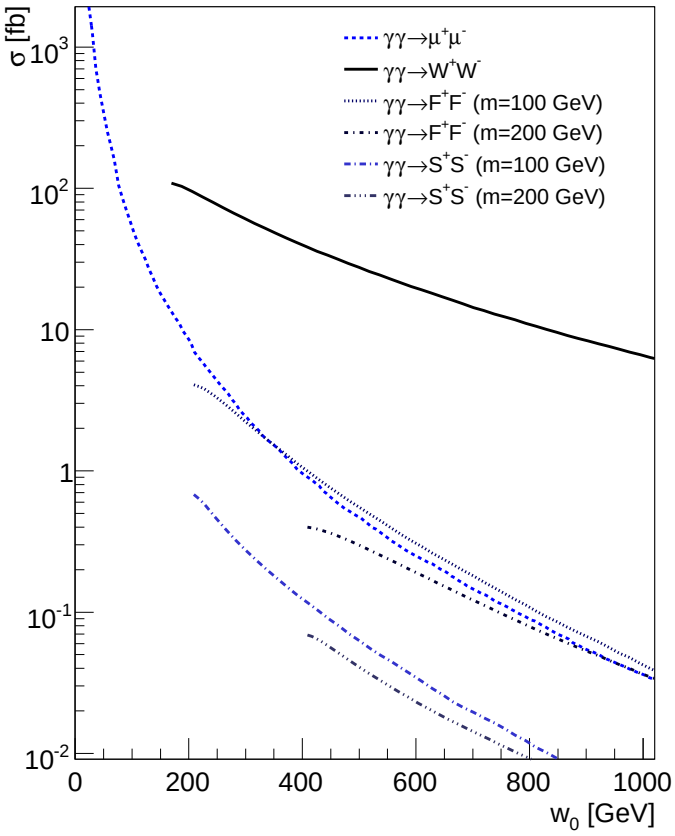

Figure 4.1: Cross-sections for various photon-photon processes as a function of the invariant mass threshold W_0. Acceptance cuts have been applied on lepton pairs [97].

Calibration and luminosity

As was introduced in the previous chapter, the two-photon production of lepton pairs can be used for the calibration of very forward detectors on a run-by-run basis. Due to their high and very well know cross-section, they also allow for precise luminosity measurements [98].

Tests of the Standard Model

The triple and quartic gauge boson couplings γWW and $\gamma\gamma WW$ are important predictions of the Standard Model. As the production rate of W boson pairs via photon-photon interactions directly depends on such couplings, a simple counting experiment could lead to improved limits on possible anomalous triple [101] and quartic couplings [42].

Supersymmetric particle pairs

Searches for supersymmetric particles are one of the main focuses at the LHC. Though the rate of photon-photon production of such particles may not be as high as the one expected from partonic interactions, they offer the possibility to have a complementary study, while benefiting from the initial state reconstruction by the VFDs which allows to put limits on the particle masses [100].

4.1.2 Photon-proton interactions

While not as clean as photon-photon interactions and not allowing a complete initial state reconstruction using VFDs, photoproduction processes at the LHC offer higher cross-sections and energies, allowing to perform early studies using only small integrated luminosities. Especially, one expects high top quark production rate and decent Higgs production cross-section. Photoproduction cross-sections for various processes are shown on Fig. 4.2.

Higgs boson search

The Higgs production was studied in the WH associated channel [99]. This process has a cross-section of around 20 fb for a SM higgs with a mass between 115 and 170 GeV while large background rates are expected from W + jets processes. It can therefore not be considered as a discovery channel for the Higgs boson, although the expected signal

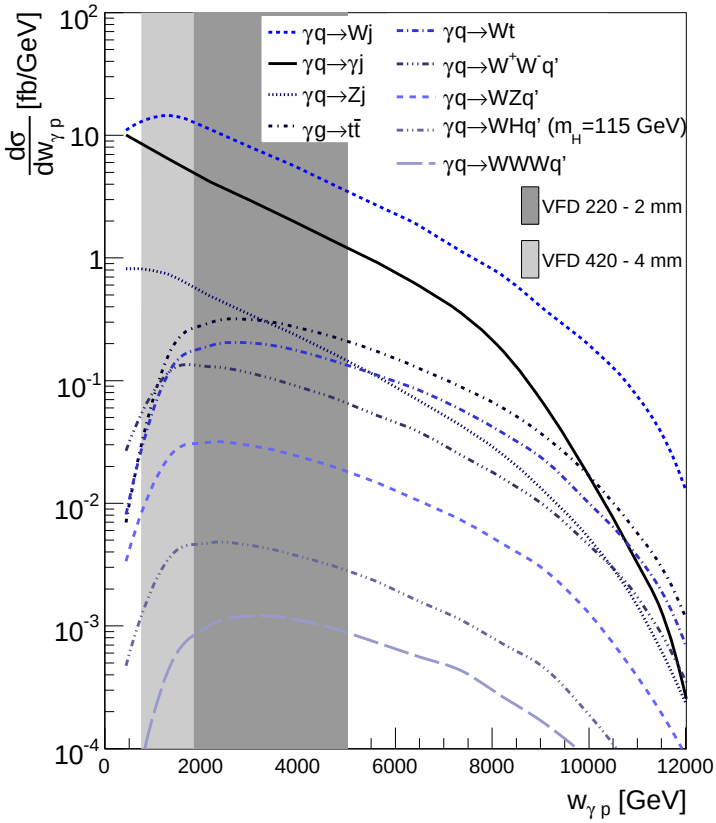

Figure 4.2: Cross-sections for various photoproduction processes as a function of the γp centre of mass energy [97].

over background ratio is close to one, but offers a complementary study to the partonic Higgs production. Moreover, its cross-section might be enhanced in the case of fermiofobic Higgs models as it is sensitive to the WWH coupling.

$|V_{tb}|$ measurement

Single top production in partonic interactions is only a small fraction ($\sim$ 5 %) of the total top quark production cross-section at the LHC. In the photoproduction channel however, associated Wt production reaches around 50 % of the total top photoproduction rate, leading to the opportunity to measure the $|V_{tb}|$ matrix element which is predicted to be far from its SM value of 1 in some models [102]. The expected precision of $\sim$ 14 % on $|V_{tb}|$ is at the same level as the values obtained in partonic interactions [103].

Vector mesons

The exclusive photoproduction of vector mesons has been studied at HERA, where production cross-section (Fig. 4.3) were measured for various particles [104, 105]. Such measurements are especially important in order to improve our kowledge of the gluon content of the proton at low values of x. The CMS collaboration has studied the Υ expected production [106] using the Starlight [107] simulation software and showed that one could expect to observe the resonances corresponding to the first three S-states of the Υ in the muon decay channel by reconstructing the invariant mass of the two muons. As the mass of the mesons are well known, this process can be used to calibrate the momentum measurement of low P_T muon tracks.

4.2 Anomalous top search at the LHC

In a similar manner to what has been done at HERA, photoproduction can be used to constraint anomalous couplings corresponding to FCNC at the LHC. The production mode is similar as at HERA, as shown on Fig. 4.4. Given the high luminosity and energy avaliable, it is natural to think that limits could be improved.

However, there is an important difference between HERA and the LHC when it comes to photoproduction, as partonic processes overwhelm photoproduction which was not the case at HERA. The back-

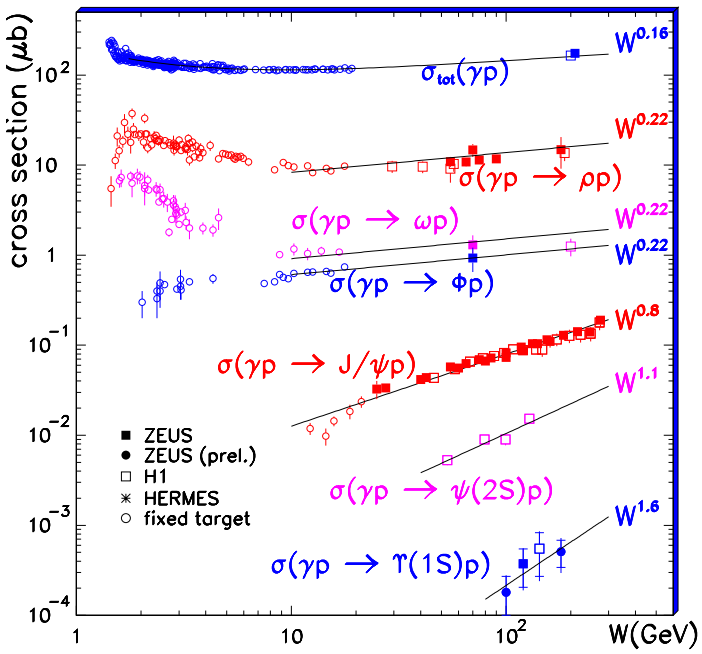

Figure 4.3: Vector mesons production cross-section as a function of the photon-proton centre of mass energy as measured at HERA by the HERMES, H1 and ZEUS collaborations.

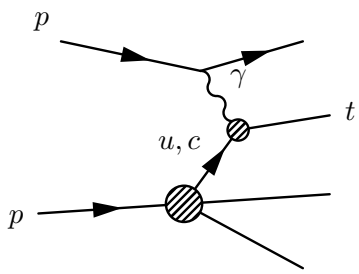

Figure 4.4: Single top production at the LHC through flavour changing neutral currents.

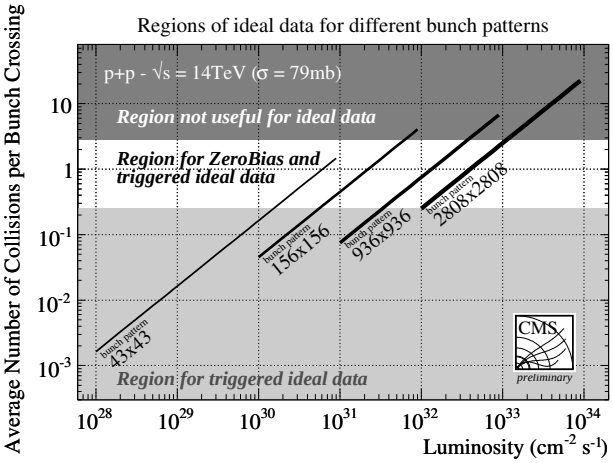

Figure 4.5: Number of events per bunch-crossing for three different running scenarii

ground conditions are thus by far harder to cope with, and efficient ways to select the few photoproduction events happening in the huge amount of partonic processes are needed.

Moreover, the LHC instantaneous luminosity will reach a point where many interactions take place during each bunch crossing. This event pileup usually adds a lot of parasitic hadronic activity, making reconstruction and selection even harder. The number of pileup events per bunch crossing according to some scenarii is shown on Fig. 4.5.

Another way to probe these anomalous couplings is to study the FCNC decay [117, 118] of the top quarks produced in pairs as was done at the Tevatron, using the large cross-section of this process (833 pb at NLO) or the associated production of a top quark and a photon [119]. The CMS and ATLAS collaborations studied the sensitivity of such methods and showed that the limit on the anomalous coupling $k_{tq\gamma}$ could be lowered to $\mathcal{O}(10^{-2})$.

4.3 Early LHC anomalous top photoproduction study

The first part of the present analysis will consider a scenario in which no event pileup takes place. This assumption relies on a luminosity of around $10^{32} - 10^{33}$ cm^{-2} s^{-1} for an integrated luminosity of 1 fb^{-1} cor-

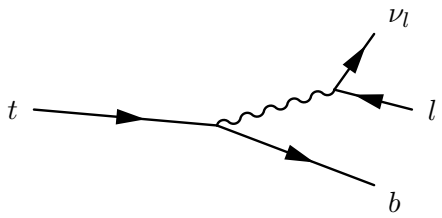

Figure 4.6: Top SM decay into a jet, a charged lepton and a neutrino

responding to the first months of running of the LHC at full energy. Only the central detector is assumed, without any additional forward detectors, as these will not be present for the first months of LHC running. Another analysis has been performed considering the presence of pileup and using very forward detectors for tagging and reconstruction purpose and will be presented in the second part of this chapter.

4.3.1 Backgrounds

The dominant background processes for the final state illustrated by Fig. 4.6 come from events with one W boson and one jet mis-tagged as a b-jet (jet from a b quark). The b-tagging method (see next section about event simulation and reconstruction) is such that jets coming from c quarks have a high probability to be tagged as b-jets (around 10 %) making it an important background, at the same level as the light jet contribution, for which the mistagging probability is only around 1 %. The contribution of backgrounds containing genuine b-jets is negligible because of its low cross-section, which is three orders of magnitude lower than the cross-section of the W + c topology. Relevant background cross-sections and sample sizes are given in table 4.1.

An additional source of background could come from the $pp \rightarrow Wb\bar{b}$ process. While its cross-section is quite low compared to other partonic backgrounds (14 pb after basic acceptance cuts), it contains genuine b-jets which lead to a high selection efficiency. It could thus amount for a maximum 10 % contribution in the partonic background. However, this already small contribution is expected to be further lowered by the requirement to have only one hard jet in the event. This process was thus neglected in the analysis.

One should note that the photoproduction backgrounds only take into account the elastic emission of the photon. Inelastic emission could obviously contribute to both signal and background as the cross-section is expected to be of the same order as the elastic cross-section. Although

process	σ [fb]	sample size
$\gamma p \to Wj$	41.6×10^3	100 k
$\gamma p \to Wc$	11.5×10^3	100 k
$pp \to Wj$	77.3×10^6	100 k
$pp \to Wc$	8.8×10^6	100 k
Diffractive W	1.3×10^6	100 k

Table 4.1: Background processes used for the analysis of the anomalous top photoproduction. Cross-sections include generation cuts of $P_T > 10$ GeV for leptons and $P_T > 20$ GeV for jets. The symbol 'j' stands for jets coming from light quarks (u, d, s) and gluons.

it would be natural to include these signal and background processes in the analysis, the technical difficulties linked to the proper simulation of the proton remnant, greatly magnified by the influence of important multiple interactions probability, make this task extremely demanding in terms of both new theoretical and computing tools to be developed. As the proper estimate of the effect of a rapidity gap condition is impossible without these results, we had to choose to limit ourselves to the elastic part.

We therefore choose here to rely on the very good forward region coverage of both CMS and ATLAS to detect the remnant of the proton after inelastic photon exchange and thus reduce both inelastic signal and background to negligible levels.

4.3.2 Event simulation

The event simulation was done at tree-level using the MadGraph software. Only direct photoproduction has been considered for both signal and background processes, as no resolved photoproduction processes contribute to the required final states. For the signal, CalcHep [108] was also used. The effective Lagrangian 1.28 was introduced in CalcHep to compute the total cross-section, which is given by:

$$\sigma_{pp\to t} = 368 \text{ pb} \times k^2_{tu\gamma} + 122 \text{ pb} \times k^2_{tc\gamma}. \tag{4.1}$$

The difference between the up and charm quark contributions being due to the difference in the two quark contents of the proton. As we want to focus only on SM-type decays of the top quark, CalcHep was used

BR($t \to W^+ b$)	$k_{tc\gamma} = 0$	$k_{tc\gamma} = 0.05$	$k_{tc\gamma} = 0.10$	$k_{tc\gamma} = 0.15$
$k_{tu\gamma} = 0$	99.84 %	99.79 %	99.65 %	99.41 %
$k_{tu\gamma} = 0.05$	99.79 %	99.74 %	99.60 %	99.36 %
$k_{tu\gamma} = 0.10$	99.65 %	99.60 %	99.46 %	99.22 %
$k_{tu\gamma} = 0.15$	99.41 %	99.36 %	99.22 %	98.98 %

Table 4.2: Branching ratio of the top quark to b quark and W boson as a function of the anomalous couplings for couplings lower than the exclusion limit.

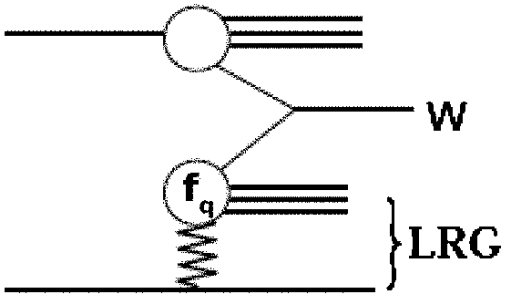

Figure 4.7: Diagram for diffractive W production at the LHC.

to compute the branching ratio of the top quark charged-current and neutral-current decays. Results can be seen in table 4.2. In the region of interest, namely $k_{tu\gamma}$, $k_{tc\gamma} < 0.1$, the FCNC branching ratios are low and will thus be neglected in further discussions.

The Pomwig[109] program (version v2.0 beta) was used to generate the diffractive W background for which the diagram is shown on Fig. 4.7. A proton survival factor of 0.05 was assumed [110] and applied as an overall correction factor to the cross-section. Hadronisation was done using Pythia 6 except for the diffractive W sample for which Herwig was used.

Detector simulation was performed using a fast simulation program designed by S.Ovyn (U.C.Louvain) and tuned to mimic a typical LHC detector. It considers perfect detector granularity and smears the energy of every visible particle(in the acceptance of the detector) with the following resolutions:

Electrons and photons: if they are in the central part of the elec-

tromagnetic calorimeter ($|\eta| < 3$), the energy resolution used is $\Delta E = 0.0026 \times E \oplus 0.028 \times \sqrt{E} \oplus 0.124$. In the forward regions ($3 \leq |\eta| < 5$), it is given by $\Delta E = 0.107 \times E \oplus 2.084 \times \sqrt{E}$.

Muons: if they are in the acceptance of the muon detector ($|\eta| < 2.4$), the transverse momentum of the muons is smeared by 1 %.

Hadrons: as for electrons, the central and forward regions are separated. Hadrons in the central region have a resolution of $\Delta E = 0.038 \times E \oplus 0.91 \times \sqrt{E}$ while in the forward region it is given by $\Delta E = 0.13 \times E \oplus 2.70 \times \sqrt{E}$.

Using particles 4-vectors, jets are reconstructed using an iterative cone midpoint algorithm [111].

Finally, in order to mimic the effect of a b-tagging algorithm such as those developed by the ATLAS and CMS collaborations, an efficiency has been associated with the proper identification of a jet coming from a b quark. The probability to identify such a jet has been set to 40 %, a typical working point of CMS and ATLAS. The corresponding mistagging probabilities (probabilities to tag a non-b jet as one) have been set to the conservative values of 10 % and 1 % for c-quarks jets and other 'light' jets respectively. The corresponding efficiencies expected by the CMS collaboration are shown on Fig. 4.8. This applies to any jet in the acceptance of the detector regardless of its direction or energy.

In order to estimate the acceptance and resolution of forward detectors, the HECTOR program was used.

4.3.3 Selection

Partonic background rejection

As shown in table 4.1, partonic backgrounds typically have cross-sections three orders of magnitude larger than the ones of photoproduction backgrounds. A particular rejection scheme is described below aiming to reduce the contribution of these backgrounds at least to the same level as the photoproduction backgrounds.

A first cut is based on the rapidity gap requirement described earlier. The variable used for that selection is the energy in a defined forward region of the detector. In the present case, we measure the total energy deposit in the regions $-5 < \eta < -3$ and $3 < \eta < 5$, corresponding to a typical coverage of forward calorimeters at the LHC. We expect very

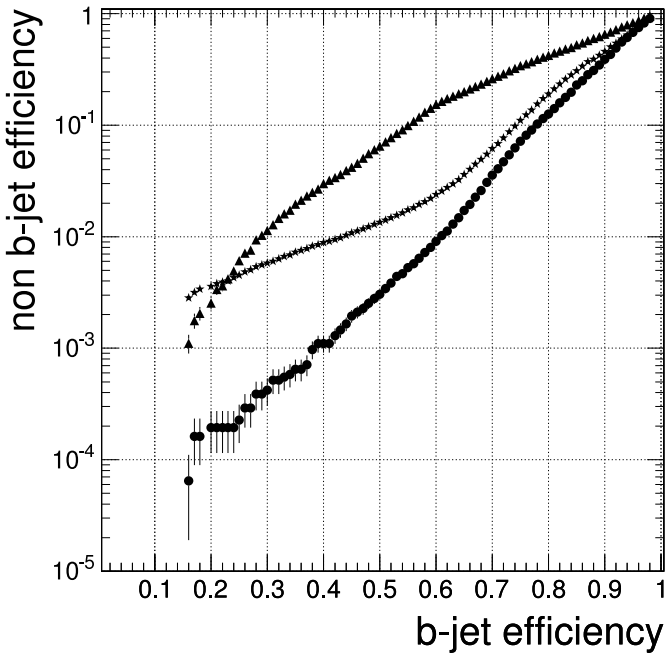

Figure 4.8: Non-b jet mistagging efficiency versus b-jet tagging efficiency for jets from charm quarks (triangles), light quarks (circles) and gluons (stars) with the CMS detector [111].

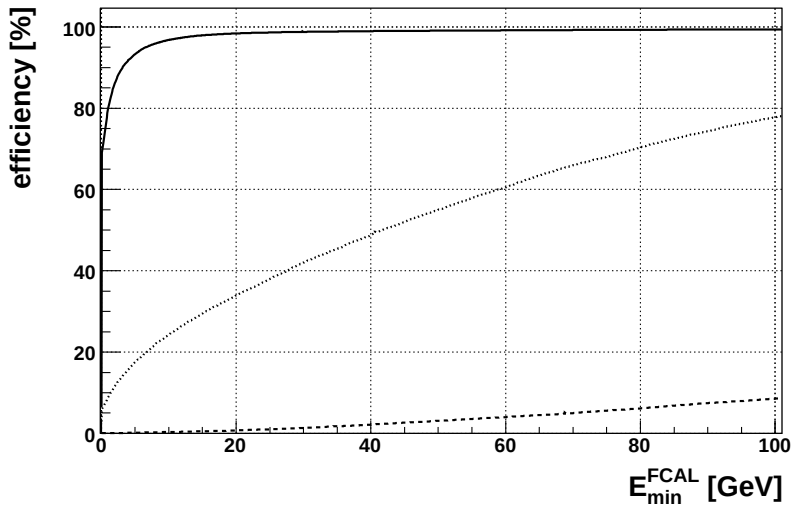

Figure 4.9: Selection efficiency as a function of the maximum allowed energy in the quietest forward calorimeter E_{min}^{FCAL} for the signal (plain), hard diffractive W production (dotted) and partonic backgrounds (dashed).

little energy deposit on the photon side for photoproduction events. The *gap energy* is thus defined as the minimum of both sides energy, noted E_{min}^{FCAL}. A typical event with a rapidity gap will then have a E_{min}^{FCAL} close to zero, while typical partonic events are most likely to show large amounts of energy in both forward regions and thus E_{min}^{FCAL} is in general large. This is illustrated by Fig. 4.9 where the efficiency of a cut of type $E_{min}^{FCAL} < E_{cut}$ for photoproduction, diffractive and partonic events is shown. One sees how partonic backgrounds are reduced while photoproduction processes are selected with high efficiency. The intermediate values for the diffractive W production is believed to be a consequence of the so-called pomeron remnant which can fill the rapidity gap. The efficiency of such a cut is heavily process-dependent. Partonic processes with many jets in the final state tend to have more colour exchanges between the objects and thus more hadronic activity, which makes the rapidity gap selection very efficient, reducing the partonic background by $\gtrsim 300$. Processes with only one jet as the ones used in the present analysis generally show a reduction of around 30 for a typical cut of $E_{min}^{FCAL} < 30$ GeV.

The exclusivity of photoproduction events is also used to reject par-

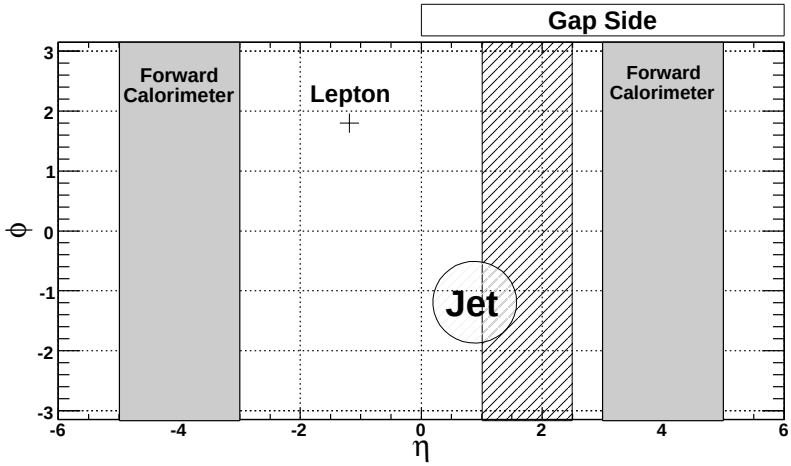

Figure 4.10: Illustration of the rapidity gap and exclusivity conditions used to reject partonic backgrounds. The forward calorimeters cover the region depicted in grey. Once the quietest side is determined and if its energy passes the cut, it is called the *gap side* and the exclusivity condition is applied on the shaded region.

tonic backgrounds. After defining the "gap side" as the side with the least forward energy, one expects no additional activity on that side, except for the central objects (in the present case, the b-jet and the lepton coming from the W decay). It is therefore required that no other tracks are seen in the central detector on that side, in the region $1 < \eta < 2.5$. Tracks associated with reconstructed final states are removed from the counting. Once again mimicking a real detector operating with a tracking device and a vertex detector, tracks were assumed visible when having a P_T of more than 0.6 GeV/c with an efficiency of 95 % [111]. This could be improved, as recent developpements by the CMS tracking group foresee a high sensitivity to tracks down to 0.3 GeV/c [112]. The overall partonic background rejection method is illustrated by Fig. 4.10.

Signal selection

The signal topology consists of one b-jet and a lepton, either electron or muon, associated with some missing transverse energy. In order to reject all "reducible" backgrounds - namely backgrounds with different topologies - one first requires one central ($-2.5 < \eta < 2.5$) isolated lep-

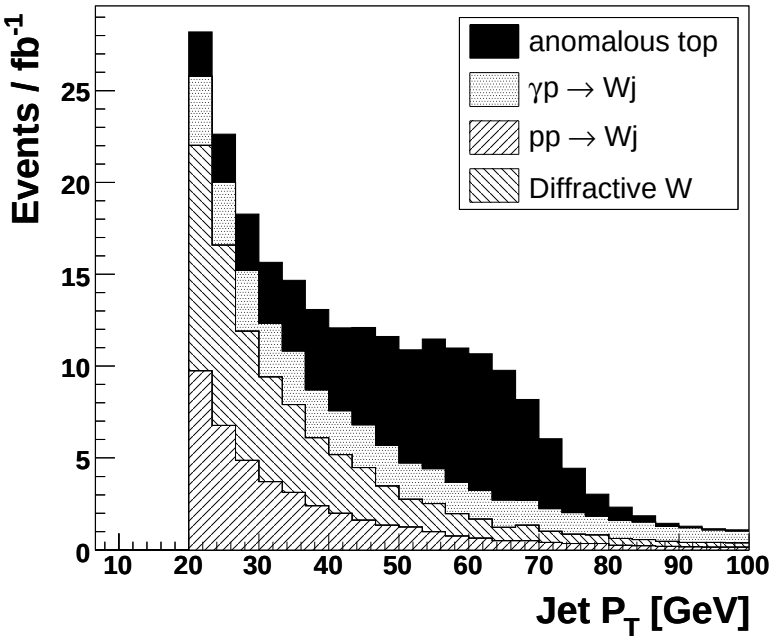

Figure 4.11: Transverse momentum cumulative distribution of the reconstructed jet, after acceptance cuts on the jet and the lepton, rapidity gap and exclusivity conditions and b-tagging. Events for which $40 < P_T < 80$GeV are selected.

ton and jet coming from the event primary vertex. Events with more than one jet with $P_T > 20$ GeV are rejected[1]. Transverse momentum cuts are placed on these objects based on the kinematics of the process. Indeed, partonic and diffractive events are t-channel processes which greatly favours low P_T jets. The transverse momentum distribution of jets is shown on Fig. 4.11. The P_T of the b-jet is naturally bounded from above at ~ 80 GeV as the P_T of the top quark is generally small. The same argument obviously applies to the lepton whose distribution appears on Fig. 4.12. The missing transverse momentum is also computed as the transverse component of the sum of the jet and the lepton four-vectors. The distribution of this variable is shown on Fig. 4.13.

The mass of the central object is compared to the top quark mass.

[1]Such "Jet veto" procedures are used in standard CMS and ATLAS analysis, see for instance [113].

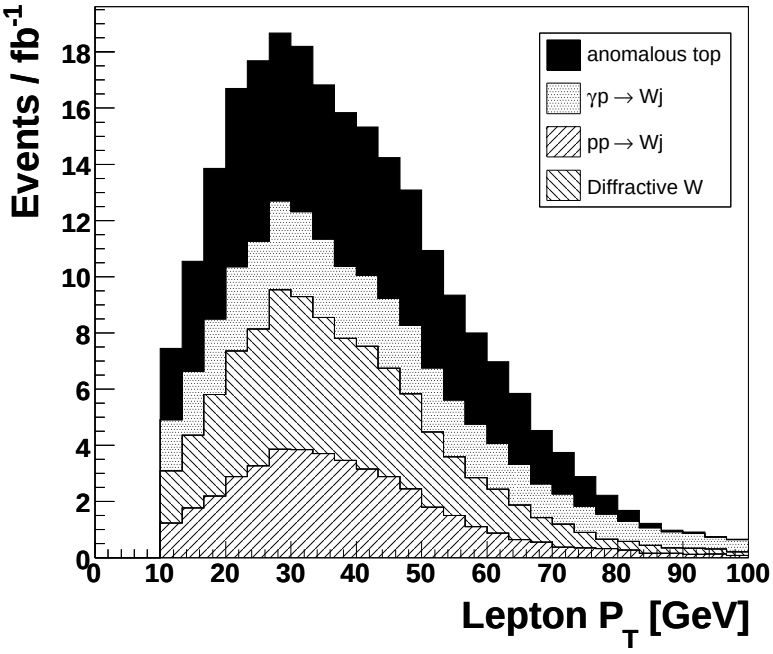

Figure 4.12: Transverse momentum cumulative distribution of the reconstructed lepton, after acceptance cuts on the jet and the lepton, rapidity gap and exclusivity conditions and b-tagging applied on the jet. Events for which $15 < P_T < 80$GeV are selected.

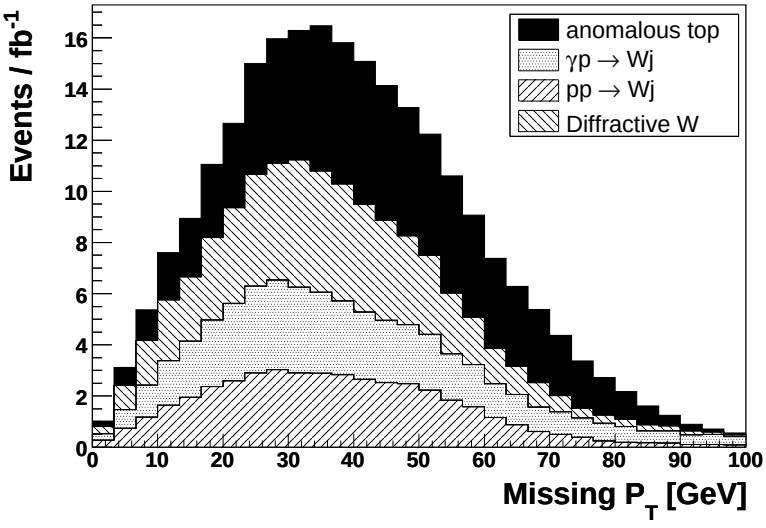

Figure 4.13: Missing transverse energy cumulative distribution after acceptance cuts on the jet and the lepton, rapidity gap and exclusivity conditions and b-tagging applied on the jet. Events with a missing transverse momentum above 15 GeV were selected

However, this requires knowing the direction of the neutrino from the W decay. One can reconstruct its azimuthal angle and its energy through the missing transverse momentum of the system, but its longitudinal momentum is unknown. It can however be reconstructed in the following way, neglecting all masses except the W one:

$$\begin{aligned} M_W^2 &= (k^\mu + l^\mu)(k_\mu + l_\mu) \\ &= k^\mu k_\mu + l^\mu l_\mu + 2k^\mu l_\mu \\ &= 2\left(k_0 l_0 - k_x l_x - k_y l_y - k_z l_z\right). \end{aligned} \tag{4.2}$$

Where k^μ and l^μ are the neutrino and lepton 4-vectors respectively. The W mass is taken as the world average. Only k_z is unknown as one gets:

$$k_0 = \sqrt{k_x^2 + k_y^2 + k_z^2}. \tag{4.3}$$

In order to shorten notation, we define:

$$\phi = \frac{M_W^2}{2} + k_x l_x + k_y l_y \tag{4.4}$$

and equation 4.2 becomes:

$$k_z^2(l_z^2 - l_0^2) + k_z(2\phi l_z) + \phi^2 - l_0^2(l_x^2 + l_y^2) = 0. \tag{4.5}$$

This second-order equation may have no solutions for k_z as a consequence of bad reconstruction of the missing energy. In this case it is choosen equal to zero. In general, two solutions for the neutrino longitudinal momentum are obtained, among which the most central one is choosen. The top mass can then be reconstructed as the mass of the sum of the b jet, the lepton and the neutrino 4-vectors. The obtained distribution is shown on Fig. 4.14. This simple reconstruction method does not provide a good resolution, and we thus cut only loosely on it. However, it is a natural discriminating variable for advanced methods such as matrix-element methods or kinematical fits.

Finally, a cut was placed on the acoplanarity[2] $\Delta\phi$ of the jet and the lepton, in order to prevent contamination from QCD dijets in which a

[2]The acoplanarity of the event is defined as the angle between the two objects in the transverse detector plane minus π. If the objects are perfectly back to back in this plane, it is thus zero.

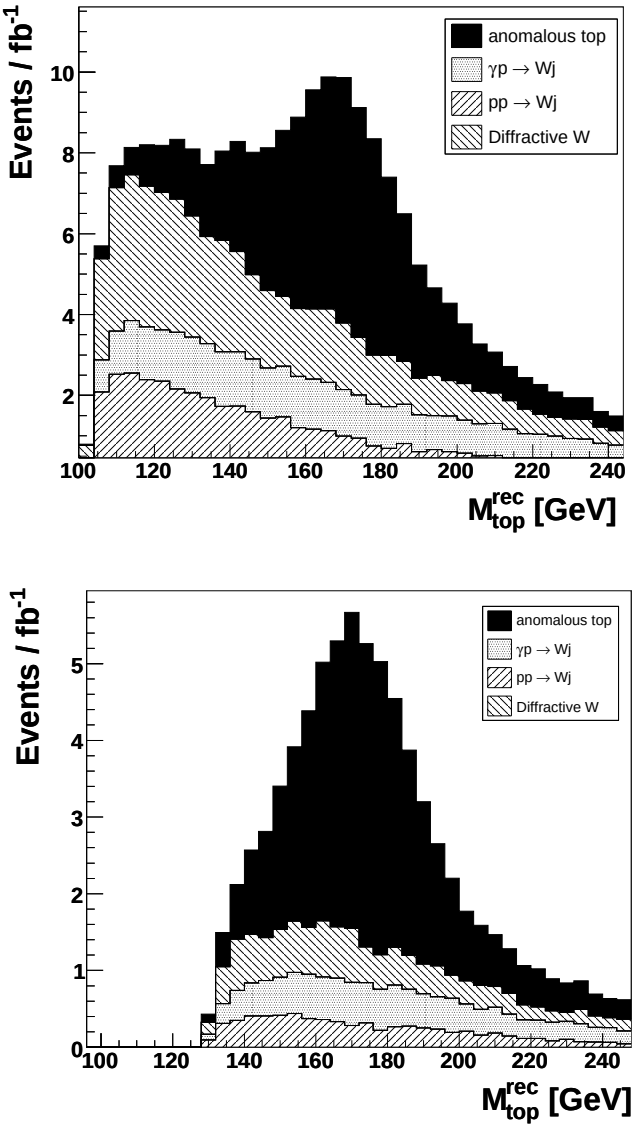

Figure 4.14: Reconstructed top mass cumulative distribution, after acceptance cuts on the jet and the lepton, rapidity gap and exclusivity condition and b-tagging applied on the jet (up) and after full selection (down). Events with a reconstructed top mass between 130 and 200 GeV are selected.

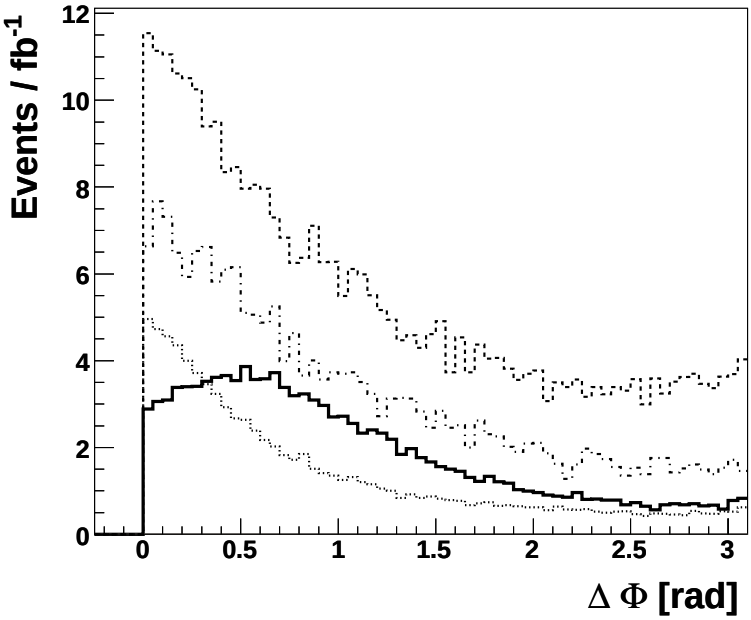

Figure 4.15: Distribution of the acoplanarity $\Delta\phi$ for signal and background events after acceptance cuts. Events with $\Delta\phi > 0.1$ are selected. The bold plain line represents the signal distribution while dashed, dotted and dash-dotted lines represent distributions for partonic, photoproduction and diffractive events respectively.

fake lepton could be reconstructed. Such leptons are coplanar with the opposite jet and the event would be rejected by this cut. The acoplanaity distributions for signal and backgrounds are shown on Fig. 4.15. The values and effect of the described cuts are shown on table 4.3.

Using these cuts, 7.4 (7.3) % of the signal induced by a up(charm) quark in which the W boson decays either to an electron or a muon is selected. This represents 129 signal events for a value of $k_{tu\gamma}$ of 0.15, while the expected background is 35.2 events for an integrated luminosity of 1 fb^{-1}.

4.3.4 Systematic uncertainties

Various sources of systematic uncertainties have been investigated:

Jet energy scale (JES): Jet(s) energy have been scaled up and down

Process	Signal [fb] (efficiency) $k_{tu\gamma} = 0.15, k_{tc\gamma} = 0$	$\gamma p \to W j, c$ [fb]	$pp \to W j, c$ [fb]	Diffractive W [fb]
Detector acceptance	806 (0.464)	3.51×10^3	2.19×10^6	30.5×10^3
Rapidity gap ($E_{min}^{FCAL} < 20$ GeV)	788 (0.453)	3.46×10^3	15.2×10^3	10.3×10^3
Exclusivity (no tracks in $1 < \eta < 2.5$))	665 (0.383)	3.11×10^3	4.60×10^3	4.77×10^3
Isolated lepton ($P_T > 15$ GeV)	629 (0.362)	2.55×10^3	3.97×10^3	4.44×10^3
Tagged b-jet ($P_T > 40$ GeV)	167 (0.096)	27.7	20.6	21.3
Acoplanarity ($\Delta\phi > 0.1$)	158 (0.091)	25.2	18.7	19.3
Missing P_T ($P_T^{miss} > 15$ GeV)	153 (0.088)	23.4	15.6	18.4
Top mass ($130 < M_t < 200$ GeV)	129 (0.074)	13.2	10.0	12.0

Table 4.3: List of all applied cuts and their effect on the visible cross-section of different samples.

by 5 % for jets with $P_T < 30$ GeV, 3 % for jets with $P_T > 50$ GeV and a linear interpolation between these two boundaries [115].

Exclusivity: The track reconstruction efficiency, fixed to 95 % by default, has been moved to 90 % and 99 %.

Rapidity gap: The cut on the energy in the forward calorimeter of the gap side has been moved by 10 % upwards and downwards.

Luminosity: An overall luminosity uncertainty of 5 % has been assumed.

b-tagging: An uncertainty of 5 % has been assumed on b-tagging efficiency and mistagging probability of a c quark jet, while a value of 10 % has been taken for light quarks jets [114].

Theoretical uncertainty: A conservative theoretical uncertainty of 5 % has been taken on all photoproduction processes, as no values could be found in the litterature. Partonic cross-sections after cuts have been assumed to be known to the 2 % level [115]. It is foreseen that the cross-section could be measured at the LHC with high precision and lower this uncertainty [116].

In all cases for which the variable varies upwards and downwards, the maximum of the two variations was taken. The effect of these tests is shown in table 4.4. The estimation of exclusivity and gap induced uncertainties on partonic backgrounds rejection requires random number generation to simulate the track reconstruction efficiency. In that case, the selection was performed several times and computed an average which was close to 8 %. We choose to use the pessimistic value of 10 % to stay conservative. For the rapidity gap requirement, the effect was around 17 % and rounded upwards to 20 %. The case of diffractive backgrounds was treated in a different way due to the large uncertainties linked to the bad knowledge of the survival probability. An overall theoretical uncertainty of 50 % was assumed dominating every other source.

Errors are added linearly when supposed correlated between the different samples, which was assumed for all uncertainties except the theoretical one for which the errors were added quadratically assuming no correlation. The different errors are supposed uncorrelated and added quadratically.

Error	signal (%)	Background (%)				
		$\gamma p \to Wj$	$\gamma p \to Wc$	$pp \to Wj$	$pp \to Wc$	Diffractive W
JES	1.6	2.0	3.0	4.0	3.1	-
Exclusivity	1.0	1.0	1.0	10.0	10.0	-
LRG	0.0	0.0	0.0	20.0	20.0	-
Luminosity	5.0	5.0	5.0	5.0	5.0	-
b-tagging	5.0	10.0	5.0	10.0	5.0	-
Theoretical	5.0	5.0	5.0	2.0	2.0	50.0
total	8.9	18.6				

Table 4.4: Systematic errors on signal and backgrounds

4.3.5 Expected results

The expected background, including uncertainties, for an integrated luminosity of 1 fb^{-1} of data, is:

$$N_B = 35.2 \pm 5.9(\text{stat.}) \pm 6.1(\text{syst.}) \text{ events}$$

This will be used to compute the expected limit for the anomalous couplings, assuming the measured value corresponds exactly to the background only.

Statistical method

The purpose of this study is to estimate the limits that would be set on the anomalous couplings $k_{tu\gamma}$ and $k_{tc\gamma}$. As the number of observed events follows a Poisson distribution, the probability to observe a number N_{obs} events is given by:

$$P(N_{obs}|k_{tu\gamma}, k_{tc\gamma}) = \frac{(N_{signal} + N_{background})^{N_{obs}} \times e^{-(N_{signal}+N_{background})}}{N_{obs}!} \tag{4.6}$$

where $N_{background}$ is the number of selected events predicted by the Standard Model and N_{signal} is the number of selected events coming from anomalous top production:

$$N_{signal} = \left(\varepsilon_u 368 \times k_{tu\gamma}^2 + \varepsilon_c 122 \times k_{tc\gamma}^2\right)\ \mathcal{L}, \tag{4.7}$$

in which $\varepsilon_{u,c}$ is the selection efficiency of the corresponding signal which is in a very good approximation independent of the anomalous couplings and $\mathcal{L}$ is the integrated luminosity corresponding to the sample, in units of pb^{-1}. As our purpose is to set a limit on the anomalous couplings or in the cross-section of the signal, we are interested in the probability density $p(k_{tu\gamma}, k_{tc\gamma}|N_{obs})$. This can be obtained using Bayes Theorem, which requires to choose a prior probability density $p(k_{tu\gamma}, k_{tc\gamma})$. Choosing a uniform prior, the probability density takes the simple form:

$$p(k_{tu\gamma}, k_{tc\gamma}|N_{obs}) = \frac{P(N_{obs}|k_{tu\gamma}, k_{tc\gamma})}{\iint P(N_{obs}|k_{tu\gamma}, k_{tc\gamma})\ dk_{tu\gamma}\ dk_{tc\gamma}}. \tag{4.8}$$

The two dimensional limit is then fixed by the set of points $(k_{tu\gamma}^{max}, k_{tc\gamma}^{max})$ corresponding to some fixed value p^* such that:

$$\iint_{p>p^*} p(k_{tu\gamma}, k_{tc\gamma}|N_{obs})\ dk_{tu\gamma}\ dk_{tc\gamma} = 0.95 \tag{4.9}$$

The same method can be used to set the one dimensional limits by computing $p(\sigma_{signal}|N_{obs})$, using a flat prior for σ_{signal} instead of the anomalous couplings. One should note that the one dimensional limits obtained this way do not correspond to the two dimensional limits obtained by putting one of the couplings to zero, because of the different number of degrees of freedom. Additionally, in order to estimate the effect of systematics, different numbers of observed events have been checked according to the systematic uncertainties.

Results

The one-dimensional limit on the signal visible cross-section, assuming that 35 events are measured where the Standard Model predicts 35.2 is of 13.2 fb. The corresponding 95 % C.L. limits on the couplings are:

$$\begin{aligned} k_{tu\gamma} &< 0.048, \\ k_{tc\gamma} &< 0.084. \end{aligned} \tag{4.10}$$

The two-dimensional allowed region for the couplings is shown on Fig. 4.16 for three different scenarii corresponding to a positive, null or negative variation according to the computed systematic errors.

4.4 Anomalous top search at high luminosity

The rapidity gap based method used at very low luminosity to reject partonic backgrounds does not hold at higher luminosities as the event pileup gets important. However, one can expect that by the time the instantaneous luminosity rises the very forward detector station are all ready for data taking, providing a complementary way of tagging photoproduction events.

4.4.1 Using forward detectors for tagging

In order to simulate the accidental coincidences of single diffractive events and background partonic processes described in the previous chapter, the probability of such a coincidence was computed using the

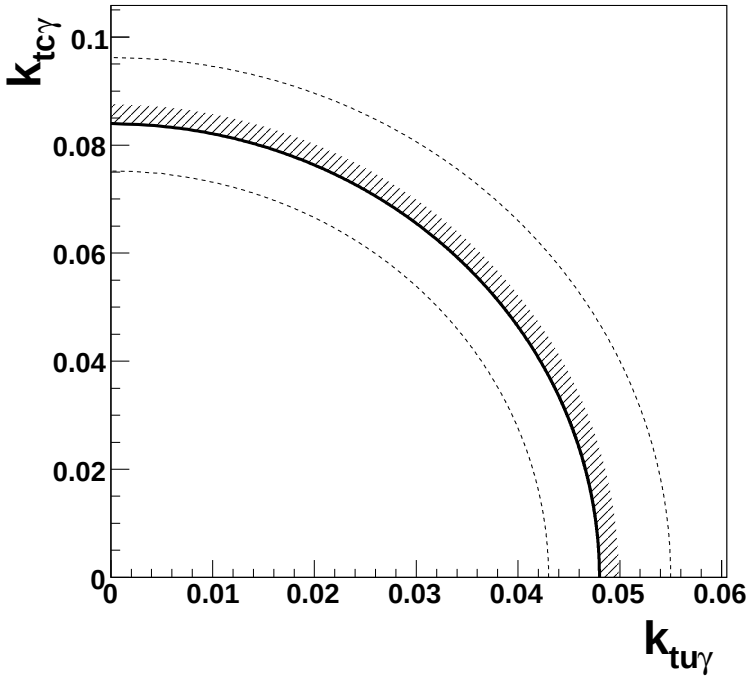

Figure 4.16: Exclusion region for the anomalous couplings after 1 fb^{-1}. The effect of a positive or negative variation of the expected number of events according to the systematic uncertainties is shown by the dashed lines.

Process	Efficiency		
	220 m	420 m	220 m $\oplus$ 420 m
Anomalous top photoproduction	37 %	46 %	83 %
Photoproduction background	52 %	37 %	89 %
Soft diffraction coincidences	15 %	13 %	28 %
Hard diffraction background	49 %	18 %	77 %

Table 4.5: Selection efficiency for signal, photoproduction, single soft diffractive (for the computation of accidental coincidences) and hard diffractive background events when requiring at least one proton tag at 220 m, 420 m or using both stations.

method described in section 3.2.7 and the events were weighted by the obtained reduction factor. For each partonic event, a single diffractive pileup event was simulated using PYTHIA in order to obtain the escaping proton. The energy of the latter was then smeared using a linear fit based on the resolutions showed in Fig. 3.13. Cuts based on the acceptance window obtained using HECTOR were then applied on outgoing protons[3], leading to the requirement that 20 GeV $< E_{loss} <$ 120 GeV for VFDs at 420 m, 4 mm away from the beam and 120 GeV $< E_{loss} <$ 800 GeV for VFDs at 220 m at 2 mm from the beam. The fraction of events selected by these cuts are shown on Table 4.5.

In order to further reject partonic backgrounds, the correlation between the central event and the forward proton measured energy was used. This correlation is illustrated by Fig. 4.17. After reconstructing the event longitudinal momentum from the central detector using relation 4.5, it was compared to the expected longitudinal momentum of an hypothetical top quark reconstructed from the photon energy using:

$$P_{Ztop} = E_\gamma \left(1 - \frac{M^2}{4E_\gamma^2}\right) \tag{4.11}$$

The result of this comparison is shown on Fig. 4.18. The variable ΔP_Z is defined as the difference between the two longitudinal momentum and events for which $|\Delta P_Z| <$ 100GeV are selected.

[3]The acceptances corresponding to beam 1 and beam 2 were averaged.

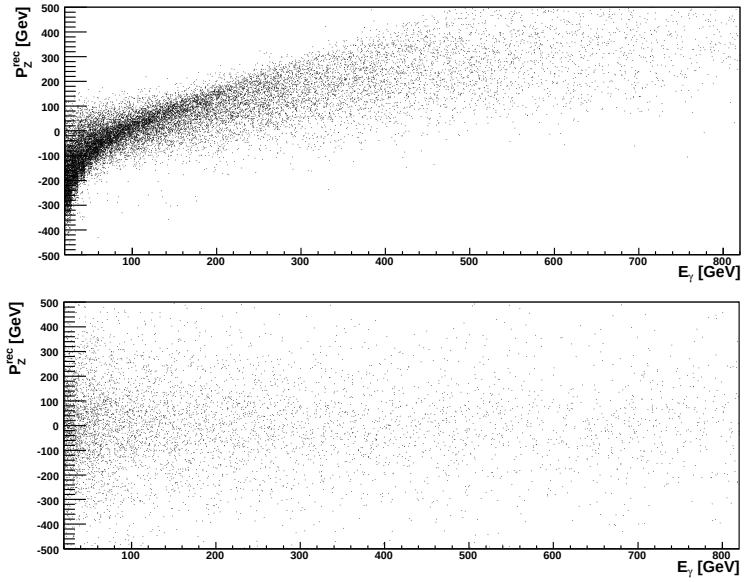

Figure 4.17: Total longitudinal momentum of the central event versus photon energy for the signal (top) and the partonic backgrounds (bottom). One clearly sees the lack of correlation between the central event and the photon in partonic backgrounds.

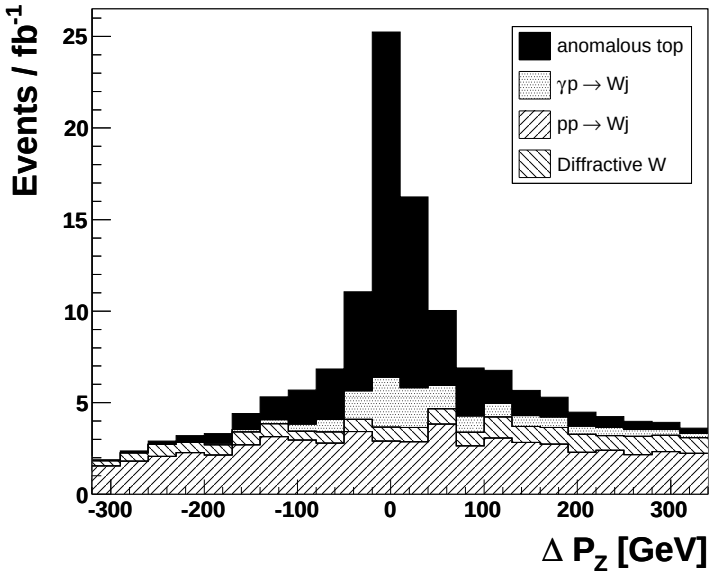

Figure 4.18: Cumulative distribution of the ΔP_Z variable after acceptance cuts on the lepton and the jet, application of the exclusivity condition and proton tagging

4.4.2 Using forward detectors for reconstruction

The fact that in the case of single top photoproduction only one proton survives and can be tagged prevents from completely constraining the kinematics. It can however contribute to the event reconstruction, especially in the present case for which the mass of the photon-quark system is know to be the top mass.

Under the assumption that the invariant mass of the quark-photon system corresponds to the world average mass of the top quark, the measurement of the proton energy from the forward proton allows, as described before, to compute the top quark momentum.

Using equation 4.11, the top quark Lorentz boost γ_L can be expressed as:

$$\begin{aligned} \gamma_L &= \frac{E_t}{M_t} \\ &= \sqrt{\frac{M_t^2 + P_t^2}{M_t^2}} \\ &= \sqrt{\frac{1}{2} + \frac{E_\gamma^2}{M_t^2} + \frac{M_t^2}{16E_\gamma^2}}. \end{aligned} \tag{4.12}$$

Applying the corresponding boost to the reconstructed b-jet and the lepton, one gets their 4-vectors in the centre of mass frame of the top quark. In this frame, the energy of the b quark is fixed by the usual two-body decay formula:

$$E_b = \frac{M_t^2 + M_b^2 - M_W^2}{2M_t} \tag{4.13}$$

This theoretical value is compared with the value obtained by boosting the reconstructed b-jet 4-vector. This is illustrated by Fig. 4.19 where the peak associated to the anomalous top production is shown over illustrative backgrounds. The reconstructed center of mass energy of this jet was required to lie within 15 GeV around the theoretical value.

Assuming that the b-jet direction is close to the direction of the original b quark yields the direction of the W boson. As the W mass is known, the boost of the boson is completely constrained and can be computed in the top quark centre of mass frame. Applying the opposite of the W boost to the lepton 4-vector gives this vector in the rest frame

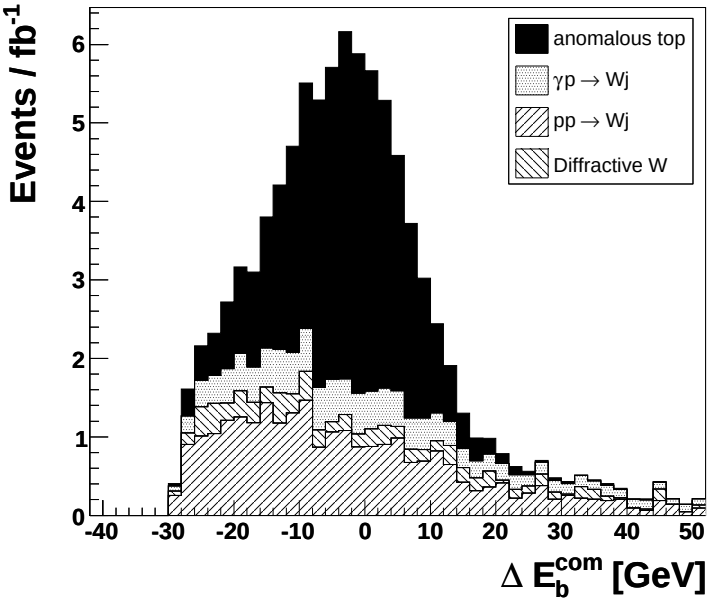

Figure 4.19: Distribution of the b-jet energy the centre of mass frame of the top quark, reconstructed using the photon energy information from very forward detectors. Basic acceptance cuts, exclusivity condition, b-tagging and proton tag were required

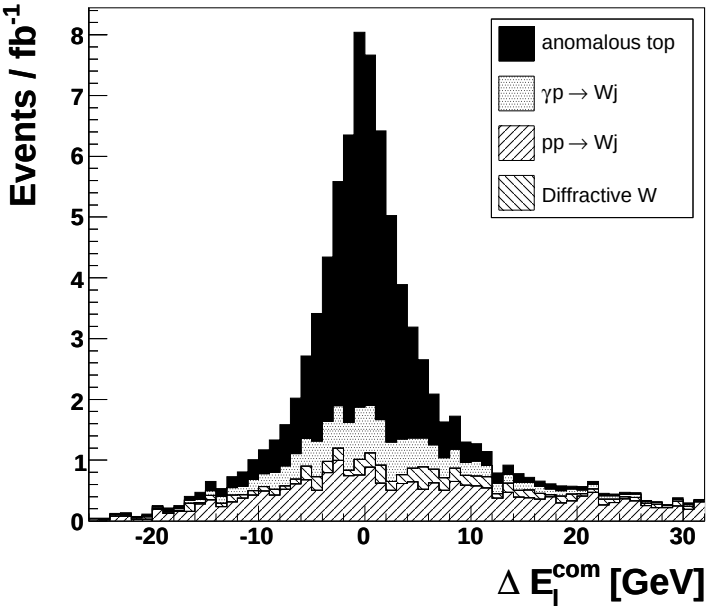

Figure 4.20: Distribution of the lepton energy the centre of mass frame of the W boson, reconstructed using the photon energy information from very forward detectors and the b-jet direction from the central detector. Basic acceptance cuts, exclusivity condition, b-tagging and proton tag were required

of the W boson. The energy of the lepton is known in that frame to be half of the W mass, and the same comparison as before can be applied. As the lepton energy is generally better reconstructed than the jet one, the signal peak is even sharper, as illustrated by Fig. 4.20. Events with an energy less than 5 GeV away from the theoretical value were selected.

4.4.3 High luminosity photoproduction without very forward detectors

There are two reasons to consider studying photoproduction at luminosities for which pileup is not negligible without very forward detectors. First, the full set of VFDs will possibly not be installed before high luminosities are reached. Secondly, photoproduction tagging using VFDs becomes harder at very high luminosities because of the rise of acciden-

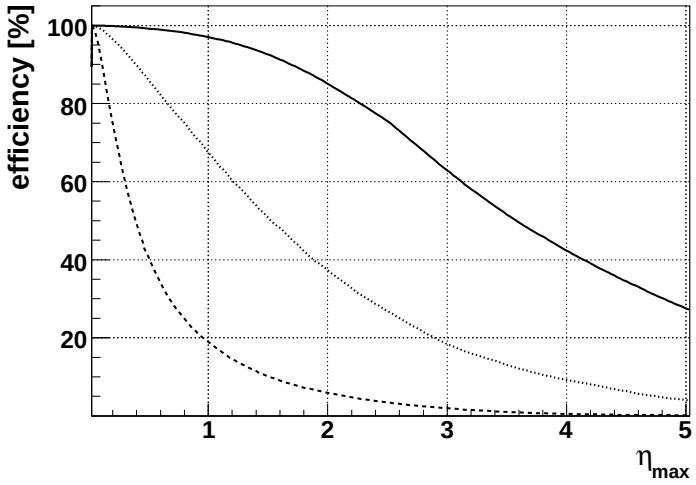

Figure 4.21: Selection efficiency as a function of η_{max} for the signal (plain), hard diffractive W production (dotted) and partonic backgrounds (dashed).

tal coincidences and of multiple hits in the detectors which reduces the signal selection efficiency while increasing the background from partonic processes.

In such cases, one can use the exclusivity condition described in the previous chapter using the whole coverage of the tracking device, as one can select tracks associated with the primary vertex and thus essentially ignore event pileup. In the present analysis, η_{max} is defined as the distance between the edge of the tracker and the first visible track. This value is computed for both sides of the detectors, then the maximum of both sides is taken as the discriminating variable. Tracks associated with the reconstructed lepton and jet[4] are not taken into account. The selection efficiency for signal and background as a function of the cut on η_{max} is shown on Fig. 4.21. For the present analysis, the full tracking device was used, requiring[5] $\eta_{max} > 4.6$.

[4] A $\eta - \phi$ cone of size 1.0 was defined around the jet direction.

[5] As the tracker expands from $\eta = -2.5$ to $\eta = 2.5$, the maximum size of η_{max} is theoretically 5 units. However, one can expect that the track reconstruction efficiency around the edges is not good, so we took a more conservative value of 4.6.

4.4.4 Selection

Apart from the rapidity gap requirement which is replaced by the requirement of a VFD tag, the selection used at high luminosity is similar to the selection in absence of event pileup, with additional cuts based on event reconstruction using the information from the VFDs. The detail and effect of the cuts is given on table 4.6 using the hypothesis of a luminosity of $2 \times 10^{33}\text{cm}^{-2}\text{s}^{-1}$ for the computation of accidental coincidences. The corresponding numbers for the case in which no VFDs are present and thus using the strong exclusivity cut described in the previous section is shown on table 4.7.

4.4.5 Systematic uncertainties

The same systematic uncertainties as in the scenario of very low luminosity have been used. There is however obviously no uncertainty linked to the rapidity gap requirement.

On the other hand, the very forward detectors bring new sources of uncertainty. Any misalignement would indeed induce a bias in the reconstructed photon energy, as was shown in section 3.2.6. However, detectors placed at 420 m from the interaction point can be calibrated in a very efficient way after only hours of data taking, providing an unbiased reconstructed energy and no uncertainty was assumed on these detectors. Considering the 220 m detectors, moving quadrupoles one by one by 0.5 mm showed effects on the energy ranging from 3 GeV to 15 GeV depending on the affected magnet. The effect of a 15 GeV bias upwards and downwards on the selection was computed. This brings an additionnal 1.1 % uncertainty on the signal selection efficiency, along with uncertainties of 2.6 %, 12.5 % and 16.7 % on the photoproduction, partonic and diffractive backgrounds respectively.

The total systematic uncertainty amounts to 10.8 % on the background and 9.0 % on the signal.

4.4.6 Expected Results

As one can not be sure of the running scenario that will take place after the very forward detectors of the FP420 project are installed in 2010, we choose to consider various luminosity scenarios, namely luminosities of 10^{33}, 2×10^{33} or 10^{34} cm^{-2} s^{-1}, considering associated integrated luminosities of 10, 30 or 100 fb^{-1}. The limits obtained without forward

Process	Signal (efficiency) $k_{tu\gamma} = 0.15, k_{tc\gamma} = 0$	$\gamma p \to Wj, c$	$pp \to Wj, c$	Diffractive W
Detector acceptance	24.2 $\times 10^3$ (0.464)	105.3 $\times 10^3$	65.7 $\times 10^6$	916 $\times 10^3$
Tagged proton (220m + 420m)	16.6 $\times 10^3$ (0.318)	84.9 $\times 10^3$	11.9 $\times 10^6$	643 $\times 10^3$
Exclusivity (no tracks in $1 < \eta < 2.5$)	13.4 $\times 10^3$ (0.257)	76.3 $\times 10^3$	521 $\times 10^3$	156 $\times 10^3$
Isolated lepton ($P_T > 15$GeV)	12.7 $\times 10^3$ (0.244)	62.3 $\times 10^3$	487 $\times 10^3$	147 $\times 10^3$
Tagged b-jet ($P_T > 40$GeV)	3.34 $\times 10^3$ (0.064)	623	2.04 $\times 10^3$	717
Acoplanarity ($\Delta\phi > 0.1$)	3.18 $\times 10^3$ (0.061)	566	1.81 $\times 10^3$	651
ΔP_Z ($-100 < \Delta P_Z < 100$GeV)	2.45 $\times 10^3$ (0.047)	289	467	147
C-o-M kinematics	1.82 $\times 10^3$ (0.035)	97.1	57.2	19.7
Missing P_T ($P_T^{miss} > 15$GeV)	1.77 $\times 10^3$ (0.034)	91.6	57.2	19.7
Top mass ($130 < M_t < 200$GeV)	1.72 $\times 10^3$ (0.033)	86.6	50.3	19.7

Table 4.6: List of all applied cuts and their effect on the number of selected events of different samples after 30 fb^{-1} for an instantaneous luminosity of 2×10^{33} cm^{-2} s^{-1} Using very forward detectors at 220m and 420m for tagging and reconstruction. The cuts on the center of mass kinematics using the recontructed photon energy are $\Delta E_b < 15$GeV and $\Delta E_l < 5$GeV

Process	Signal (efficiency) $k_{tu\gamma} = 0.15, k_{tc\gamma} = 0$	$\gamma p \to W j, c$	$pp \to W j, c$	Diffractive W
Detector acceptance	24.2 $\times 10^3$ (0.464)	105 $\times 10^3$	65.7 $\times 10^6$	916 $\times 10^3$
Exclusivity ($\eta_{max} > 4.6$)	8.14 $\times 10^3$ (0.156)	54.5 $\times 10^3$	155 $\times 10^3$	51.9 $\times 10^3$
Isolated lepton ($P_T > 15$GeV)	7.62 $\times 10^3$ (0.146)	42.8 $\times 10^3$	148 $\times 10^3$	49.3 $\times 10^3$
Tagged b-jet ($P_T > 40$GeV)	2.08 $\times 10^3$ (0.040)	441	632	262
Acoplanarity ($\Delta\phi > 0.1$)	1.98 $\times 10^3$ (0.038)	401	574	235
Missing P_T ($P_T^{miss} > 15$GeV)	1.93 $\times 10^3$ (0.037)	377	523	222
Top mass ($130 < M_t < 200$GeV)	1.51 $\times 10^3$ (0.029)	166	324	105

Table 4.7: List of all applied cuts and their effect on the number of selected events of different samples after 30 fb^{-1} for an instantaneous luminosity of 2×10^{33} cm^{-2} s^{-1} using no forward detectors.

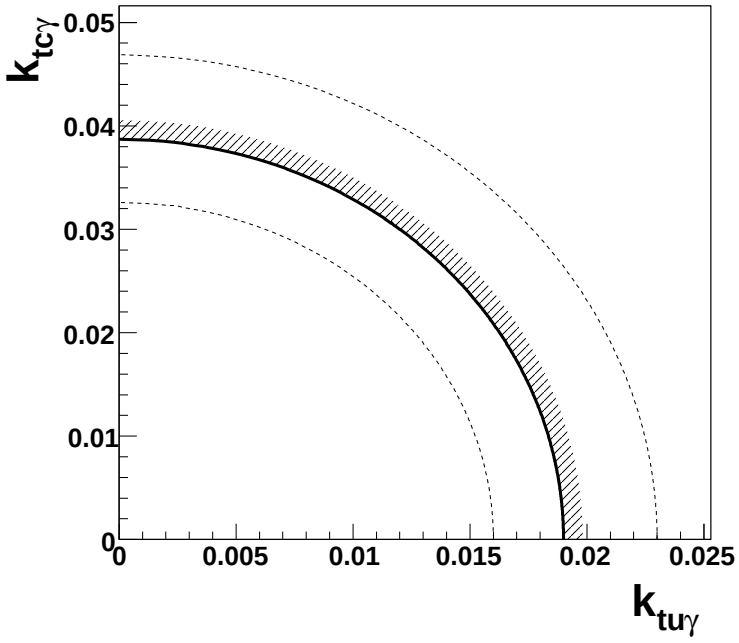

Figure 4.22: Two-dimensional limits on the anomalous couplings $k_{tu\gamma}$ and $k_{tc\gamma}$ (solid) for the intermediate scenario of an instantaneous luminosity of $2 \times 10^{33}\text{cm}^{-2}\text{s}^{-1}$ and 30 fb^{-1} of integrated luminosity using VFDs for tagging and reconstruction. The other lines correspond to a positive or negative variation of the observed number according to the systematic uncertainty.

detectors are also computed, using exclusivity on the whole tracking detector as described in section 4.4.3.

The statistical method described above has been used to estimate the limit one can expect to obtain on the anomalous parameters if the number of observed events corresponds to the SM expected number. The results are summarised in table 4.8 along with the one dimensional limits on the anomalous couplings. The two dimensional limit is shown on Fig. 4.22, along with the effect of systematic errors, for the intermediate scenario of an instantaneous luminosity of $2 \times 10^{33}\text{cm}^{-2}\text{s}^{-1}$ and 30 fb^{-1} of integrated luminosity.

These numbers were computed assuming very forward detectors approaching the beam as close as 2 mm (220 m) and 4 mm (420 m). As was

Scenario		signal	background			$k_{tu\gamma}$ limit	$k_{tc\gamma}$ limit
		($k_{tu\gamma} = 0.15$)	pp	γp	Diff.		
10^{33}cm^{-2}s^{-1}, 10 fb^{-1}	VFDs	0.63 $\times 10^3$	9	33	7	0.024	0.039
	no VFDs	0.53 $\times 10^3$	108	55	35	0.036	0.069
2×10^{33}cm^{-2}s^{-1}, 30 fb^{-1}	VFDs	1.72 $\times 10^3$	50	91	20	0.019	0.031
	no VFDs	1.51 $\times 10^3$	324	166	105	0.027	0.052
10^{34}cm^{-2}s^{-1}, 100 fb^{-1}	VFDs	2.62 $\times 10^3$	501	138	30	0.021	0.035
	no VFDs	5.33 $\times 10^3$	1080	553	350	0.020	0.038

Table 4.8: Expected number of events and limits on the anomalous couplings for three different LHC running scenarii, namely $10^{33}, 2 \times 10^{33}$ or 10^{34} cm^{-2} s^{-1}. The limits do not include systematic uncertainties.

Scenario	Signal	$\gamma p \to W j, c$	$pp \to W j, c$	Diff. W
220 m : 2 → 3 mm	- 5 %	- 5 %	- 6 %	- 0 %
420 m : 4 → 5 mm	- 15 %	- 17 %	- 11 %	- 13 %
both stations moved	- 20 %	- 22 %	- 17 %	- 13 %

Table 4.9: Effect of an additional 1 mm distance between VFD stations and the beam on the selection efficiency obtained using both stations.

discussed in the previous chapter, these values are not fixed yet. The effect of an additional distance of 1 mm on the selection efficiency of both signal and background was computed and is shown in table 4.9. For the typical case of 30 fb^{-1} at 2×10^{33}cm^{-2}s^{-1}, moving the two stations by 1 mm causes a 20 % (19.3 %) signal (background) loss, leading to a 4.5 % degradation of the 95 % C.L. limit on the anomalous couplings.

4.5 Anomalous triple gauge couplings

It has been showed in the previous sections that the presence of large anomalous FCNC couplings would lead to an excess of events featuring an isolated lepton and a high P_T jet. However, such an excess could also be the consequence of anomalous γW^+W^- couplings as these could enhance W boson photoproduction. The CalcHep program has been used to generate events using the effective Lagrangian of equation 1.27 for values of the anomalous couplings $\Delta\kappa$ and λ of ± 0.1 and ± 0.05 respectively, roughly corresponding to the LEP 95 % limits. Simulations showed that the effect of anomalous couplings would be especially strong at high mass of the W + jet system, leading to high P_T jets.

Two selections were performed on these events: first the exact same selection as for the anomalous top search was applied in order to estimate the effect of anomalous triple gauge couplings on this study. Then, we looked at events with one isolated lepton with $P_T > 15$ GeV and a single jet, requiring this jet to have $P_T > 100$ GeV as it is expected that the effect of anomalous couplings is especially strong at high P_T. This "high P_T" sample is expected to be especially sensitive to anomalous couplings. Partonic backgrounds were reduced using VFDs and exclusivity on the photon side as in the case of high luminosity search with VFDs. The effect of a cut on the jet transverse momentum is shown on Fig. 4.23.

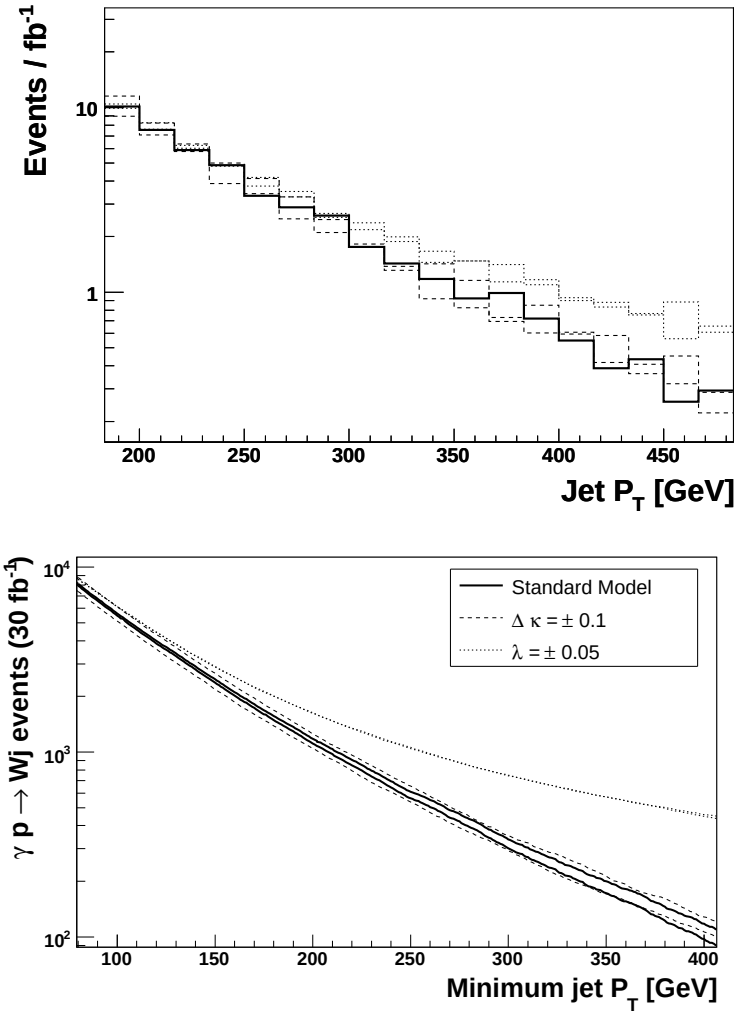

Figure 4.23: Distribution of the jet transverse momentum P_T (top) and effect of a cut on this variable on the selected sample for W photoproduction (bottom). Dashed and dotted lines correspond to anomalous couplings. The numbers shown on both plots are obtained after requiring a single hit in the VFDs, exclusivity on the photon side and an isolated lepton with $P_T > 15$ GeV. The bottom plot shows the number of observed events after 30 fb^{-1}. The two plain lines on this plot represent one sigma deviations from the SM scenario.

Physics case	Very low lumi		Low lumi with VFDs	
	Normal	High P_T	Normal	High P_T
SM expected [fb]	35.2	566	5.2	611
Anomalous top				
(95 % C.L. limit)	+ 30.8 %	-	+ 22.3 %	-
$\Delta\kappa = +0.1$	+ 2.0 %	+ 12.4 %	+ 1.4 %	+ 6.2 %
$\Delta\kappa = -0.1$	- 6.5 %	- 8.9 %	- 12.7 %	- 4.9 %
$\lambda = +0.05$	- 2.5 %	+ 11.1 %	- 9.2 %	+ 6.2 %
$\lambda = -0.05$	- 3.0 %	+ 9.2 %	- 4.7 %	+ 6.2 %

Table 4.10: Effect of the anomalous couplings on the visible cross-section after the full analysis described in this chapter ("Normal") and using the high P_T jet selection described in this section. Diffractive and partonic backgrounds are included in the computation of the effect. A luminosity of 2×10^{33} cm^{-2} s^{-1} was assumed for the computation of accidental coincidences of the "low lumi" scenario.

The effect of anomalous couplings on the visible W + jet photoproduction cross-section are shown in table 4.10. One sees how the two physics cases decouple.

In the very low luminosity case, after 1 fb^{-1}, one standard deviation represents approximately 4 % of the high P_T sample and only maximal variations of the couplings could be seen. On the other hand, the effect of these maximal variations on the anomalous top analysis is expected to be small.

For an integrated luminosity of 30 fb^{-1} at 2×10^{33}cm^{-2}s^{-1}, this sensitivity goes as low as 0.7 %. Variations due to large anomalous triple gauge couplings can thus be detected and decoupled from the effect of anomalous top production.

4.6 Conclusions and perspectives

The analysis performed considering only 1 fb^{-1} of data, corresponding to few months of LHC running at 10^{33} cm^{-2} s^{-1}, showed the potential to improve the actual limit on the anomalous coupling $k_{tu\gamma}$ while getting the first limit on $k_{tc\gamma}$. At higher luminosity, it was shown that the problems linked to the event pileup can be efficiently solved using very

forward detectors, and this mostly independently of the instantaneous luminosity. The case for which there are no VFDs was also investigated, showing comparable results, especially at the highest LHC luminosity. The influence of systematic uncertainty was showed to change the limits by less than 15 % in all cases.

On the other hand, the CMS and ATLAS collaborations have studied the possibility of measuring these couplings through pair production of top quarks, one of them decaying into a photon and an up or charm quark and through the associated production of a top quark and a photon [117, 118, 119]. The limit obtained by CMS in the FCNC decay analysis is similar to the one obtained here, while the ATLAS $k_{tq\gamma}$ limit improved from around 0.015 to 0.005 assuming 10 fb^{-1} of luminosity without pileup by switching to a likelihood-based analysis. Because of these similar sensitivities, the different approaches can be considered complementary.

Moreover, measuring the branching ratio of the top into a photon and a jet leads to symmetrical limits on $k_{tu\gamma}$ and $k_{tc\gamma}$, while the present analysis has significantly different sensitivities to the two couplings. Consequently, if a compatible excess was to be seen in both channels, the combination of the two results would directly provide the values of both couplings, as illustrated by Fig. 4.24.

Perspectives

The present analysis was based on a collection of cuts. Another approach would have been a likelihood-based analysis. The study made by ATLAS showed significative improvements when switching to such an analysis to draw limits on the anomalous couplings, which suggests that similar improvements can be expected on this analysis.

A full detector simulation is another natural improvement of the current analysis, as some variables are very sensitive to detector parameters such as track reconstruction efficiency for the exclusivity cuts and noise in the calorimeters for the rapidity gap requirements.

A realistic trigger simulation would also improve the actual analysis, as trigger selection efficiencies were not considered. Both ATLAS and CMS use a muti-level trigger system. The value of 15 GeV for the lepton P_T cut used here roughly corresponds to the high level trigger values that will be used by CMS at low luminosities. At higher luminosities, the CMS first level trigger will select events with a muon or electron with P_T higher than 14 GeV and 22 GeV respectively, while the high level

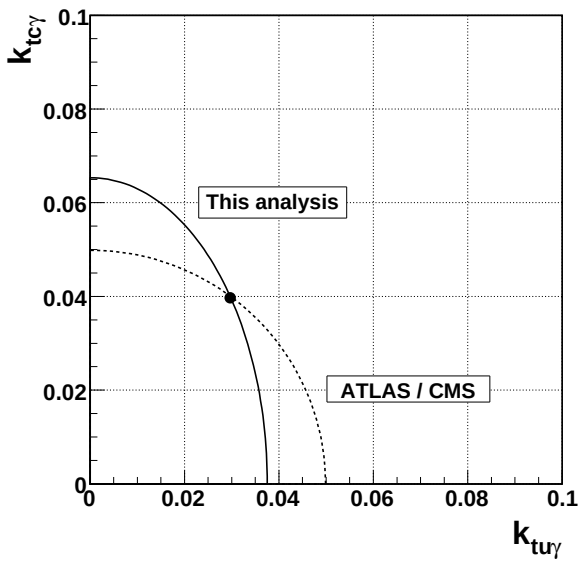

Figure 4.24: Illustration of the effect of the combination of the present analysis with results from top FCNC decay, assuming the latter show an excess corresponding to $k_{tq\gamma} = 0.05$. The dashed line corresponds to the allowed values for both couplings according to an analysis based on top decay, while the plain line is based on the top photoproduction analysis of the present work (with arbitrary results for the purpose of illustration). The black dot at the intersection gives the most probable value for the couplings. Contours can be obtained by combining the results using a likelihood approach.

trigger rises these cuts to 19 and 26 GeV [120]. Taking these values for the cuts in the present analysis changes the significance $S/\sqrt{B}$ by less than 7 %, leading to changes in the 95 % C.L. limits on the couplings of around 3 %.

Conclusion

The search for W bosons at HERA performed in the first part of this work provides a significant test of the Standard Model. The measured value of $0.97^{+0.75}_{-0.57}$ pb for the cross-section of W boson production at HERA is in good agreement with the Standard Model expectations of $\sim$ 1 pb. Although it was based only on events for which the W boson decays into an electron and a neutrino, it is consistent with other measurements by the ZEUS collaboration based on final states including jets or muons. It does not confirm the excess of events with high P_T isolated leptons observed by the H1 collaboration. On the other hand, the search for top quarks produced through FCNC requires a good understanding of this process which appears as the main background in the analysis.

The challenges of studying photoproduction events at the LHC exceed a lot those confronted at HERA. There, photoproduction events will be dominated by orders of magnitude by partonic events. Moreover, the composite nature of protons increases the complexity of the computation of photon fluxes. We have shown that partonic cross-sections can be reduced to the level of photoproduction ones using various methods that can be combined in different ways according to pileup and detector scenarios. The very forward detectors offer in this context an important way to select photoproduction events. However, these require particular simulations of the path of particles in the beam, which lead to the developpement of the HECTOR software. The matter of photoproduction tagging using such detectors raises new questions such as the influence of accidental coincidences and the developpement of methods aiming at the reconstruction of the initial state of the measured proton, which were adressed in details.

The analysis of single top photoproduction at the LHC through FCNC was based on these tagging techniques and showed their efficiency. By combining selections based on rapidity gaps, exclusivity conditions and tagging very forward detectors, it was shown that sensitivities similar to the ones expected in top FCNC decay analysis can be reached independently of the value of the instantaneous luminosity. Especially, the present world limit of 0.14 on the anomalous coupling $k_{tu\gamma}$ is expected to be improved by a factor three after only one fb^{-1} of integrated luminosity. At higher luminosities, despite of the presence of important event pileup, this limit is expected to be improved to 0.019, one order of magnitude lower than the present limit, after 30 fb^{-1} of integrated luminosity. Finally, the sensitivity of this analysis to potential anomalous triple gauge couplings (ATGCs) has been studied, showing that the effects of FCNC and ATGC could be separated. In addition, the important effect of ATGCs on events including W bosons and jets with very high transverse momentum offers an interesting opportunity of novel and original studies of triple gauge couplings in W boson photoproduction at the LHC.

Remerciements / Acknowledgements

This thesis is the fruit of many collaborations. It is a general rule that one does not do science without getting inspired and helped by others, and I was happy to benefit from the abundant help of many people. Most naturally, first comes my advisor Krzysztof Piotrzkowsky. His ideas are the fundation of this work, and his advices brought it to its final state.

Similarly important in my eyes are the people which spent time working with me, side by side, for many hours. Among these, the first is Xavier Rouby, which was not bored enough after spending fours years in courses with me and spent months, not only designing and coding HECTOR, but discussing all the matters of ours respective works. Our views of problems often complemented themselves and I hope he benefited of this continuous collaboration as much as I did. The second most patient person in the world is James Ferrando, which spent many hours helping me understanding HERA physics and computing, debugging codes and discovering foreign beers. I can not thank him enough for this time he shared with me.

There are many other coworkers who deserve to be quoted here (in random order): Vincent Lemaître for advices in almost every field, Muriel Vander Donckt for reading and commenting large parts of this thesis, Dominique Belge for chocolate breaks, Ginette Tabordon for encouragements, Christophe Delaere for amazing support on all programming issues, Severine Ovyn for some fruitful collaborations and Vincent Boucher for listening to me when I started to get sick of my thesis. In general, working at the "cyclotron" was made a pleasure by all peo-

ple working there every day. A general thank goes to my colleagues, especially the "cyclotrolls" team.

Je tiens aussi à remercier mes parents, ma famille, ma belle-famille et tous les amis qui m'ont soutenu pendant la durée de cette thèse, et spécialement pendant les derniers mois qui auraient sans doute été insupportables sans ce soutient.

Le soutient, je l'ai trouvé avant tout auprès de Marie. Son amour, sa patience m'ont permis de mener ce travail à bien. Je dois aussi beaucoup à Joachim et Claire qui me donnent tant de joies.

Appendix A

Hector, a fast simulator for particles in beamlines

There exists a certain number of softwares designed to simulate particle propagations in magnetic fields or more specifically in storage rings. However, for the needs of an experiment like CMS or ATLAS, some points become very important:

Programming language: The simulation software of both CMS and ATLAS collaborations is based on C++ code. It is thus far easier and transparent to the user if all the code is based on the same language.

Single-particle simulation: The simulation should be run on a particle by particle basis, as the purpose is not to compute global statistics but to have montecarlo simulation of physics events with a given number of particles going in the forward region. Programs aiming at the simulation of the whole beam, as MAD-X for instance, don't fit this need by design.

Speed: One may design a full simulation of the beamline, along with interactions with matter and intra-beam interactions. However, speed is a key point when dealing with detector simulation, and this requires some simplifications while ensuring sufficiently accurate simulation.

Adaptability: The choice was made to design a tool which may be adapted to any beamline, not only the LHC, by the simple change

of a file and a few beam parameters. As a matter of fact, HECTOR is already used at CMS as an official tool, but also by the ATLAS and STAR collaborations.

No existing software fits these requirement. The closest candidate, TRANSPORT [121] which is fast, accurate and can simulate the propagation of a single particle, is unfortunately written in FORTRAN. A new tool was thus needed, and this conclusion lead to the development of HECTOR. The program also benefits from the classes of the cern's ROOT [122] analysis software in order to provide handy tools to the user for his analysis. One should note that HECTOR presents itself more as a framework than as a pre-compiled software. This adds to the adaptability as pieces of code using HECTOR can thus be included in any simulation or analysis code.

Many results of HECTOR have already been presented in the present dissertation. This chapter aims at presenting the simulation methods used and to give an introduction on how to use the program.

A.1 The basics of beam simulation

The Lorentz force acting on a moving particle in a magnetic field $\vec{B}$ is given by:

$$\vec{F} = \frac{d\vec{p}}{dt} = q\vec{v} \wedge \vec{B} \tag{A.1}$$

where q is the particle charge and $\vec{v}$ its velocity. Let us consider a co-moving coordinate system in which the s coordinate goes along the particle trajectory, x is horizontal and y is vertical. Considering horizontal bending of the beam path with radius R, one gets:

$$\frac{1}{R} = \frac{q}{p} B_y, \tag{A.2}$$

which can be expanded around the centre of the magnet as:

$$\frac{q}{p} B_y(x) = \frac{q}{p} B_y(0) + \frac{q}{p} \frac{\partial B_y}{\partial x} x + \frac{q}{2p} \frac{\partial^2 B_y}{\partial^2 x} x^2 + ... \tag{A.3}$$

This corresponds to a development of the magnetic field B as a sum of multipoles. In the case of beam magnets, only one term will in general be considered at a time. For instance, a dipole has only a bending effect

described by the first term, whereas a quadrupole does not have this effect and can be described by the second term only. Sextupoles however have both behaviours and their description should then take both terms into account. In the following calculations, we use the following definitions:

$$\frac{1}{R} = \frac{q}{p} B_y(0) \tag{A.4}$$

$$k = \frac{q}{p} \frac{\partial B_y}{\partial x} \tag{A.5}$$

The ideal path of a particle in the ring, fixed by design, is called the *orbit*. We are only interested in computing the position of a particle relatively to this orbit for most of the practical applications. In order to achieve this, we use the co-moving coordinate system which follows the path of the orbit. This path is in particular bent by dipoles, and the coordinate system will be rotated accordingly.

If we define:

$$\dot{x} = \frac{\partial x}{\partial t}, \tag{A.6}$$

$$x' = \frac{\partial x}{\partial s}, \tag{A.7}$$

we get the following by including the coordinate system rotation:

$$\dot{\vec{x}} = x'\dot{s}\hat{x} + y'\dot{s}\hat{y} + \left(1 + \frac{x}{R}\right)\dot{s}\hat{s} \tag{A.8}$$

$$\begin{aligned} \ddot{\vec{x}} &= \left[x''\dot{s}^2 + x'\ddot{s} - \left(1 + \frac{x}{R}\right)\frac{\dot{s}^2}{R}\right]\hat{x} \\ &+ \left[z''\dot{s}^2 + z'\ddot{s}\right]\hat{y} + \left[\frac{2}{R}x'\dot{s}^2 + \left(1 + \frac{x}{R}\right)\ddot{s}\right]\hat{s} \end{aligned} \tag{A.9}$$

The Lorentz equation A.1 gives then (considering no longitudinal field B_z and no acceleration $\ddot{s}$):

$$\begin{aligned} x'' &= \left(1 + \frac{x}{R}\right)\left(\frac{1}{R} - \frac{v}{\dot{s}}\frac{q}{p}B_y\right) \\ y'' &= \left(1 + \frac{x}{R}\right)\frac{v}{\dot{s}}\frac{q}{p}B_x \end{aligned} \tag{A.10}$$

On a typical beamline composed only of horizontally bending dipoles and of quadrupoles, one can write:

$$\frac{q}{p}B_x = -ky \tag{A.11}$$

$$\frac{q}{p}B_y = \frac{1}{R} - kx. \tag{A.12}$$

By inserting these into A.10 and assuming only small energy losses, we get the final equations:

$$\begin{aligned} x'' + \left(\frac{1}{R^2} - k\right)x &= \frac{1}{R}\frac{\Delta p}{p} \\ y'' + ky &= 0. \end{aligned} \tag{A.13}$$

Those equations should then be solved individually for any type of beam element we want to consider. We will here treat the case of dipoles and quadrupoles, as those are the only two types of magnets that are encountered in the LHC beamlines around the interaction points.

A.1.1 Matrix formalism for beam particles

We will now solve the equations of the previous section for beam particles, thus neglecting the energy losses. This effect will be treated separately later. In the case of an horizontally bending dipole of length l, the equations A.13 become:

$$x''(s) + \frac{1}{R^2}x(s) = 0 \tag{A.14}$$

$$y''(s) = 0. \tag{A.15}$$

The vertical (y) trajectory is obviously a straight line, while in the horizontal(x) plane, we get the following solutions:

$$x(s) = x_0 \cos\frac{l}{R} + x_0' R \sin\frac{s}{R} \tag{A.16}$$

$$x'(s) = -x_0\frac{1}{R}\sin\frac{l}{R} + x_0'\cos\frac{s}{R}, \tag{A.17}$$

which represents the rotation of an angle l/R of a (x, x') vector and thus a focusing of the beam. This effect can be written in a matrix formalism:

$$\begin{pmatrix} x(l) \\ x'(l) \end{pmatrix} = \begin{pmatrix} \cos\frac{l}{R} & R\sin\frac{l}{R} \\ \frac{-1}{R}\sin\frac{l}{R} & \cos\frac{l}{R} \end{pmatrix} \begin{pmatrix} x_0 \\ x'_0 \end{pmatrix}$$

Including the y components of the vector which becomes (x, x', y, y'), one gets the dipole matrix:

$$M_{dipole} = \begin{pmatrix} \cos\frac{l}{R} & R\sin\frac{l}{R} & 0 & 0 \\ \frac{-1}{R}\sin\frac{l}{R} & \cos\frac{l}{R} & 0 & 0 \\ 0 & 0 & 1 & l \\ 0 & 0 & 0 & 1 \end{pmatrix}.$$

where the lower-left part corresponds to a straight propagation which will be used for all so-called *drift sections* Corresponding to places where no magnetic field takes place. Solutions for quadrupoles lead to two kinds of solutions depending on the sign of the k variable. We define $\Omega = l\sqrt{|k|}$ to get:

$$\begin{aligned} k < 0 \quad &\Rightarrow \quad M_{quadrupole} = \begin{pmatrix} \cos\Omega & \frac{1}{\sqrt{|k|}}\sin\Omega \\ -\sqrt{|k|}\sin\Omega & \cos\Omega \end{pmatrix} \\ k > 0 \quad &\Rightarrow \quad M_{quadrupole} = \begin{pmatrix} \cosh\Omega & \frac{1}{\sqrt{|k|}}\sinh\Omega \\ \sqrt{|k|}\sinh\Omega & \cosh\Omega \end{pmatrix}. \end{aligned}$$

The case for which k is negative is similar to the effect of a dipole and thus represents focusing. The other case is, as expected, defocusing. As the sign of k in equations A.13 is opposite for x and y, We see that focusing in one direction automatically implies defocusing in the other direction. The full horizontally focusing quadrupole matrix is thus written as:

$$M_{h-quad} = \begin{pmatrix} \cos\Omega & \frac{1}{\sqrt{|k|}}\sin\Omega & 0 & 0 \\ -\sqrt{|k|}\sin\Omega & \cos\Omega & 0 & 0 \\ 0 & 0 & \cosh\Omega & \frac{1}{\sqrt{|k|}}\sinh\Omega \\ 0 & 0 & \sqrt{|k|}\sinh\Omega & \cosh\Omega \end{pmatrix}.$$

The vertically focusing quadrupole matrix is then obtained by swapping the focusing and the defocusing parts.

To be complete, we should also consider that many dipoles in accelerators like the LHC are not bent according to the radius R, which means that the particle sees the entrance and output of the dipole tilted by some angle Φ with respect to the beam direction.

The main difference between a *sector* dipole and a rectangular one is the path length of the particle in the magnet. If the entrance/exit angle is Φ, the path length difference is $\Delta\Phi = x_0 \tan\Phi$ and the angle given by the bending is diminished by a value $\Delta\alpha = x_0 \tan\Phi/R$. This effects makes the weak focusing weaker. In the matrix formalism, it corresponds to the application of a matrix M_{edge}:

$$M_{edge} = \begin{pmatrix} 1 & 0 \\ \frac{\tan\Phi}{R} & 1 \end{pmatrix}$$

Which should be applied at both sides of the dipole matrix. As we know the bending angle given by the dipole, we will write in all practical applications $\tan\Phi \sim \Phi \sim 2l/R$ as the angles are generally small.

A.1.2 Particle energy loss effect

As can be seen from equation A.13, the path of the particle is momentum-dependent only through the dipolar component of the field at small energy losses. Higher energy losses will obviously affect focusing too and this effect, called *chromaticity*, will be treated later.

If we introduce $\Delta p \neq 0$, we get an inhomogeneous equation of which the homogeneous part has already been solved in the previous section. In order to solve the other part, let us define the dispersion function $D(s)$ as the horizontal trajectory of a particle with $\Delta p = p$. We get:

$$D'' = \frac{D}{R^2} = \frac{1}{R}$$

The constant solution $D(s) = R$ is solution of this inhomogeneous part, and the full solution of the equation becomes:

$$D(l) = D_0 \cos\frac{l}{R} + D'_0 R \sin\frac{l}{R} + R\left(1 - \cos\frac{l}{R}\right) \tag{A.18}$$

For small energy losses, the position of a particle is thus given by:

$$x(l) = x_{no-loss}(l) + D(l)\frac{\Delta p}{p}$$

.

We need to add a degree of freedom corresponding to Δp in the particle vector and an additional line/column appears in the magnets matrices. Computation of a dipole effect then takes the form:

$$\begin{pmatrix} x \\ x' \\ y \\ y' \\ \Delta p \end{pmatrix}(l) = \begin{pmatrix} \cos\frac{l}{R} & R\sin\frac{l}{R} & 0 & 0 & R\left(1-\cos\frac{l}{R}\right) \\ \frac{-1}{R}\sin\frac{l}{R} & \cos\frac{l}{R} & 0 & 0 & \sin lR \\ 0 & 0 & 1 & l & 0 \\ 0 & 0 & 0 & 1 & 0 \\ 0 & 0 & 0 & 0 & 1 \end{pmatrix} \begin{pmatrix} x_0 \\ x'_0 \\ y_0 \\ y'_0 \\ \Delta p \end{pmatrix} \tag{A.19}$$

The additional components stay trivial for all elements with no dipolar field.

An additional effect already quoted is the modification of the focusing effects due to the energy losses. This is directly seen from the definition of k and R as functions of p. We have:

$$k(p) = \frac{p_0}{p}\left(\frac{e}{p_0}\frac{\partial B}{\partial x}\right) = \frac{p_0}{p}k_0$$

This makes all the magnet matrices momentum-dependent. The simulation becomes more complicated as the matrices have to be recomputed for each particle depending on its energy.

A.1.3 Full beam simulation

Once the matrices for all beam elements (magnets or drift sections) have been computed, the simulation of a particle's path is straightforward. We get:

$$\vec{X}(s) = \vec{X}_0 \prod_{s_i<s} M_{s_i} \tag{A.20}$$

Where M_{s_i} is the matrix of the element i at position s_i. The last element should be truncated to get to the required s. This truncation is trivial as it only requires to change the element length l to the desired length. The position $s = 0$ has to be a place where the beam properties are well known in order to fix the vector precisely. In the case of the LHC, the interaction points are used.

The initial vector $\vec{X}_0$ is fixed by two factors: first, the beam has some transverse spatial extension, which corresponds to a smearing of the x and y components of $\vec{X}_0$. The width of this smearing is fixed by design

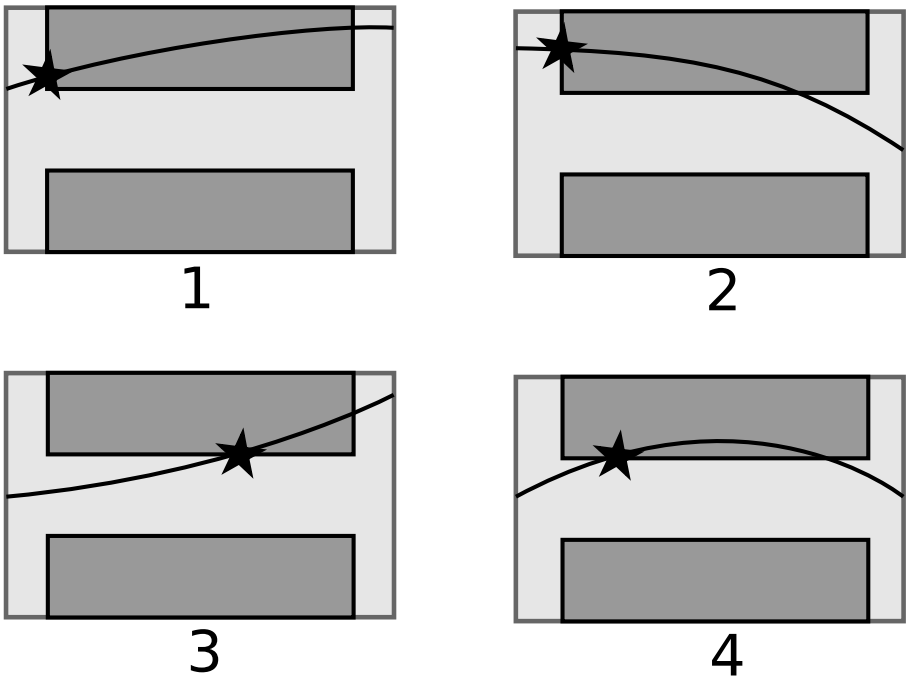

Figure A.1: The four different configurations that can happen when a particle is stopped as it passes through a beam element.

and is considered Gaussian. A similar smearing is applied to the x' and y' components, corresponding to the beam angular spread at the starting position of the simulation. Beside this, the vector is affected by physics. The last component Δp is obviously physics dependent, although the beam energy also suffers some natural spread. The angular components are fixed by the virtuality of the interaction.

A.2 Acceptance computation

Another key point of simulation is the *acceptance*. By acceptance, we design the phase space domain of particles that can reach some point s. For a given element, there are four different possible cases where a particle is stopped while passing through the element, illustrated by Fig. A.1.

The most simple check to perform is to compute the position at the entrance and output of the element and compare it with the aperture of

this element. This solves cases 1 to 3, but does not give any information on the real hit point in case 3, while in cases 1 and 2 the hit point is situated at the entrance of the element.

The case of 4 is slightly harder to solve, as it requires the knowledge of the particle's tridimensionnal path and to compute its intercept with a tridimensionnal shape. This computation would have to be done for every element and would thus increase greatly the computation time. However, this case is unlikely to be an important part of the acceptance limitation at the LHC for the following reasons: this case is most likely to happen in very strong magnets, especially dipoles. The strongest dipoles are the ones aiming at the separation of the beams after the interaction points, which means that the beam basically enters or exits them parallel to the magnet direction. The situation labelled as 4 is thus unlikely to happen in these dipoles. One simple way to cope with this effect would be to check the particle position in the middle of the element, or even at a fixed number of places, but this would directly multiply the computing time and is thus not implemented.

Case 3 is interesting in order to compute secondaries (using a Geant simulation for instance) issued from interactions of particles with the beam element's inner surface. Those secondaries can create hits in very forward detectors which would fake protons coming from the interaction point, and it it thus important to evaluate the rate at which such fake hits will happen. The main difference with case 4 is that only one element has to be checked for each particle, as this test has only to be performed on the first element for which the particle passes the entrance and does not passes the output.

The estimation of the hit point of the particle in the element requires a tridimensionnal representation of the aperture. As the particle path and the aperture shape are in general nontrivial, the usage of algorithms is mandatory. The simplest way is to slice the element into a certain number of sub-elements and to perform checks at the entrance of each of these. the precision obtained with this method is of order l/N where l is the element length and N is the number of computations corresponding to the number of sub-elements.

A more effective way is to use iteration methods based on *dichotomy*. The principle is the following:

1. the bidimensionnal test is performed at the middle of the current element,

2. if the particle passes, the first part of the element is excluded and the current element is set to be the second half of the previous one.

3. if the particle hits, the second part of the element is excluded and the current element is set to the first half.

This principle is illustrated by Fig. A.2. The position precision obtained with this method is of order $l/2^N$. If a realistic precision of 1 mm is required for a typical 1-meter long element, it only requires ten iterations to be reached, which is similar to add ten elements in the beamline in term of computation time. In the case of FP420 detectors at the LHC where computations runs on over 50 elements, this increase is not critical, as it would only represent an increase of the computing time of less than 10% if all particles entered the case 3 category, which is a very pessimistic hypothesis.

A.3 Hector howto

A.3.1 The usual "getting started" chapter

In order to run Hector on your system, first download its sources and compile the *libHector* library[1]:

```
tar jxvf hector_1_2.tgz
cd Hector
```

Hector has been tested with ROOT versions from 4.xx. When launched from Hector's main directory, ROOT will automatically load libHector (see rootlogon.C) and display a welcome prompt. In case you are not using Pythia, one can simply ignore it by commenting `#define _include_pythia_` in ./include/H_Parameters.h[2].

```
~/Hector$ make
~/Hector$ root
```

[1] The Makefile is compatible for a compilation on Linux and Windows/Cygwin systems. For such Windows, just modify the library extension name to LEXT=dll in the Makefile.

[2] If your ROOT version does not contain the PYTHIA libraries, the make command will return an error. In that case, you will have to remove by hand the references to libPythia and libEGPythia in the Makefile, then run "make clean" and "make".

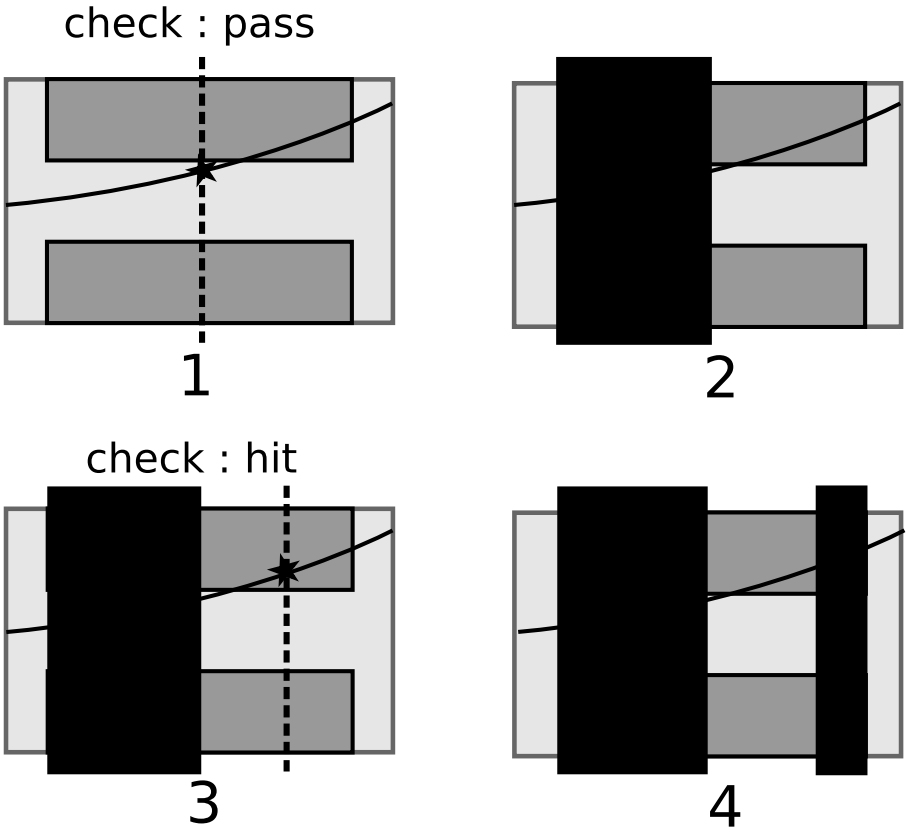

Figure A.2: Iterative algorithm used to compute the hit point of a particle in a magnet.

```
Ready for Hector -- enjoy !
root [0]
```

As a general comment, don't forget that every class you use in your routine should be included in the routine file, for instance:

```
#include "H_BeamLine.h"
#include "H_BeamParticle.h"
```

A.3.2 The everyday life with Hector

In this chapter, we will tell you how to use Hector to perform basics tasks such as using predefined beamlines and designing yours, propagating particles along those, and computing some beam properties. Generally speaking, the detailed constructors and methods arguments for Hector classes will not be detailed here, as it can be easily found in the Internet reference manual[3].

The beamline

The first step to use Hector is to define the list of optical elements that the particles will cross while in the beam pipe. This can be done in two ways:

- Using (existing) magnets tables
- Building the line yourself

Element tables

This way is the simplest. You only need a text file containing columns with the magnet name, position, length, strength. Apertures can also be specified in this file. The order of the columns is meaningless but you should use column headers with the following "codenames":

- NAME: name
- KEYWORD: type
- S: position along the line

[3]This online manual can be found here:

- L: length
- K0L: dipole strength (horizontal)
- K1L: quadrupole strength
- HKICK: horizontal kick angle
- VKICK: vertical kick angle
- APERTYPE: aperture type
- APER_X: aperture size (X runs from 1 to 4)

The "KEYWORD" code defining the element type can take the following values:

- "DRIFT": no-field zone[4]
- "QUADRUPOLE": regular quadrupole
- "RBEND": rectangular dipole
- "SBEND": sector dipole
- "VKICKER": vertical kicker
- "HKICKER": horizontal kicker
- "MARKER": dummy element[5]
- "RCOLLIMATOR": rectangular collimator

The "APERTYPE" can be:

- "NONE": no aperture limitation
- "CIRCLE": circular aperture. the radius is given by APER_1.
- "RECTANGLE": rectangular aperture. The x and y sizes are given by APER_1 and APER_2.

[4]The drift spaces lines in the tables are not read by Hector, because it automatically fills the gaps between other elements with drifts of the right length.

[5]This can be used to tag special places such as Interaction points.

- "ELLIPSE": elliptic aperture. Same size definition as the rectangular aperture.
- "RECTELLIPSE": intersection between a rectangle and an ellipse. The APER_X parameters give the rectangle then the ellipse size.

When your table is properly written, the method to create your beamline is the following[6]:

```
float length = 500;
int direction = 1;
H_BeamLine* mybeamline = new H_BeamLine(direction,length);
mybeamline->fill("table.txt",1,"starting point")
```

The two arguments of the *H_BeamLine* creator are the line length and the direction in which the table will be read (forwards (1) or backwards (-1)). The *fill* Method requires the name of the table file, the propagation direction of the particles from the starting point and the name of the starting point marker.

The meaning of these two direction parameters can seem unclear, so let's suppose you use the following table:

```
NAME              KEYWORD          S   ...

"element1"        "rbend"          0   ...
"element2"        "vquadrupole"   10   ...
"starting point"  "marker"        20   ...
"element3"        "vquadrupole"   30   ...
"element4"        "rbend"         40   ...
```

If the *H_BeamLine* creator argument is 1, we read only the last three elements. Has it been -1, we would have read the first three. The *fill* argument being 1, the particles will go from top to bottom. If it is -1, it goes from bottom to top[7].

Examples of elements tables - taken from the LHC IP5 region - can be found in the "data" directory of Hector as a working example.

[6] As all the methods/functions using a H_BeamLine as argument require it to have the "pointer" type, it is heavily recommended to declare it with that type in all the cases.

[7] It can be useful to notice that the order of the lines does not matter as the ordering is done from the S parameter. However, the elements have to be on their real position (before or after) with respect to the starting point.

Element-by-element beam building

Another way to build the beamline is to add each element separately in the beamline. This is done by this kind of code:

```
float length = 500;
int direction = 1;
H_BeamLine* mybeamline = new H_BeamLine(direction,length);
float position = 10;
float strength = -0.001;
float length = 1;
H_VerticalQuadrupole hvq("myquad",position,strength,length);
mybeamline->add(hvq);
```

This way is not recommended, as the other one is more convenient in most of the cases. But it still can be used to add markers or user-defined elements useful only in specific routines, or to design a new beamline automatically from Monte Carlo techniques.

It is important to note that the *H_Dipole* and *H_Quadrupole* classes are purely abstract and should then never be used directly.

Alignment effects

After building the beamline, one can move elements around their nominal position using the following method:

```
string name = "MCBXA.1R5"
double delta_x = 50;
double delta_y = 30;
mybeamline->alignElement(name,delta_x,delta_y);
```

This will displace the element called $MCBXA.1R5$[8] by the specified amounts in the x and y directions. Corresponding angles can be changed using the similar:

```
mybeamline->tiltElement(name,delta_theta_x,delta_theta_y);
```

[8]Please note that in LHC tables the names include double quotes, meaning that the name should be something like "\"MCBXA.1R5\" ".

The particles

Using the lines:

```
double mass = MP;
double charge = 1;
H_BeamParticle myp(mass, charge);
```

one particle with given mass and charge[9] is created at the "starting point" (IP) with energy defined by the BE (beam energy) given in the *H_Parameters.h* file. The other main variables in this file are:

- SBE: beam energy dispersion
- PX: x position at IP
- PY: y position at IP
- TX: x angle at IP
- TY: y angle at IP
- SX: x dispersion of the beam at IP
- SY: y dispersion of the beam at IP
- STX: x angle dispersion of the beam at IP
- STY: y angle dispersion of the beam at IP

The x and y positions are always given in μm and the corresponding angles are in μrad. The s coordinate is conveniently expressed in meters.

The particle can then be smeared[10] using the SBE, SX, SY, STX, STY parameters by the following methods:

```
myp.smearE();
myp.smearPos();
myp.smearAng();
```

Other useful methods for the particles at the starting point include:

```
H_BeamParticle::emitGamma(float Energy, float virtuality);
```

[9] If not specified, the default particle used is a proton.

[10] These methods use a simple Gaussian smearing.

which allows to simulate the emission of a virtual particle with given properties, causing an energy loss and an angle displacement. Another way to simulate an energy change is to use the

```
H_BeamParticle::setE(float Energy);
```

method which only changes the energy parameter of the particle without any other effects. The effect of the energy loss is obviously simulated by HECTOR[11].

Particle propagation

Once the beamline has been set and the particle has all the desired properties, the latter can be propagated along the former using the following:

```
myp.computePath(mybeamline);
```

This computes the positions and angles of the particle at the entrance of each element and allows to interpolate its position in all the drift spaces. This method is the most time-consuming in HECTOR and thus defines the speed of the program. The typical timescale is less than 4μ s per particle and per element (including drifts)[12].

Apertures check

If one wants to check if the particle has been stopped by any aperture, the following method should be used:

```
bool stopped = myp.stopped(mybeamline);
```

It checks all the element apertures and stores the closest intercepting element from the IP. This element can then be obtained using:

```
const H_OpticalElement* myopticalelement = myp.getStoppingElement();
cout<<myopticalelement->getName()<<endl;
```

for instance to show the element name.

[11] The energies and virtualities are always given in GeV and GeV^2. The virtuality is by definition a negative number.

[12] Tested on a 1.7 GHz Centrino processor running Linux.

Getting the particle information

Once the path has been computed, it is quite legitimate to be be interested by the particle transverse position[13] and angle at some position in s. This is achieved the following methods:

```
float position = 100;
myp.propagate(position);
float x = myp.getX();
float y = myp.getY();
float theta_x = myp.getTX();
float theta_y = myp.getTY();
```

The particle can then be "propagated" to any other other position and the variables obtained at that new positions by the same methods. The complete path can be obtained via the ROOT *TGraph* class using the following:

```
TGraph* ppath_x;
TGraph* ppath_y;
ppath_x = p1.getPath(0,color_x);
ppath_y = p1.getPath(1,color_y);
ppath_x->Draw("AL");
ppath_y->Draw("AL");
```

A convenient way to deal with big numbers of particles is to use the *H_Beam* class. It it build the following way:

```
int number_of_particles = 1000;
H_Beam mybeam;
mybeam.createBeamParticles(number_of_particles);
```

where the *createBeamParticles* method smears all the particle variables using the pre-defined parameters. Most of the single-particle methods can then be applied to the full beam, such as *computePath* and *propagate*. One can access one particle of the beam using the simple

```
int particle_i = 10;
H_BeamParticle* myparticle = mybeam.getBeamParticle(particle_i);
```

[13]The x and y coordinates are respectively the transverse horizontal and vertical displacement of the particle.

for instance to get its properties or to use methods such as *emitGamma* on it. Using a *H_Beam* is especially useful when the user is interested in global properties of the beam, such as its spatial extension, given by the β functions. This is achieved in a straightforward way using the method:

```
float position = 100;
float beta_x_error, beta_y_error;
float beta_x = mybeam.getBetaX(position, beta_x_error);
float beta_y = mybeam.getBetaY(position, beta_y_error);
```

which returns the value of the β function at the given position and the error on this value.

Remarks for the courageous user

In this section we will detail some features of Hector that most people should not use, some problems that will appear to only few of the users, and other exceptionally boring things that could help you in some very seldom cases.

Absolute frame

First of all, Hector is designed to work in "relative frame". This means the normal transverse position for a particle with no angle or displacement at the IP is always 0, and then particles with nominal beam energy will not be deflected by the dipoles.

However, in some case it can be interesting to check the absolute trajectory of the beam. This can be achieved with Hector, if and only if you can consider all your beam elements as parallel. In that case, it suffices to add two lines at the beginning of your routine:

```
extern bool relative_energy;
relative_energy = false;
```

You can also displace all beam elements after a given point laterally using the following:

```
float s_start = 100;
float x_offset = -0.1:
mybeamline->offsetElements(s_start,x_offset);
```

This will displace horizontally all elements from 100m onwards from the IP, by 10 cm in the negative x direction. As this feature is not "natural" in HECTOR, it is not still possible to do the same in the y direction.

Kickers

One exception to the "no-deflection" rule of the previous section is obviously the presence of an initial angle of the beam compared to its natural propagation direction, for instance a crossing angle. This kind of case is usually coped with using "kickers" which deflect the beam by a given angle. These kickers are included in Hector and are the only elements that doesn't respect the "no-deflection" law. If one feels more comfortable to switch this effect off, it is easily done by including:

```
extern int kickers_on;
kickers_on = 0;
```

at the beginning of the routine.

Compiling and running your code

Once you have written a routine and made sure you put it in the right place - for instance the very convenient Hector/routines directory - you only need to compile it. This is most easily done by running root and doing the following[14]:

```
~/Hector$ root -l
Ready for Hector -- enjoy !
root [0] .L routines/myroutine.cpp++
root [1] myprogram()
```

A.3.3 A simple example

As a reward for your patience, here's a little working example of Hector plotting a transverse view of the beam at 220 m from the IP.

```
// C++ #includes
#include <iostream>
```

[14]Here we suppose that Hector is already properly installed on your computer.

```
// ROOT #includes
#include "TH2F.h"

// Hector #includes
#include "H_BeamLine.h"
#include "H_BeamParticle.h"

using namespace std;

void drawProfile() {

  const int NParticle = 1000;
  H_BeamLine* beamline = new H_BeamLine(1,500);
  beamline->fill("data/twiss_ip5_b1_v6.5.txt",1,"IP5");

  TH2F* hp = new TH2F("Pos","",100,-2.5,2.5,100,-2.5,2.5);

  for (unsigned int i=0; i<NParticle ; i++) {
        H_BeamParticle p1;
        p1.smearPos();
        p1.smearAng();
        p1.computePath(beamline);
        p1.propagate(220);
        hp->Fill(p1.getX()/1000.,p1.getY()/1000.);
  }
  hp->Draw();
}
```

Appendix B

Phiti: a simple Υ and J/Ψ photoproduction simulator

Exclusive vector meson production is a very challenging domain when it comes to cross-section predictions. In order to be able to perform studies at the LHC, one needs simulations of such processes. A quick and simple generator was designed in order to estimate the physics potential of vector meson photoproduction studies.

The cross-section for exclusive J/Ψ and Υ production has been measured at Hera as a function of the photon-proton centre of mass energy W up to some hundreds of GeV. We used a fit on this data to determine the *alpha* parameter of the function $\sigma = \alpha W^{1.6}$ [123] in order to extrapolate the cross-section to the LHC region, typically 1.5 TeV if one requires tagging in a detector at 420m from the interaction point.

The differential cross-section for the pp interaction is thus given by:

$$\frac{d\sigma}{dW_{\gamma p}} = \frac{dN}{dx}(x_\gamma)\frac{W}{2E^2}\sigma_{\gamma p}(W), \tag{B.1}$$

Where E is the proton beam energy and $\sigma_{\gamma p \to V}(W)$ is the vector meson production cross-section obtained from HERA data. The resulting differential distribution is shown on Fig. B.1.

The production cross-section is the integral of this distribution over the momentum fractions of both the pomeron and the photon providing some forward detector acceptance. As both protons can be tagged, one should avoid double-counting in the integral. Results compare well with the ones obtained using the StarLight generator as shown on table B.1.

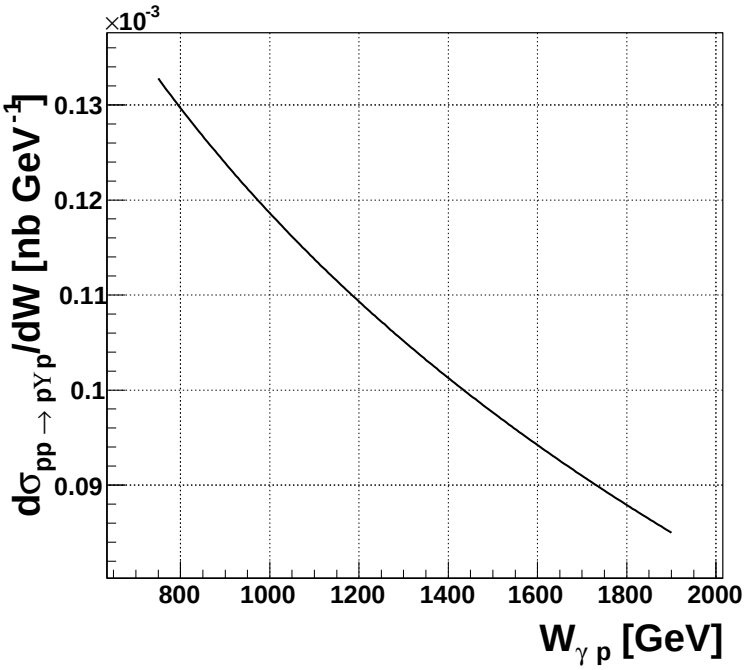

Figure B.1: Differential cross-section for upsilon photoproduction as a function of the γp centre of mass energy W. The photon exchange has been taken as elastic in order to allow a VFD tag.

Process (generator)	cross-section [nb]
$pp \to \Upsilon(1S)$ (Phiti)	1.82
$pp \to \Upsilon(1S)$ (StarLight)	1.57

Table B.1: Exclusive Υ photoproduction cross-section at the LHC computed with StarLight and Phiti. No proton tagging was assumed.

Eventually, the distribution can be used to generate events. First, a photon-proton centre of mass energy is randomly generated according to B.1. The photon energy is then calculated, as well as the longitudinal momentum of the vector meson, neglecting its potential transverse momentum. Pythia 6 is eventually used to decay the vector meson and all particles (initial protons, photon, pomeron, meson and decay products) are then stored in a root file, ready for analysis.

Bibliography

[1] H. Pirmakoff, Phys. Rev. **81** (1951) 899.

[2] R. L. Walker, J. G. Teasdale, V. Z. Peterson and J. I. Vette, Phys. Rev. **99** (1955) 210.

[3] V. E. Balakin, A. D. Bukin, E. V. Pakhtusova, V. A. Sidorov and A. G. Khabakhpashev, Phys. Lett. B **34** (1971) 663.

[4] C. Bacci *et al.*, Lett. Nuovo Cim. **3S2** (1972) 709 [Lett. Nuovo Cim. **3** (1972) 709].

[5] H. J. Besch *et al.*, Phys. Lett. B **81** (1979) 79.

[6] C. Berger *et al.* [PLUTO Collaboration], Phys. Lett. B **107** (1981) 168.

[7] G. Abbiendi *et al.* [OPAL Collaboration], Eur. Phys. J. C **14** (2000) 199 [arXiv:hep-ex/9906039].

[8] M. Acciarri *et al.* [L3 Collaboration], Phys. Lett. B **519** (2001) 33 [arXiv:hep-ex/0102025].

[9] F. Ledroit, Nucl. Phys. B (Proc. Suppl.) **64**, 411 (1998).

[10] R. J. M. Covolan and M. S. Soares, Phys. Rev. D **60**, 054005 (1999);**61**, 019901(E) (2000).

[11] T. Aaltonen *et al.* [CDF Collaboration], arXiv:0902.1271 [hep-ex].

[12] :. T. Aaltonen [CDF Collaboration], arXiv:0902.2816 [hep-ex].

[13] B. Badelek *et al.* [ECFA/DESY Photon Collider Working Group], Int. J. Mod. Phys. A **19** (2004) 5097 [arXiv:hep-ex/0108012].

[14] K. Piotrzkowski, Phys. Rev. D **63**, 071502 (2001)

[15] J. Freidman *et al.*, Phys. Rev. D **5**, 528 (1972)

[16] M. Klein and R. Yoshida, arXiv:0805.3334 [hep-ex].

[17] M. Derrick *et al.* [ZEUS Collaboration], Phys. Lett. B **346**, 399 (1995)

[18] T. Ahmed *et al.* [H1 Collaboration], Phys. Lett. B **348**, 681 (1995)

[19] N. Cartiglia [H1 Collaboration and ZEUS Collaboration], arXiv:hep-ph/9703245.

[20] C. Diaconu [H1 Collaboration and ZEUS Collaboration], arXiv:hep-ex/0610041.

[21] M. Turcato [H1 Collaboration and ZEUS Collaboration], arXiv:0810.0501 [hep-ex].

[22] S. Chekanov *et al.* [ZEUS Collaboration], Eur. Phys. J. C **38** (2004) 43 [arXiv:hep-ex/0408009].

[23] J. Lukasik, *Prepared for 15th International Workshop on Deep-Inelastic Scattering and Related Subjects (DIS2007), Munich, Germany, 16-20 Apr 2007*

[24] C. Adloff *et al.* [H1 Collaboration], Nucl. Phys. B **619** (2001) 3 [arXiv:hep-ex/0106070].

[25] I. Wilson, W. Schnell and H. Henke, *In the Proceedings of IEEE Particle Accelerator Conference, Chicago, Illinois, 20-23 Mar 1989, pp 103.*

[26] C. F. von Weizsacker, Z. Phys. **88**, 612 (1934).

[27] E. J. Williams, Phys. Rev. **45**, 729 (1934).

[28] V.M. Budnev, I.F. Ginzburg, G.V. Meledin and V.G. Serbo, Phys. Rept. **15**, 181 (1974).

[29] C. Pisano, Eur. Phys. J. C **38**, 79 (2004) [arXiv:hep-ph/0408101].

[30] B. A. Kniehl, Phys. Lett. B **254**, 267 (1991).

[31] M. Spira, arXiv:hep-ph/9905469.

[32] R. Nisius, D. Haas and C. Grupen, arXiv:hep-ex/0006032.

[33] M. Derrick *et al.* [ZEUS Collaboration], Phys. Lett. B **297** (1992) 404.

[34] T. Ahmed *et al.* [H1 Collaboration], Phys. Lett. B **297** (1992) 205.

[35] H. Abramowicz, E. M. Levin, A. Levy and U. Maor, Phys. Lett. B **269** (1991) 465.

[36] H. Abramowicz and A. Levy, arXiv:hep-ph/9712415.

[37] T. Aaltonen *et al.* [CDF Collaboration], Phys. Rev. D **76** (2007) 111103 [arXiv:0705.2247 [hep-ex]].

[38] J. Abdallah *et al.* [DELPHI Collaboration], Eur. Phys. J. C **54** (2008) 345 [arXiv:0801.1235 [hep-ex]].

[39] S. Schael *et al.* [ALEPH Collaboration], Phys. Lett. B **614** (2005) 7.

[40] P. Achard *et al.* [L3 Collaboration], Phys. Lett. B **597** (2004) 119 [arXiv:hep-ex/0407012].

[41] E. Accomando and A. Kaiser, Phys. Rev. D **73** (2006) 093006 [arXiv:hep-ph/0511088].

[42] T. Pierzchala and K. Piotrzkowski, arXiv:0807.1121 [hep-ph].

[43] S. L. Glashow, J. Iliopoulos and L. Maiani, Phys. Rev. D **2** (1970) 1285.

[44] J. M. Yang, B. L. Young and X. Zhang, Phys. Rev. **D 58** 055001 (1998)

[45] F. del Aguila, J. A. Aguilar-Saavedra and R. Miquel, Phys. Rev. Lett. **82** (1999) 1628 [arXiv:hep-ph/9808400].

[46] G. Liu and H. j. Zhang, arXiv:0708.1553 [hep-ph].

[47] R. Ammar *et al.* [CLEO Collaboration], Phys. Rev. Lett. **71** (1993) 674.

[48] S. Anderson *et al.* [CLEO Collaboration], Phys. Rev. Lett. **87** (2001) 181803 [arXiv:hep-ex/0106060].

[49] B. Aubert *et al.* [BABAR Collaboration], Phys. Rev. Lett. **93** (2004) 191801 [arXiv:hep-ex/0408023].

[50] V.V. Animovsky*et al.*, Phys. Rev. Lett. **93** (2004) 031801.

[51] T. Han and J. L. Hewett, Phys. Rev. D **60** (1999) 074015

[52] J. Abdallah *et al.* [DELPHI Collaboration], Phys. Lett. B **590** (2004) 21 [arXiv:hep-ex/0404014].

[53] P. Achard *et al.* [L3 Collaboration], Phys. Lett. B **549** (2002) 290 [arXiv:hep-ex/0210041].

[54] A. Heister *et al.* [ALEPH Collaboration], Phys. Lett. B **543** (2002) 173 [arXiv:hep-ex/0206070].

[55] G. Abbiendi *et al.* [OPAL Collaboration], Phys. Lett. B **521** (2001) 181 [arXiv:hep-ex/0110009].

[56] S. Xella, PoS **TOP2006** (2006) 030.

[57] F. Abe *et al.* [CDF Collaboration], Phys. Rev. Lett. **80** (1998) 2525.

[58] M. Antonelli, *Prepared for 31st International Conference on High Energy Physics (ICHEP 2002), Amsterdam, The Netherlands, 24-31 Jul 2002*

[59] C. Adlo *et al.*, Eur. Phys. J. C **5**, 575 (1998).

[60] V. Andreev *et al.*, Phys. Lett. B **561**, 241 (2003).

[61] A. Aktas *et al.*, Eur. Phys. J. C 4**8**, 699 (2006).

[62] D. M. South [H1 and ZEUS Collaboration], J. Phys. Conf. Ser. **110** (2008) 072041 [arXiv:0709.4433 [hep-ex]].

[63] M. Derrick *et al.* [ZEUS collaboration], Phys. Lett. B **293** (1992) 465.

[64] ZEUS Collaboration, Status Report 1993, DESY(1993).

[65] V. Chiochia [ZEUS MVD Group], Nucl. Instrum. Meth. A **501** (2003) 60

[66] B. Foster *et al.* [ZEUS Collaboration], Nucl. Instrum. Meth. A **338** (1994) 254.

[67] M. Derrick *et al.*, Nucl. Instrum. Meth. A **309** (1991) 77.

[68] U. Baur, J. A. M. Vermaseren and D. Zeppenfeld, Nucl. Phys. B **375** (1992) 3.

[69] K. Charchula, G.A. Schuler and H. Spiesberger, Comp. Phys. Comm. **81**, 381 (1994).

[70] R. Brun, R. Hagelberg, M. Hansroul and J. C. Lassalle, "Geant: Simulation Program For Particle Physics Experiments. User Guide And Reference Manual"

[71] H. Abramowicz, A. Caldwell and R. Sinkus, Nucl. Instrum. Meth. A **365** (1995) 508 [arXiv:hep-ex/9505004].

[72] A. Kwiatkowski, H. Spiesberger and H.-J. Mhring, Comp. Phys. Comm. **69**, 155 (1992).

[73] G. Ingelman, A. Edin and J. Rathsman, Comp. Phys. Comm. **101**, 108 (1997).

[74] L. Lönnblad, Comp. Phys. Comm. **71**, 15 (1992).

[75] T. Sjöstrand, Comp. Phys. Comm. **39**, 347 (1986).

[76] J. Ferrando, Mod. Phys. Lett. A **21** (2006) 1901.

[77] E. Rizvi, Talk presented at DIS2008.

[78] A. A. Affolder *et al.* [CDF Collaboration], Phys. Rev. Lett. **84** (2000) 5043.

[79] J. D. Bjorken, Phys. Rev. D **47** (1993) 101.

[80] V. A. Khoze, A. D. Martin and M. G. Ryskin, Phys. Lett. B **650** (2007) 41 [arXiv:hep-ph/0702213].

[81] V. A. Khoze, A. D. Martin and M. G. Ryskin, Eur. Phys. J. C **23** (2002) 311

[82] V.A. Khoze, A.D. Martin and M.G. Ryskin, Eur. Phys. J. C**23**, (2002) 311.

[83] T. Regge, Nuovo Cim. **14** (1959) 951.

[84] S. Chekanov *et al.* [ZEUS collaboration], Eur. Phys. J. C **38**, 43 (2004).

[85] A. Atkas *et al.*, Eur. Phys. J. C **48**, 715 (2006).

[86] J. C. Collins, J. Phys. G **28** (2002) 1069 [arXiv:hep-ph/0107252].

[87] ATLAS Collaboration [CERN/LHCC 2007-001]

[88] ATLAS Collaboration [CERN/LHCC 2008-004]

[89] K. Osterberg, J. Phys. Conf. Ser. **110** (2008) 022037.

[90] A. L. S. Angelis *et al.*, arXiv:hep-ex/9901038.

[91] B. E. Cox, AIP Conf. Proc. **792** (2005) 540.

[92] F. Maltoni and T. Stelzer, JHEP **0302** (2003) 027 [arXiv:hep-ph/0208156].

[93] H. U. Bengtsson and T. Sjostrand, Comput. Phys. Commun. **46** (1987) 43.

[94] O. Bruning, P. Collier, P. Lebrun, S. Myers, R. Ostojic, J. Poole and P. Proudlock, [CERN/LHCC 2004-003]

[95] J. de Favereau, X. Rouby and K. Piotrzkowski, JINST **2**, P09005 (2007) [arXiv:0707.1198 [physics.acc-ph]].

[96] R. Appleby *et al.*, *In the Proceedings of 11th European Particle Accelerator Conference (EPAC 08), Magazzini del Cotone, Genoa, Italy, 23-27 Jun 2008, pp MOPP006.*

[97] J. de Favereau *et al.*, CP3-08-04, June 2008.

[98] The CMS Collaboration, CMS PAS FWD-08-003

[99] J. de Favereau de Jeneret and S. Ovyn, Nucl. Phys. Proc. Suppl. **179-180** (2008) 277 [arXiv:0806.4886 [hep-ph]].

[100] N. Schul and K. Piotrzkowski, Nucl. Phys. Proc. Suppl. **179-180** (2008) 289 [arXiv:0806.1097 [hep-ph]].

[101] M. Maniatis, A. v. Manteuffel, O. Nachtmann, Nucl. Phys. Proc. Suppl. **179-180** (2008) 104

[102] J. Alwall *et al.*, Eur. Phys. J. C **49**, 791 (2007) [arXiv:hep-ph/0607115].

[103] A. Giammanco [CMS and ATLAS Collaborations], PoS **TOP2006**, 025 (2006).

[104] M. Tytgat, Eur. Phys. J. A **31** (2007) 451.

[105] D. Szuba [ZEUS Collaboration], PoS D **IFF2006** (2006) 012.

[106] The CMS Collaboration, CMS PAS DIF-07-001

[107] S. R. Klein and J. Nystrand, Phys. Rev. Lett. **92** (2004) 142003 [arXiv:hep-ph/0311164].

[108] A. Pukhov, arXiv:hep-ph/0412191.

[109] B. E. Cox and J. R. Forshaw, Comput. Phys. Commun. **144** (2002) 104 [arXiv:hep-ph/0010303].

[110] V. A. Khoze, A. D. Martin and M. G. Ryskin, Phys. Lett. B **643** (2006) 93 [arXiv:hep-ph/0609312].

[111] CMS Collaboration [CERN/LHCC 2006-001]

[112] P. Azzurri [On behalf of the CMS Collaboration], arXiv:0812.5036 [physics.ins-det].

[113] The CMS Collaboration, CMS PAS HIG-08-006

[114] CMS Collaboration [CMS AN 2007/001]

[115] CMS Collaboration [CERN/LHCC 2006-021]

[116] A. G. Holzner, arXiv:hep-ex/0408030.

[117] L. Benucci and A. Kyriakis, Nucl. Phys. Proc. Suppl. **177-178** (2008) 258.

[118] J. Carvalho, N. Castro1, L. Chikovani, T. Djobava, J. Dodd, S. McGrath, A. Onofre, J. Parsons, F. Veloso [arXiv:hep-ex/0712.1127v1]

[119] J. A. Aguilar-Saavedra, Acta Phys. Polon. B **35** (2004) 2695 [arXiv:hep-ph/0409342].

[120] CMS Collaboration [CERN/LHCC 2000-038]

[121] K. L. Brown, F. Rothacker, D. C. Carey and F. C. Iselin,

[122] R. Brun and F. Rademakers, Nucl. Instrum. Meth. A **389** (1997) 81.

[123] M. F. McDermott, Nucl. Phys. Proc. Suppl. **79** (1999) 355 [arXiv:hep-ph/9905288].

List of Figures

1.1 The HERA collider complex with its injection system. . . 6
1.2 Integrated luminosity provided by the HERA collider as a function of the number of days of running. 8
1.3 $x - Q^2$ range of various experiments for the measurement of structure functions. Fixed-target experiments fill the lower right part of the graph, corresponding to low Q^2 and high x, while HERA extended the range to higher virtualities and lower x. The LHC expected range is also plotted. 9
1.4 Number of observerd events as a function of the pseudo-rapidity η_{max} of the most forward calorimeter cluster in the ZEUS detector, compared with the Monte Carlo DIS expectation. One clearly sees the excess of events with an important rapidity gap between the outgoing proton direction and any activity in the detector [17]. 10
1.5 Typical deep inelastic scattering event at HERA (up) and event with a rapidity gap (down) [19]. In the latter, no activity is observed in the detector in the region between the proton outgoing direction (left) and the jet, leading to a rapidity gap with $\eta_{max} \sim 0$. 11
1.6 Satellite view of the LHC (top) and schematic view of the accelerator and its injection complex (bottom). 15
1.7 Feynman diagrams for Deep Inelastic Scattering (left) and the corresponding photoabsorbtion process (right). 17
1.8 Reference diagram for the definition of variables used in the text. 18

1.9 Kinematically allowed line for (P_T, M_X) for x = 0.001 (left) and 0.05 (right) for a photon virtuality of 0.1 GeV^2 (plain) and 10 GeV^2 (dashed). 19
1.10 Lepton pair production via photon-photon interaction . . 21
1.11 Comparison of exact computation of the process $ep \to \nu WX$ with the result obtained through EPA. The EPA elastic component is indistinguishable from the exact calculation 22
1.12 Behaviour of the form factors H_1 (plain) and H_2 (dashed) as a function of the photon virtuality. 24
1.13 Value of the structure function F_2 as a function of the virtuality of the exchanged boson ($M_X^{max} = 20$ GeV). . . 26
1.14 Photon energy spectrum for inelastic photon exchange as a function of the photon energy fraction x. The mass M_X has been required to be lower than 20 GeV. 27
1.15 Relative luminosity $\mathcal{N}(W)$ for elastic photon-photon interactions at the LHC. 29
1.16 Relative luminosity $\mathcal{N}(W)$ for photon-gluon (plain) and photon-quark interactions at the LHC. Here only the up (dashed) and down (dotted) quark contents were considered. 30
1.17 Typical t-channel process via photon-proton interaction. . 31
1.18 Illustration of the singularity extraction for the W + quark photoproduction. 32
1.19 One-loop diagrams for FCNC in the SM 34
1.20 One-loop diagrams for FCNC in Multi-Higgs Models . . . 35
1.21 Single top production at LEP through flavour changing neutral currents. 37
1.22 Single top production at HERA through flavour changing neutral currents. 37
1.23 FCNC decay of a top quark 38
1.24 Current limits on the anomalous couplings $k_{tu\gamma}$ and v_{tuZ} . 38

2.1 Diagrams for W boson production in the Standard Model with the subsequent decay to fermions. The process $ep \to \nu_e WX$ is not depicted. Diagram (c) is sensitive to possible anomalous triple gauge couplings. Diagrams (d) and (e) are included to preserve gauge invariance. The present analysis only focuses on final states including an electron and a neutrino. 42

2.2 Side (top) and front (bottom) cuts of the ZEUS detector . 45
2.3 Deeply inelastic neutral current (left) and charged current (right) interactions at HERA. 46
2.4 Two-photon production of a lepton pair at HERA (with elastic photon emission by the proton). 47
2.5 Number of good tracks versus the total number of tracks for beam-gas events. The line represents the condition described by equation 2.1. One clearly sees the separation between beam-gas induced events (lower right) and physical events. 51
2.6 Distributions of the isolated electron events compared with the SM expectation for the data taking period 1999-2000 which represents the most important statistics in the present analysis. The error bars on the data points correspond to $\sqrt{N_i}$ where N_i is the number of events in bin i of the histogram. 53
2.7 Acoplanarity distribution of the isolated electron events compared with the SM expectation for the data taking period 1999-2000 55
2.8 Reconstructed Q^2 distribution of the isolated electron events compared with the SM expectation for the data taking period 1999-2000 55
2.9 Selected event from the 96-97 data taking period. The electron candidate is clearly visible in the lower part of the detector. 56

3.1 Diffractive (left) and two-photon (right) production of a Higgs boson at the LHC 64
3.2 Photon energy spectrum as a function of the virtuality of the emitted photon in the case of inelastic photon emission. 65
3.3 Longitudinal impact parameter resolution for single tracks in the CMS detector [111]. 66
3.4 Layout of the LHC beam line around IP1 and IP5. See text for a complete description. 73
3.5 The *roman pot* design of TOTEM very forward detectors 75
3.6 Position s reached by a particle with given energy loss E_{loss}. The particle is supposed to be at the centre of the beam with no angle at the interaction point. Forward detectors were considered at 420 m from IP only. 77

3.7 Acceptance of very forward detectors at 220 m (top) and 420 m (bottom) from the IP for beam 1. The plain lines represent 100 % acceptance, while dashed lines give the 75 %, 50 % and 25 % limits. The detectors at 220 m and 420 m have been assumed to approach the beam at 2 mm and 4 mm respectively. 78

3.8 Acceptance of very forward detectors at 220 m (top) and 420 m (bottom) from the IP for beam 2. The plain lines represent 100 % acceptance, while dashed lines give the 75 %, 50 % and 25 % limits. The detectors at 220 m and 420 m have been assumed to approach the beam at 2 mm and 4 mm respectively. 79

3.9 Effective luminosity of photon-photon interactions with the requirement of one (up) or two (down) tagged protons using detectors at 220 m (dashed), 420 m (dotted) or both stations (dash-dotted). One should note that in the case of single tag, luminosities have to be multiplied by two in order to take into account the symmetry between the two beams. The solid line shows the untagged luminosity. . . . 81

3.10 Effective luminosity of photon-proton interactions in gamma-quark (up) and gamma-gluon (down) channels using detectors at 220 m (dashed), 420 m (dotted). On the gamma-quark luminosity plot, the luminosity including one tag at 220 is indistinguishable from the untagged lumi after 1500 GeV while the luminosity for a 420 m tag dies around 2 TeV of centre of mass energy. Only the interactions with the up quark were considered for illustration. The solid line shows the untagged luminosity. 82

3.11 Effect of momentum transfer of 10 GeV^2 on the beam profile (left). As the position is measured only using one detector plane, this affects strongly the reconstructed energy resolution (right). 84

3.12 Chromaticity grids for detectors at 220 m from CMS interaction point. Lines represent protons with same energy loss (plain) and angle (dashed). The lower plot was built without taking into account the second-order effect of the energy loss, while the top plot includes it. 86

3.13 Resolution of the reconstructed energy loss of protons as a function of the energy loss (left) and the transverses momentum (right), for stations at 420 m (up) and 220 m (down). The detector resolution was supposed to be perfect (no smearing, circles), 5 μm (squares) and 30 μm (triangles). 89
3.14 Resolution of the reconstructed transverse momentum of protons as a function of the energy loss (left) and the transverses momentum (right), for stations at 220 m (up) and 420 m (down). The detector resolution was supposed perfect (no smearing, circles), 5 μm (squares) and 30 μm (triangles). 90
3.15 Effect on the reconstructed (using detectors at 420 m) proton energy loss of a 0.5 mm transverse displacement of the quadrupole placed at s. 91
3.16 Effect on the reconstructed (using detectors at 420 m) proton energy loss of a 0.5 mm transverse displacement of the quadrupole placed at s, while considering the beam position at the VFD to be known perfectly. 92
3.17 Reconstruction of a centrally produced higgs boson via photon-photon interaction using the missing mass method. The empty histogram shows the effect of the misalignment of a quadrupole close to the IP. The shaded histogram is obtained using perfect beam position knowledge. The filled histogram represents the effect of a calibration based on $\sim$ 100 dimuon events. 94
3.18 Illustration of accidental coincidences between a soft diffractive event (grey) including a surviving proton which can be detected by VFDs and a hard event mimicking the signal (black). 95
3.19 Effect of the requirement to have exactly one proton hit in the forward detectors on the signal over background ratio. A value of one means that this requirement does not affect the ratio. Values below one represent a degradation of the ratio. 98
3.20 Expected reduction factor as a function of the luminosity for two bunch crossing rate scenarios (10 MHz and 40 MHz), for a scenario including detectors at 220 m and 420 m. 99

3.21 Integrated number of protons potentially hitting very forward detectors at 420 m as a function of the distance from the beam centre. The beam halo coming from the effect of collimators (Mom. Cleaning) dominates at distances lower than 5 mm but dies quickly afterwards, while the halo from distant beam gas interactions is smaller close to the beam but falls slower at larger distances. 101

4.1 Cross-sections for various photon-photon processes as a function of the invariant mass threshold W_0. Acceptance cuts have been applied on lepton pairs [97]. 104
4.2 Cross-sections for various photoproduction processes as a function of the γp centre of mass energy [97]. 106
4.3 Vector mesons production cross-section as a function of the photon-proton centre of mass energy as measured at HERA by the HERMES, H1 and ZEUS collaborations. . . 108
4.4 Single top production at the LHC through flavour changing neutral currents. 108
4.5 Number of events per bunch-crossing for three different running scenarii 109
4.6 Top SM decay into a jet, a charged lepton and a neutrino 110
4.7 Diagram for diffractive W production at the LHC. 112
4.8 Non-b jet mistagging efficiency versus b-jet tagging efficiency for jets from charm quarks (triangles), light quarks (circles) and gluons (stars) with the CMS detector [111]. . 114
4.9 Selection efficiency as a function of the maximum allowed energy in the quietest forward calorimeter E_{min}^{FCAL} for the signal (plain), hard diffractive W production (dotted) and partonic backgrounds (dashed). 115
4.10 Illustration of the rapidity gap and exclusivity conditions used to reject partonic backgrounds. The forward calorimeters cover the region depicted in grey. Once the quietest side is determined and if its energy passes the cut, it is called the *gap side* and the exclusivity condition is applied on the shaded region. 116
4.11 Transverse momentum cumulative distribution of the reconstructed jet, after acceptance cuts on the jet and the lepton, rapidity gap and exclusivity conditions and b-tagging. Events for which $40 < P_T < 80$GeV are selected. 117

4.12 Transverse momentum cumulative distribution of the reconstructed lepton, after acceptance cuts on the jet and the lepton, rapidity gap and exclusivity conditions and b-tagging applied on the jet. Events for which $15 < P_T <$ 80GeV are selected. 118
4.13 Missing transverse energy cumulative distribution after acceptance cuts on the jet and the lepton, rapidity gap and exclusivity conditions and b-tagging applied on the jet. Events with a missing transverse momentum above 15 GeV were selected 119
4.14 Reconstructed top mass cumulative distribution, after acceptance cuts on the jet and the lepton, rapidity gap and exclusivity condition and b-tagging applied on the jet (up) and after full selection (down). Events with a reconstructed top mass between 130 and 200 GeV are selected. 121
4.15 Distribution of the acoplanarity $\Delta\phi$ for signal and background events after acceptance cuts. Events with $\Delta\phi >$ 0.1 are selected. The bold plain line represents the signal distribution while dashed, dotted and dash-dotted lines represent distributions for partonic, photoproduction and diffractive events respectively. 122
4.16 Exclusion region for the anomalous couplings after 1 fb^{-1}. The effect of a positive or negative variation of the expected number of events according to the systematic uncertainties is shown by the dashed lines. 128
4.17 Total longitudinal momentum of the central event versus photon energy for the signal (top) and the partonic backgrounds (bottom). One clearly sees the lack of correlation between the central event and the photon in partonic backgrounds. 130
4.18 Cumulative distribution of the ΔP_Z variable after acceptance cuts on the lepton and the jet, application of the exclusivity condition and proton tagging 131
4.19 Distribution of the b-jet energy the centre of mass frame of the top quark, reconstructed using the photon energy information from very forward detectors. Basic acceptance cuts, exclusivity condition, b-tagging and proton tag were required 133

4.20 Distribution of the lepton energy the centre of mass frame of the W boson, reconstructed using the photon energy information from very forward detectors and the b-jet direction from the central detector. Basic acceptance cuts, exclusivity condition, b-tagging and proton tag were required 134

4.21 Selection efficiency as a function of η_{max} for the signal (plain), hard diffractive W production (dotted) and partonic backgrounds (dashed). 135

4.22 Two-dimensional limits on the anomalous couplings $k_{tu\gamma}$ and $k_{tc\gamma}$ (solid) for the intermediate scenario of an instantaneous luminosity of $2 \times 10^{33}\text{cm}^{-2}\text{s}^{-1}$ and 30 fb^{-1} of integrated luminosity using VFDs for tagging and reconstruction. The other lines correspond to a positive or negative variation of the observed number according to the systematic uncertainty. 139

4.23 Distribution of the jet transverse momentum P_T (top) and effect of a cut on this variable on the selected sample for W photoproduction (bottom). Dashed and dotted lines correspond to anomalous couplings. The numbers shown on both plots are obtained after requiring a single hit in the VFDs, exclusivity on the photon side and an isolated lepton with $P_T > 15$ GeV. The bottom plot shows the number of observed events after 30 fb^{-1}. The two plain lines on this plot represent one sigma deviations from the SM scenario. 142

4.24 Illustration of the effect of the combination of the present analysis with results from top FCNC decay, assuming the latter show an excess corresponding to $k_{tq\gamma} = 0.05$. The dashed line corresponds to the allowed values for both couplings according to an analysis based on top decay, while the plain line is based on the top photoproduction analysis of the present work (with arbitrary results for the purpose of illustration). The black dot at the intersection gives the most probable value for the couplings. Contours can be obtained by combining the results using a likelihood approach. 145

A.1 The four different configurations that can happen when a particle is stopped as it passes through a beam element. . 158
A.2 Iterative algorithm used to compute the hit point of a particle in a magnet. 161

B.1 Differential cross-section for upsilon photoproduction as a function of the γp centre of mass energy W. The photon exchange has been taken as elastic in order to allow a VFD tag. 174

List of Tables

1.1 Parameters of the HERA collider during the HERA-I (HERA-II) phase. 7
1.2 Parameters of the LHC in injection and collision mode. . 16
1.3 H_1 and H_2 functions for different beam particles. G_E, G_M and F_π are form factors of the proton and pion. F_2 is the usual proton structure function. 21
1.4 Maximum FCNC decay branching ratio and couplings of the top quark in some models. 36

2.1 Signal subsamples simulated with EPVEC. 48
2.2 List of the simulated background samples along with their associated cross-section and sample size. 49
2.3 Remaining data events and SM expectation after selection for the four periods of data taking. The SM backgrounds are the ones listed in table 2.2. 57
2.4 Expected MC and observed events for three regions in P_T^X. 58

3.1 single diffractive tagging efficiency for different detector scenarios.The detector at 220 m(420 m) is placed at 2 mm(4 mm) from the beam position. Beam 1 and beam 2 values have been averaged. 96
3.2 Average single diffractive pileup λ for different luminosity scenarios. 99
3.3 Expected reduction factor. Although the numbers are given for illustration, forward detectors at 420 m are not expected to be present for early LHC runs at 10^{32} cm^{-2} s^{-1}. 99

4.1 Background processes used for the analysis of the anomalous top photoproduction. Cross-sections include generation cuts of $P_T > 10$ GeV for leptons and $P_T > 20$ GeV for jets. The symbol 'j' stands for jets coming from light quarks (u, d, s) and gluons. 111

4.2 Branching ratio of the top quark to b quark and W boson as a function of the anomalous couplings for couplings lower than the exclusion limit. 112

4.3 List of all applied cuts and their effect on the visible cross-section of different samples. 123

4.4 Systematic errors on signal and backgrounds 125

4.5 Selection efficiency for signal, photoproduction, single soft diffractive (for the computation of accidental coincidences) and hard diffractive background events when requiring at least one proton tag at 220 m, 420 m or using both stations. 129

4.6 List of all applied cuts and their effect on the number of selected events of different samples after 30 fb^{-1} for an instantaneous luminosity of 2×10^{33} cm^{-2} s^{-1} Using very forward detectors at 220m and 420m for tagging and reconstruction. The cuts on the center of mass kinematics using the recontructed photon energy are $\Delta E_b < 15$GeV and $\Delta E_l < 5$GeV 137

4.7 List of all applied cuts and their effect on the number of selected events of different samples after 30 fb^{-1} for an instantaneous luminosity of 2×10^{33} cm^{-2} s^{-1} using no forward detectors. 138

4.8 Expected number of events and limits on the anomalous couplings for three different LHC running scenarii, namely $10^{33}, 2 \times 10^{33}$ or 10^{34} cm^{-2} s^{-1}. The limits do not include systematic uncertainties. 140

4.9 Effect of an additional 1 mm distance between VFD stations and the beam on the selection efficiency obtained using both stations. 141

4.10 Effect of the anomalous couplings on the visible cross-section after the full analysis described in this chapter ("Normal") and using the high P_T jet selection described in this section. Diffractive and partonic backgrounds are included in the computation of the effect. A luminosity of 2×10^{33} cm^{-2} s^{-1} was assumed for the computation of accidental coincidences of the "low lumi" scenario. 143

B.1 Exclusive Υ photoproduction cross-section at the LHC computed with StarLight and Phiti. No proton tagging was assumed. 174